Hydrogen Plasma Defined Graphene Edges

Inauguraldissertation

zur

Erlangung der Würde eines Doktors der Philosophie

vorgelegt der

Philosophisch-Naturwissenschaftlichen Fakultät

der Universität Basel

von

Mirko K. Rehmann

aus Kaisten AG, Schweiz

Basel, 2019

Genehmigt von der Philosophisch-Naturwissenschaftlichen Fakultät auf Antrag von

Prof. Dr. Dominik M. Zumbühl

Prof. Dr. Andras Kis

Basel, den 11. Dezember 2018

Prof. Dr. Martin Spiess

(Dekan)

Abstract

In this thesis, anisotropic etching of graphite and graphene in a hydrogen (H) plasma is investigated. The exposure of graphite flakes at different plasma pressures and sample-plasma distances reveals the existence of two different plasma regimes: the *direct* and the *remote* regime. In the direct regime, high energetic H-ions continuously induce new defects into the graphite surface during the etching process, thus leading to a perforated surface. In the remote plasma regime, on the other hand, well-defined hexagonal etch pits evolve, which grow in size, while their number remains constant. This indicates anisotropic etching, which takes place only at pre-existing defects and edges and leaves the graphite basal plane pristine.

In a second step of the experiment, the substrate dependence of single layer graphene etching in the remote plasma regime is investigated. Interestingly, the etching is only anisotropic for hexagonal boron nitride substrates but isotropic if graphene is placed on Si/SiO_2. It was previously found that the edges of H plasma defined hexagons on graphite run along the zigzag (ZZ) direction of the crystal lattice. Hence, by inducing artificial defects into a graphene flake, one can tailor diverse graphene nano-structures with presumably well-defined ZZ edges, such as e.g. graphene nano ribbons.

However, it is not exactly known how good the quality of as-fabricated graphene edges really is. This open question is addressed in the second work, where the quality of H plasma defined graphene edges is investigated by means of atomic resolution atomic force microscopy (AFM), Raman spectroscopy and low-temperature electronic transport experiments. AFM measurements on hexagons created on graphite surfaces reveal that the edges are aligned to the ZZ direction and the absence of the Raman D-peak suggests that these edges are high quality ZZ edges. In contrast, hexagons created in single layer graphene on hexagonal boron nitride exhibit a relatively large D-peak, pointing towards the presence of edge disorder or armchair segments. Polarization-dependent Raman experiments indicate that the edges consist of a mixture of armchair and ZZ

segments. Furthermore, electronic transport measurements, combined with quantum transport simulations, support the findings from the Raman experiments. Hence, H plasma defined edges still suffer from edge disorder and the etching process needs to be further optimized in order to get high quality crystallographic graphene edges.

In addition to the graphene experiments, investigations on Ge/Si core/shell nano wires are conducted. In particular, single, double, and triple quantum dots (QDs) of various sizes and with low occupation numbers are formed. In the single QD regime, indications for the last hole state are found. Moreover, Pauli spin blockade is observed in the double QD regime. These results open the door for exploring Ge/Si core/shell nano wires as a potential platform for hole spin-qubit experiments.

Contents

1 Introduction

The invention of the computer in the early 1940s has since had a major influence on many different aspects of our lives and is omnipresent in the modern world. With the increase in computational power, new fields of application became accessible. Today, computers are essential elements in many areas of our daily lives, mostly in custom-tailored form and adapted to specific purposes. Examples are embedded systems for control of everyday devices such as, e.g. washing machines, TVs and cars. Personal computers are used in smart phones and laptops and have their application area, among other things, in data processing in economy and industry. Super-computers with large computational power are used to simulate complex processes such as, e.g. climate developments or medical procedures.

Although there was a continuous development and increase of computational power in the past 70 years, fundamental limits are anticipated, which slow down and eventually stop a further rise in computational capacity. Increasing the computational capacity is connected to miniaturization of transistors, the basic building blocks of computers. However, there are physical limits in miniaturization, and already in current devices, quantum mechanical effects become perceptible and can interfere with device functionality. Interestingly, it is these quantum mechanical effects which seem to provide a solution for further development and increase in computational power. In particular, a quantum computer was proposed by Feynman in the 1980s [1, 2] and triggered a whole new field of research, which focuses on its realization and development.

In a quantum computer, the fundamental building block is a two-level system, which in analogy to the *classical bit*, is called a *quantum bit* (qubit). In contrast to a classical bit, which encodes only two states (i.e. "1" and "0"), a qubit can, in addition to the two eigenstates of the system, be in any *superposition* thereof. Furthermore, quantum physics allows for profound correlations between two qubits, which is called *entanglement* and is not possible in classical physics. The principles of superposition

and entanglement are the ingredients which make a quantum computer much more powerful than a classical computer.

The realization of a quantum computer requires the physical implementation of qubits. To this aim, several approaches have been pursued such as, e.g. cold-ion traps [3] liquid-phase nuclear spins [4] and atoms in optical lattices [5]. An important property of a qubit implementation approach is its scalability, i.e. the feasibility of fabricating large arrays of qubits within a relatively small space. A particularly promising approach, in this regard, was proposed by Loss and DiVincenzo in 1998 [6], where electron spins in solid state structures encode qubits, hence also called *spin-qubits*. In addition, this approach is interesting because the fabrication techniques of such solid state qubits have similarities to the well established semiconductor fabrication technologies, which could therefore be adapted and used for the fabrication of solid state qubit systems. Early realizations of solid state qubits were shown in III-V heterostructures such as GaAs. In 1996 Tarucha et al. have investigated a few-electron quantum dot and observed shell-filling effects [7]. Moreover, qubit initialization and read-out [8] and coherent manipulation of spin states [9] was shown. However, it soon became clear that qubit coherence is intrinsically limited in these III-V materials, which turned out to be associated to the interaction of the nuclear spins with the electrons, also called hyperfine coupling. This understanding triggered the search for new materials with fewer/no nuclear spins. The elements from group IV of the periodic table generally consist of isotopes with no nuclear spins and the natural abundance of spin-containing isotopes is rather small. Hence, elements like carbon (C), silicon (Si) and germanium (Ge) are promising candidates for hosting materials of long-coherence spin-qubits.

The first part of this thesis focuses on the investigation of quantum states of matter in graphene systems. In particular, narrow strips of graphene, also called graphene nanoribbons (GNRs), are predicted to exhibit interesting physical phenomena. A few examples are ferro- and anti-ferromagnetic electron spin-order [10], helical states and topological phases containing Majorana fermions [11] and spin qubits in quantum dots

(QDs) [12]. According to the crystal lattice of graphene, two main crystallographic directions exist: zigzag (ZZ) and armchair (AC). The above mentioned phenomena are expected only for crystallographic ribbons following either one of these directions, and, very importantly, the edges need to be of high quality. Several different fabrication techniques have been investigated to achieve edge qualities as high as possible. The work presented in this thesis follows an approach where an anisotropic etching method of graphite and graphene in a hydrogen (H) plasma is developed and investigated. Furthermore, characterization of the H plasma defined graphene edges is performed by means of Raman spectroscopy, atomic resolution atomic force microscopy (AFM), and low-temperature electronic transport measurements.

In the second part of this thesis, Ge/Si core/shell nano wires (NWs) are investigated as potential hosts for spin-qubit experiments. As mentioned above, both Si and Ge have a low abundance of non-zero nuclear spins and are, thus, promising candidates for spin-qubits with long coherence times. In addition to the small hyperfine coupling, theoretical predictions suggest a strong and tunable spin-orbit interaction (SOI) of Rashba type, which is called direct Rashba SOI (DRSOI) [13]. The large SOI enables fast and all-electrical spin manipulation, which is an important ingredient for quantum computation schemes. Moreover, helical modes and phases hosting Majorana fermions are theoretically predicted [13]. Next to the strong and tunable SOI, an anisotropic and tunable g-factor is predicted [14], and was observed in experiment [15]. A tunable g-factor is especially interesting because it allows for selectively tuning the coupling to externally applied electrical driving fields. All of the above mentioned properties make Ge/Si core/shell NWs a promising platform for the realization of spin-qubits. The work presented in this thesis focuses on the investigation of QDs of different sizes, which can be tuned to low occupation numbers. Furthermore, double and triple QDs can be formed and Pauli spin blockade (PSB) is observed in the double QD regime.

This thesis is organized as follows:

- **Chapter 2:** In this chapter the theoretical and experimental background for the experiments presented in this thesis is addressed. In a first part, the structure and properties of graphene are explained. GNRs are introduced and a brief review of fabrication methods and their results is given. The generation of a H plasma and possible reaction mechanisms of H radicals with graphitic species is explained. Moreover, the working principle of Raman spectroscopy and its use for insight into the quality of graphene edges is discussed. In addition, electronic transport in graphene samples and the formation of pn-junctions is addressed. Furthermore, sample fabrication techniques and methods are presented.

  In a second part, Ge/Si core/shell NWs are introduced and a brief review of important experimental achievements in the field is given. Moreover, single and double QDs are addressed and the mechanism of PSB is explained.

- **Chapter 3:** Presentation of the experimental results on anisotropic etching of graphite and graphene in a remote H plasma. Important etching parameters such as pressure, sample-plasma distance, and substrate influence are identified.

- **Chapter 4:** Based on the findings presented in chapter 3, graphene nano structures are fabricated by means of anisotropic etching in a remote H plasma. Their edges are investigated with atomic resolution AFM, Raman spectroscopy and low-temperature electronic transport measurements.

- **Chapter 5:** In this chapter low-temperature transport experiments in Ge/Si core/shell NWs are presented. In particular, the formation of single QDs of different sizes and the formation of double and triple QDs is shown. In the double QD regime, PSB is observed.

- **Chapter 6:** Summary of presented work and outlook on future experiments.

2 Theoretical and Experimental Background

2.1 Graphene

Graphene is a truly two-dimensional material composed of carbon atoms arranged in a honeycomb lattice. It is the basic building block for further carbon allotropes like graphite, carbon nano tubes and fullerenes. First, it was believed that a single layer (SL) of graphene would be thermodynamically unstable and hence not possible to isolate in a free state [16, 17]. Nevertheless, it was extensively investigated in theory [18–20]. Finally, in 2004 A. K. Geim and K. S. Novoselov showed for the first time that it is possible to isolate a single layer of graphene [21]. This discovery triggered experimental graphene research in many research groups around the globe.

Graphene turned out to be an extraordinary material for fundamental research and holds great potential for practical applications. Despite the fact that graphene is only one atom thick, it exhibits outstanding mechanical strength [22]. Furthermore, graphene shows exceptionally high thermal [23] and electric conductivities [21, 24]. The charge carriers in graphene behave as massless Dirac fermions which leads to many interesting physical phenomena such as e.g. the anomalous quantum Hall effect [25] and the Klein paradox [26].

2.1.1 Structure and Properties of Graphene

A free standing carbon atom has the chemical configuration $1s^2 2s^2 2p^2$. As carbon atoms are brought together to form graphene, the $2s$ and $2p$-orbitals hybridize and form three sp^2-orbitals and one p-orbital (see Fig. 2.1 (a)). The sp^2-orbitals form the σ-bonds and lie in a plane where they have $120\,^\circ$ angles in between them, which leads to the hexagonal lattice shown in Fig. 2.1 (b). It can be seen as two inter-penetrating triangular lattices with a two-atomic unit cell spanned by the unit vectors

$$\vec{a_1} = \frac{a_0}{2}\begin{pmatrix} 3 \\ \sqrt{3} \end{pmatrix} \qquad \text{and} \qquad \vec{a_2} = \frac{a_0}{2}\begin{pmatrix} 3 \\ -\sqrt{3} \end{pmatrix} \tag{2.1}$$

where $a_0 = 1.42\,\text{Å}$ is the distance between two adjacent carbon atoms. The corresponding Brillouin zone is depicted in Fig. 2.1 (c) with the reciprocal lattice vectors

$$\vec{b_1} = \frac{2\pi}{3a_0}\begin{pmatrix} 1 \\ \sqrt{3} \end{pmatrix} \qquad \text{and} \qquad \vec{b_2} = \frac{2\pi}{3a_0}\begin{pmatrix} 1 \\ -\sqrt{3} \end{pmatrix} \tag{2.2}$$

and the high symmetry points Γ, M, K' and K. The p-orbitals form the conductive π and π^* bands in which the charge carriers are delocalized over the hole graphene sheet. The corresponding band structure was first calculated by Wallace [18] with a tight-binding approach and is sketched in the following, based on ref. [27].

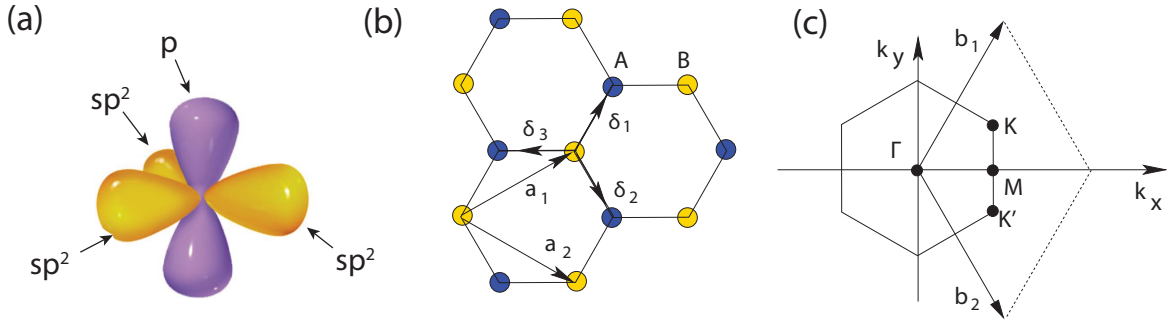

Figure 2.1: Graphene crystal lattice and Brillouin zone. (a) Atomic orbitals of sp^2-hybridized carbon atoms. Fig. taken from [28]. **(b)** Crystal lattice of graphene. The two-atomic unit cell with A (blue) and B (yellow) atoms is spanned by the unit vectors $\vec{a_1}$ and $\vec{a_2}$ and the nearest-neighbor vectors $\vec{\delta}_{1,2,3}$ are indicated. **(c)** Brillouin zone of graphene. The high symmetry points Γ and M and the two in-equivalent valleys K and K' are marked. $\vec{b_1}$ and $\vec{b_2}$ are the unit vectors in reciprocal space. Fig. in panel (b) and (c) are taken from [27].

The charge carriers in the p-orbitals can hop to their nearest-neighbor sites

$$\vec{\delta_1} = \frac{a}{2}\begin{pmatrix} 1 \\ \sqrt{3} \end{pmatrix} \qquad \text{and} \qquad \vec{\delta_2} = \frac{a}{2}\begin{pmatrix} 1 \\ -\sqrt{3} \end{pmatrix} \qquad \text{and} \qquad \vec{\delta_3} = -a\begin{pmatrix} 1 \\ 0 \end{pmatrix} \tag{2.3}$$

and the next-nearest-neighbors $\vec{\delta}_1' = \pm\vec{a_1}$, $\vec{\delta}_2' = \pm\vec{a_2}$ and $\vec{\delta}_3' = \pm(\vec{a_2} - \vec{a_1})$. The corresponding tight-binding Hamiltonian reads

$$H = -t \sum_{\langle i,j\rangle,\sigma} (a^\dagger_{\sigma,i} b_{\sigma,j} + h.c.) - t' \sum_{\langle\langle i,j\rangle\rangle,\sigma} (a^\dagger_{\sigma,i} a_{\sigma,j} + b^\dagger_{\sigma,i} b_{\sigma,j} + h.c.) \tag{2.4}$$

where $a_{\sigma,i}$ annihilates and $a^\dagger_{\sigma,i}$ creates an electron with spin $\sigma =\uparrow$ or $\sigma =\downarrow$ on site R_i on sublattice A (equivalent notation for sublattice B). t and t' denote the nearest-neighbor and the next-nearest-neighbor hopping energies, respectively. Note that units were used such that $\hbar = 1$. The resulting energy bands are given by:

$$E_\pm(k) = \pm t\sqrt{3 + f(k)} - t' f(k) \tag{2.5}$$

where $f(k)$ is given by

$$f(k) = 2\cos\Big(\sqrt{3}k_y a\Big) + 4\cos\left(\frac{\sqrt{3}}{2}k_y a\right)\cos\Big(\frac{3}{2}k_x a\Big) \tag{2.6}$$

The corresponding dispersion relation is plotted in Fig. 2.2 (a). In panel (b) a 2D-representation of the dispersion relation is shown here for a system at the charge neutrality point.

An expansion close to the K' or K point ($k = K + q$ with $|q| \ll |K|$) leads to the following expression

$$E_\pm(q) \approx \pm v_F|q| + \mathcal{O}(q/K)^2 \tag{2.7}$$

where $v_F = 3ta/2 \simeq 1 \cdot 10^6\, m/s$ is the Fermi velocity. Hence, the dispersion relation of the charge carriers in graphene can be well approximated by a linear function at low energy and q values, respectively (see inset of Fig. 2.2 (a)). The conduction and valence bands touch each other at zero energy in six points whereof two are different from each other (K and K'). This leads to the so-called valley degeneracy of two in addition to the

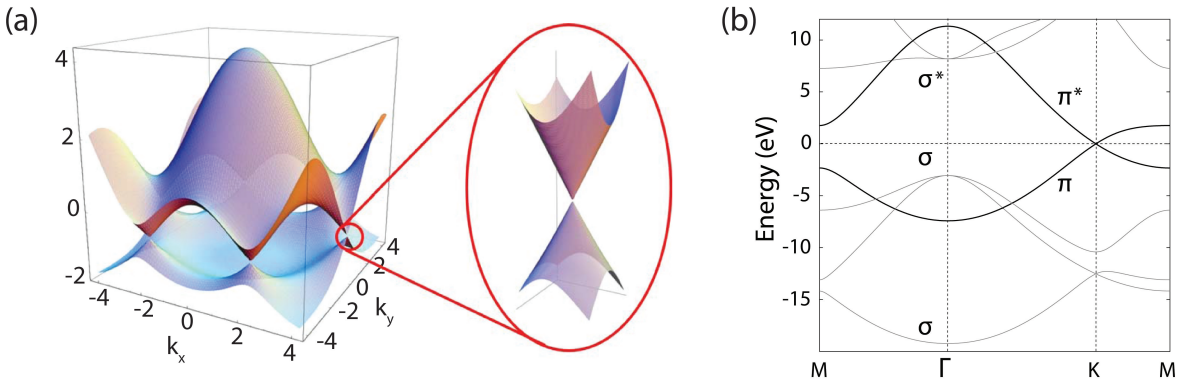

Figure 2.2: Tight-binding band structure of graphene. (a) Calculated energy bands in units of t for $t = 2.7\,\mathrm{eV}$ and $t' = -0.2\,t$. The zoom-in shows the region close to a Dirac point where the linear nature of the dispersion relation is visible for small energy values. Fig. adapted from [27]. **(b)** Dispersion relation of graphene where the bonding σ-bands and anti-bonding σ^*-bands are shown in gray and the π and π^*-bands are shown in black. The Fermi energy is indicated by the horizontal dashed line. Fig. taken from [29].

spin degeneracy which also counts two. Graphene is a zero-gap semiconductor where the Fermi level can be tuned, for example by electric field gating, continuously from holes to electrons or vice versa. This allows charge carriers to travel across regions of different polarity (pn-junctions) which are electronic counter parts to semi-transparent mirrors in classical optics and hence enable to perform many exciting electron-optic experiments, some of which are discussed in more detail in section 2.1.5. Due to its high electronic quality, graphene was considered as a suitable material to build transistors. However, the absence of an electronic band gap disables the possibility to tune the transistor into an off-state. This obstacle can in principle be overcome if graphene is cut into narrow stripes (GNRs) where the spatial confinement is expected to lead to the opening of a band gap. Furthermore, many theoretical proposals which predicted the appearance of interesting physical phenomena in GNRs with crystallographic edges motivated the research in this field. In the following section, an overview of GNR fabrication methods and the experimental findings will be given.

2.1.2 Graphene Nano Ribbons

If graphene is laterally confined into a narrow strip, where the width of the strip is equal or smaller than the Fermi wavelength of the charge carriers, it forms a quasi-1D structure, also called GNR. Interestingly, the electronic properties of GNRs depend strongly on the nature of their edges. According to the graphene crystal lattice structure, there are two types of crystallographically clean edge types: Zigzag (ZZ) and armchair (AC). Fig. 2.3 (a) shows the lattice structure of a ZZ-GNR and in panel (b) the corresponding electronic band structure is plotted for different ribbon widths (N = 4, 5, 6; where N corresponds to the number of ZZ lines). As seen in the Fig., the highest valence band and the lowest conduction band touch each other at zero energy and turn into essentially flat bands, thus producing a peak in the density of states.

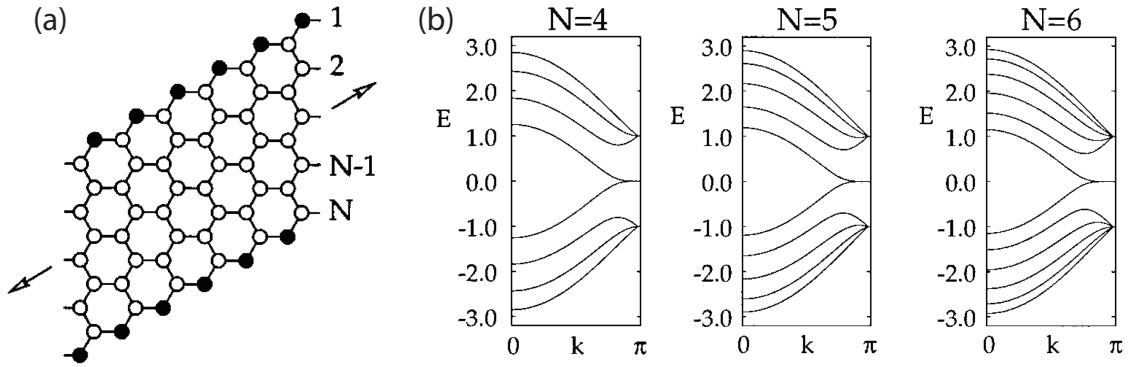

Figure 2.3: Crystal structure and tight-binding band structure of a ZZ-GNR. (a) Schematic of the crystal lattice structure of a ZZ-GNR. N denotes the width of the ribbon in amount of ZZ lines. **(b)** Tight-binding band structure calculations for ZZ-GNRs of different widths (N = 4, 5, 6). Fig. adapted from [27].

Taking electron-electron interactions into account, an electronic band gap opens and turns the otherwise metallic system into a semiconductor [29]. It turns out that these low-energy states are localized at the edges of the ribbon and give rise to magnetic ordering of the respective spin states [29]. In particular, the spins align parallel at each edge (ferromagnetic ordering) and anti-parallel between the two ribbon edges (anti-ferromagnetic ordering). These predictions have interesting implications which

triggered exciting proposals for the realization of e.g. spin-filters [30] and magnetic field sensors [31].

GNRs with edges of the AC type have fundamentally different electronic properties compared to ZZ-GNRs. Fig. 2.4 (a) shows the crystal structure of an AC-GNR and panel (b) shows the corresponding tight-binding band structures for different ribbon widths (N = 4, 5, 6; where N corresponds to the number of dimer lines). AC-GNRs change their electronic property from metallic to semiconducting, depending on the ribbon width. If the width is equal to $N = 3M - 1$, where $M \in \mathbb{N}$ the ribbon is metallic and semiconducting otherwise. In contrary to the ZZ case, there are no edge states present in AC-GNRs. Nevertheless, many interesting proposals based on AC-GNR systems exist as for example the realization of helical modes and Majorana fermions [11] and the implementation of spin quibits [12].

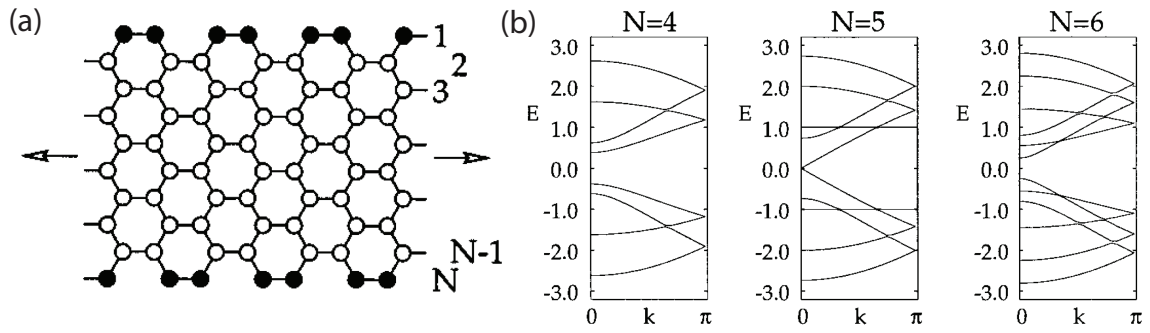

Figure 2.4: Crystal structure and tight-binding band structure of an AC-GNR. (a) Schematic of the crystal lattice structure of an AC-GNR. N denotes the width of the ribbon in amount of dimer lines. **(b)** Tight-binding band structure calculations for AC-GNRs of different widths (N = 4, 5, 6). Fig. adapted from [27].

For ballistic GNRs with perfect edges the conductance is expected to be quantized according to the sub-mode spacing arising due to the spatial confinement. For GNRs with AC edges the valley degeneracy is lifted and the theoretical predictions for the conductance exhibit steps of $2\,e^2/h$ because of the two degenerate spin channels. Ribbons of the ZZ type, on the other hand, have their valley and spin degeneracy conserved and are therefore expected to show steps of $4\,e^2/h$ [29, 32]. However, only a small amount of edge-disorder suppresses conductance quantization [33–35] and prevents the occur-

rence of interesting physical phenomena which were predicted to arise in systems with perfect edges. Hence, it is crucial to be able to fabricate GNRs with well-defined crystallographic orientations and low edge-disorder. It has proven to be very challenging to create GNRs which are sufficiently clean (in terms of bulk as well as edge-disorder) in order to observe the theoretically predicted physical effects in experiment. A number of different fabrication methods were attempted such as:

- Carbon nano tube unzipping [36, 37]
- Ultrasonication of intercalated graphite [38]
- Chemical bottom-up synthesis [39–45]
- Anisotropic etching by nickel nano particles [46]
- Anisotropic etching during CVD processing [47–50]
- Carbothermal etching of graphene sheets [51–54]
- Helium ion beam lithography [55, 56]
- TEM Nanosculpting [57]
- GNR growth on SiC step-edges [58]
- Current annealing of suspended GNRs [32]
- STM cutting [59]
- Hydrogen plasma etching [60–67]

Different fabrication techniques probably create different edge configurations and it is important to develop an understanding of this connection in order to optimize the edge quality towards perfectly clean crystallographic edges. In order to experimentally investigate graphene edges, a range of different methods is pursued. On the one hand, direct experimental imaging of graphene edges can be tried, while on the

other hand features in electronic transport measurements can be analyzed and used to draw conclusions about the edge quality and configuration. Visualization of the edges was attempted with different techniques such as TEM imaging [36, 57, 68–76], STM imaging [40, 62, 77–83] and more recently by means of tip-functionalized AFM imaging [84, 85] where even information on the chemical structure is possible. For each method there are advantages and disadvantages. For TEM investigations the samples need to be suspended on a special grid and the high energetic electrons can change the edge structure while imaging. For STM experiments, on the other hand, conductive substrates are needed and the samples need a very clean surface. Indeed atomically resolved AFM imaging is a rather noninvasive method and does not require special sample preparation apart from proper cleaning of the investigated GNRs.

Another technique to gain information about the edge configuration is Raman spectroscopy. Since we used Raman spectroscopy for the investigation of graphene edges in the work presented in this thesis, the technique will be introduced in more detail in an own section 2.1.4.

Most fabrication methods in the list above turned out to produce disordered edges which are either a mixture of ZZ and AC segments or are disordered in such a way that not even small AC or ZZ segments are present at all. In electronic transport experiments, performed in narrow GNRs at low temperatures, this manifests itself in the occurrence of suppressed conductance and localization features such as Coulomb blockade diamonds [86–91]. However, in a small minority of electronic transport experiments or STM studies, indications of conductance quantization or other edge related physics were observed. These experiments will be briefly described in the following.

- **Quantized conductance**

  Tombros et al. [32] have shown transport through a suspended and current-annealed GNR at zero magnetic field which exhibited indications of conductance plateaus arising from the spatial confinement. However, to my knowledge, it was not possible to fabricate such devices in a reproducible manner.

Another experiment performed by Baringhaus et al. [58] showed high conductance through the first mode of a GNR grown on a SiC step-edge. No localization features were observed and the authors claimed ballistic transport over a distance of 16 μm at room temperature. However, the underlying transport mechanism is not yet fully understood and it is not exactly clear how the SiC substrate influences the transport properties of the ribbons.

In another publication the ability to fabricate GNRs on SiC sidewalls with certain dimensions and edge shapes (ZZ and AC terminations) is presented [92].

In a more recent work [93] transport through GNRs epitaxially grown on the sidewalls of SiC mesa structures is investigated in a spatially-resolved two-point probe setup. This allows to selectively access and directly image a range of individual transport modes which give rise to a sequence of quantized conductance plateaus. The individual transport modes are believed to result from an interplay between edge-magnetism and asymmetric terminations at opposite ribbon edges due to the underlying SiC structure morphology.

Size quantization of Dirac fermions was observed in graphene constrictions encapsulated in two hexagonal boron nitride (hBN) flakes [94]. At high charge carrier densities, clear quantization features are present, while at lower densities deviations from the ballistic transport behavior allow for probing the density of localized states at the edges. The edges of these devices were defined with reactive ion etching (RIE) and presumably have a relatively high degree of edge disorder, which probably turns the quantization features into kinks in the conductance rather than clean plateaus.

- **Edge states**

  Ruffieux and coworkers [39–42] have developed bottom-up fabrication methods where chemically synthesized ribbons with atomic precision are created. By means of STM they map the local density of states and observe edge states which could potentially be spin polarized according to theoretical predictions [95].

- **Magnetic ordering**

  Narrow GNRs with well defined crystallographic orientations and low edge disorder are fabricated with a STM cutting method [59]. Scanning tunneling spectroscopy is performed on ZZ edged GNRs where a semiconductor-metal transition is observed as the ribbon width is increased. This is in agreement with theoretical expectations which predict the opening of a band gap and the occurrence of magnetic ordering of the edge states for narrow ribbons due to electron-electron interactions. As the ribbon width exceeds a certain threshold, the intra-edge coupling becomes too small and the system turns metallic, presumably resulting in the loss of its magnetic structure. It is noteworthy that these effects were observed at room temperature.

The work presented in this thesis focuses on the approach to fabricate GNRs with high quality crystallographic edges by means of anisotropic etching of graphite and graphene in a remote H plasma [60–67]. The generation methods and properties of such a H plasma are explained in the next section 2.1.3.

2.1.3 Hydrogen Plasma

Already in 1970 McCarroll and McKee have investigated the reactivity of graphite surfaces with atoms and molecules of H, oxygen and nitrogen [60, 61]. They found graphite exposed to *molecular* H and nitrogen to be inert in a temperature range from 300 °C - 1200 °C. Interestingly, *atomic* H and nitrogen lead to the appearance of hexagonal etch pits on the graphite surfaces upon exposure. It was found that hexagons created with H atoms have sides parallel to the ZZ direction of the crystal lattice, whereas atomic nitrogen produces hexagons oriented along the AC direction.

While both, ZZ and AC terminated GNRs are in principle interesting for their own, different reasons, we focus on the fabrication of ZZ edges in this thesis. Hence we need to have a source of atomic H to perform the desired etching along the ZZ direction. One possibility to produce atomic H is to employ a H plasma. In the following a brief

description will be given of how such a H plasma can be generated and of which plasma species it is composed of. Furthermore, possible reaction mechanisms of graphite with atomic H will be discussed.

Generation of Hydrogen Plasmas

A H plasma can be generated by using a surface launcher, also called surfatron, which is mounted on the outside of a plasma chamber (e.g. a quartz tube). The generation method via a surfatron has several advantages over other plasma generation methods as e.g. the positive column of a DC discharge. Namely, no electrodes are in direct contact with the plasma which could lead to gas contamination and electrode corrosion. Furthermore, the relatively small surfatron allows to generate long plasma columns without the need of axial magnetic fields or external structure extending along the entire chamber. Moreover, it works over a large frequency range, has a low rate of electron density fluctuation, exhibits high stability and is reliably reproducible. Fig. 2.5 (a) shows a photograph of the used quartz tube with the surfatron. In panel (b) a schematic of the setup is shown.

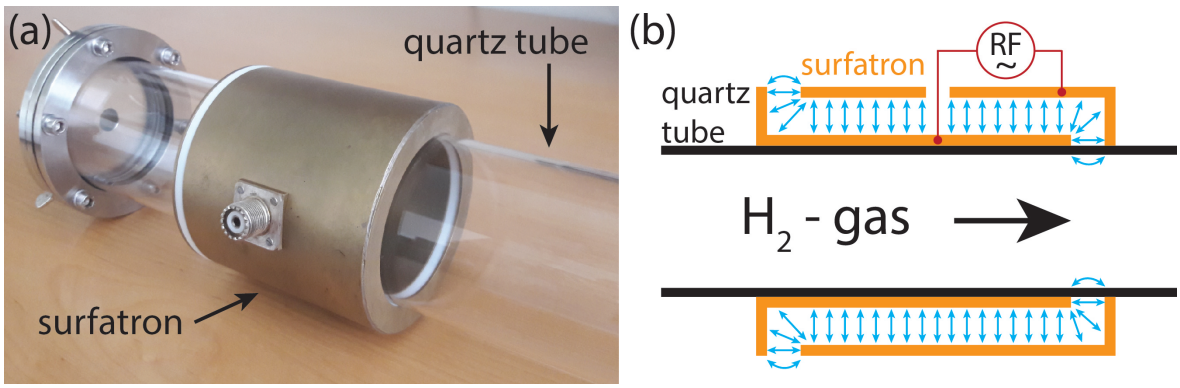

Figure 2.5: Plasma generation with a surfatron. **(a)** Photograph of the Suprasil quartz tube with the surfatron mounted. **(b)** Schematic of the plasma setup. The blue arrows indicate the electric RF field oscillating between the outer and inner plates of the surfatron.

A surface wave plasma is generated by coupling a radio frequency (RF) signal over the surfatron to the gas molecules in the quartz tube. The oscillation of the electric RF field induces waves which have their charges in the plasma compensated by polarization

charges in the dielectric material, i.e. in the quartz tube. These waves can travel along the interface between the plasma and the quartz tube and sustain the plasma also away from the surfatron. In MHz discharges as ours (13.56 MHz) the condition $\omega_{pi} < \omega_{RF} < \omega_{pe}$ is fulfilled, with ω_{pi} and ω_{pe} being the plasma frequency of the ions and electrons, respectively. This means that the ions are too slow to follow the electric field oscillations, whereas the electrons move with the applied RF frequency. When the moving electrons scatter with the neutral gas particles, they get out of phase with the applied electric field. This process allows the electrons to gain energy until ionization and plasma ignition occurs. As the surface wave travels along the plasma/quartz tube interface away from the surfatron, it transfers energy into the gas and thereby ionizes it and sustains itself. Due to scattering events of the electrons with ions and neutrals and scattering at the quartz tube walls, the energy of the surface wave decreases with the distance from the surfatron. This leads to a linear decrease of the electron and ion density away from the surfatron, until the energy is too low to sustain the discharge, leading to the breakdown of the plasma column. Hence, the plasma column length can be tuned with the applied RF power, in particular longer plasma columns can be generated with higher power. Another parameter which influences the length of the plasma column is the gas pressure inside the quartz tube. The gas pressure influences the amount of scattering events which in turn is proportional to the amount of energy loss of the surface wave. In particular, a higher pressure would lead to more scattering and higher energy loss and therefore a shorter plasma column would result.

In a H plasma as described above, the following species are present: H_2, H, H^+, H_2^+, H_3^+, electrons and higher vibrational states of the respective molecules. Basically, two plasma regimes can be distinguished, the *direct* and the *remote* plasma (see Fig. 2.6).

In the direct plasma regime, the surface wave energy is large enough to sustain the discharge and ionization takes place which leads to the optically visible glow. The remote plasma regime, on the other hand, lies downstream of the glowing part where the surface wave has not enough energy anymore to ionize the H gas. In the direct plasma

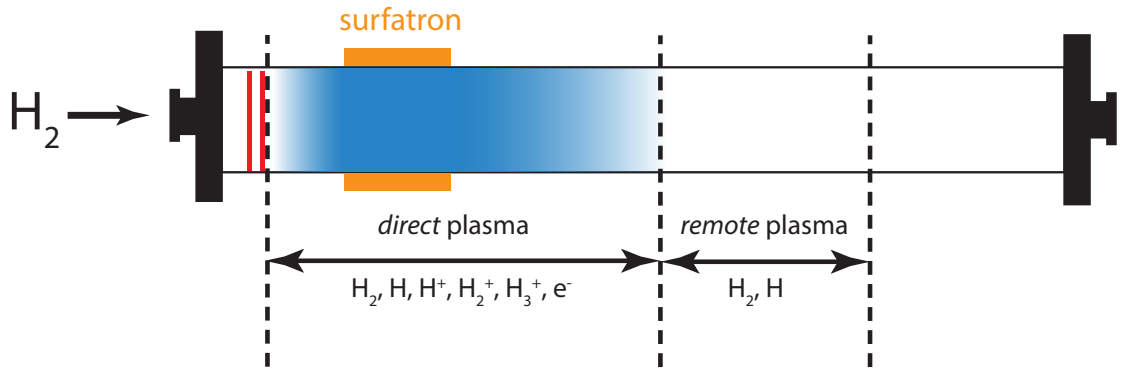

Figure 2.6: Direct and remote plasma regions. The direct and remote plasma regions are marked with the molecular and ionic species present in the respective regions. The red strips are glass plates which hinder the plasma to interact with the metallic closures of the quartz tube plasma chamber.

regime, all the above mentioned species are present. In the remote plasma regime, the abundance of the individual species depends on the respective recombination rate. Ions and electrons recombine relatively efficiently inside the gas, whereas the collision of H radicals needs a third body to carry away the excess energy for recombination. Hence the recombination of H radicals mainly takes place at the tube walls and depends strongly on the material of the plasma tube. It was found that quartz has a relatively low H radical recombination coefficient [96, 97] which makes it possible to create a region where essentially all ions have already recombined and only H radicals and molecules are present, as needed for the desired etching effect. The influence of the sample positioning, regarding the direct/remote plasma regions, on the etching character and the optimization of the plasma parameters in order to reach etching conditions which are useful to fabricate graphene nano structures with well defined edges is subject of the work presented in section 3. In the next section, possible reaction mechanisms of H radicals with graphitic material are discussed.

Reaction Mechanisms of Hydrogen Radicals with Graphite and Graphene

If graphite or graphene is exposed to a remote H plasma an anisotropic etching effect can be observed. This anisotropic etching manifests itself in the formation of hexagonal

shaped etch pits. Interestingly, the etching takes place only at preexisting defects or trenches and leaves the basal plane untouched. The formation of hexagonal etch pits upon exposure to remote H plasma was observed in many experiments [60–63, 65–67] and is believed to be based on a chemical reaction of H radicals with the graphitic material. However, the reaction mechanism which leads to the anisotropic etching is not exactly known and different ideas and speculations exist. In the following, two possible reaction mechanisms are described in detail. The first mechanism is sketched in Fig. 2.7 where the four reaction steps are labeled with red numbers and are discussed in the sequence of reaction: (1) Starting from a two-carbon entity of the graphene plane, the impact of H radicals leads to the breakage of the C-C double bond and the hydrogenation of the left C atom which thereby undergoes an sp^2 to sp^3 transformation. The other C atom of the former double bond remains in an sp^x state as only one of the carbon atoms can be hydrogenated at a time. (2) Multiple hydrogenation steps can lead to the intermediate product at the top of the Fig., featuring a methyl group. (3) Further impact of H radicals leads to the release of molecular H and the formation of the intermediate product shown on the right of the Fig. (4) For temperatures above 400 K the methyl group can split-off and a fresh C-C double bond is formed.

This last step incorporates the removal of a C-atom-containing-species and therefore to the chemical erosion of the graphene sheet. This could explain how etching of graphene under H radical impact happens in general, but gives no lead why the etching could form straight edges and be anisotropic. The next described mechanism incorporates ideas of how the etching could form straight lines with low edge roughness, as it would be desired for the fabrication of crystallographic GNRs.

In Fig. 2.8 an etching mechanism proposed by Davydova et al. [99] is shown. The mechanism is based on a molecular dynamics study of a ZZ GNR in a downstream H plasma, as it was used in the studies presented in section 3 and 4 and can be subdivided into three phases: *Phase 1:* The GNR edges are hydrogenated and form C-H and C-H_2 groups (see panel (a) to (c)). This lowers the surface potential barriers

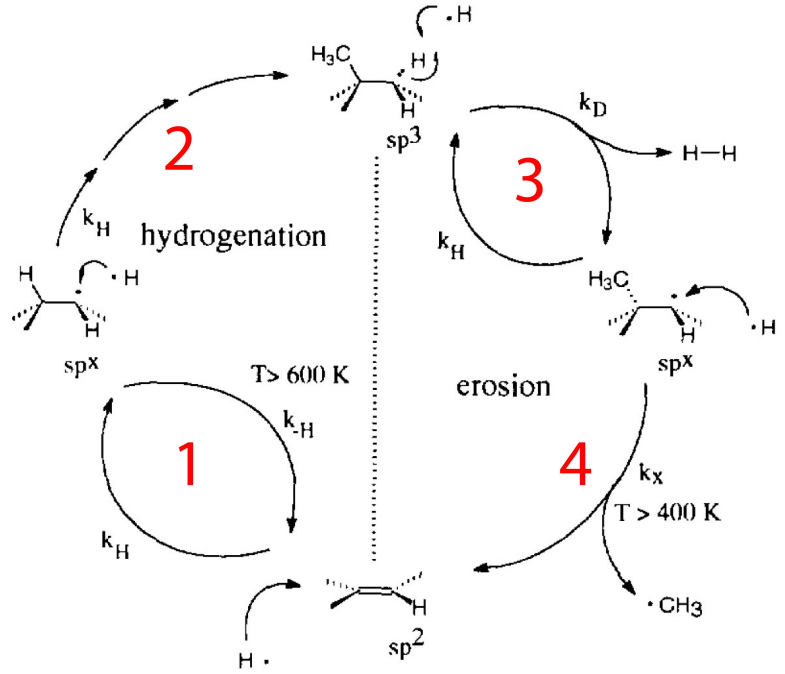

Figure 2.7: Possible reaction mechanism of H radicals with graphitic material. On the left hand side hydrogenation of carbon atoms is sketched and on the right hand side the chemical erosion of graphite via the release of a methyl group is shown. The red numbers indicate the four reaction steps between the intermediate products. Fig. adapted from [98].

for H chemisorption on inner C atoms from the 1st and 2nd carbon rows. Thus, hydrogenation of C-C dimers from the 1st and 2nd rows takes place and leads to stress between the fist two carbon rows, initiating phase 2. *Phase 2:* The increasing stress between the 1st and 2nd carbon rows finally leads to the rupture of C-C dimer bonds and unzipping of the 1st row from the 2nd carbon row (see panel (d) to (i)). *Phase 3:* If the suspended carbon rows reach a critical length regarding their stability, they rupture. The ruptured C chains are bombarded by impinging H atoms and are successively sputtered away (see panel (j) to (n)). This mechanism leaves straight edges with a low line edge roughness and would be desirable to realize in experiment.

As discussed above, the quality of the edges of GNRs is essentially determining the electronic properties of the systems and thus important to control and characterize. A rather straight forward and quite powerful method to gain information on the quality of graphene edges is Raman spectroscopy which is explained in the next section 2.1.4.

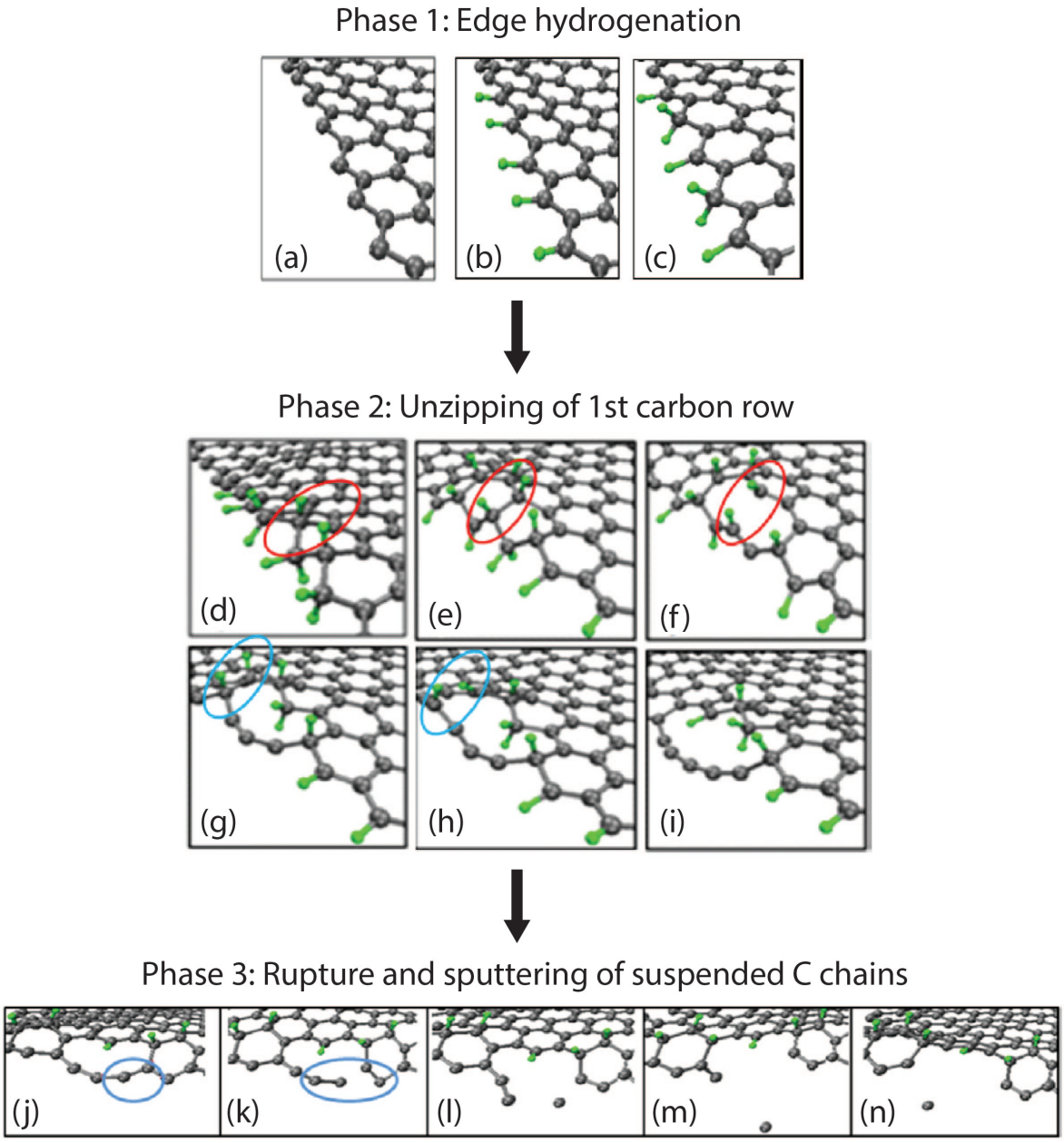

Figure 2.8: Possible reaction mechanism of GNR etching in a downstream H plasma. **(a)** to **(c)** Phase 1 of the etching mechanism where hydrogenation takes place , indicated with the greed spheres being H atoms bound to the edge C atoms. **(d)** to **(i)** Phase 2: hydrogenation of inner C atoms and unzipping of the 1st from the 2nd carbon rows. The red and blue ovals highlight regions where a C-C dimer ruptures. **(j)** to **(n)** Phase 3: Rupture and sputtering of suspended C chains. The blue ovals highlight the location at which the C chain ruptures. Fig. adapted from [99].

2.1.4 Raman Spectroscopy

Raman spectroscopy is a versatile tool for the surface investigation of many different materials and sample types (e.g. biological samples, solid state samples). In particular, it can be used to investigate carbon materials such as graphite [100], carbon nanotubes [101], fullerenes [102] and graphene [103]. Raman spectroscopy of graphene can provide information on many important properties of graphene such as e.g. the number of layers [104], the amount of defects [105, 106], the chirality and quality of edges [52, 107–109], strain [110, 111], electronic doping [112, 113] and bulk hydrogenation [114].

The Raman spectrum of graphene exhibits three main peaks which are important for gaining information on the above mentioned quantities: the G-peak, the D-peak and the 2D-peak. The according processes are shown in Fig. 2.9. Basically all Raman processes include the creation of an electron-hole pair upon laser irradiation, the interaction with one or more phonons and the subsequent recombination of the electron-hole pair which leads to the emission of light. Since the inelastic scattering with phonons leads to energy loss of the electron (or the hole), the emitted light has a lower frequency compared to the light which was used to excite the electron-hole pair. This shift in light frequency is called Raman shift and is characteristic for the material and the specific lattice vibrations thereof. In the following the three main peaks of the graphene spectrum are explained in detail.

The G-peak arises due to an inelastic first order Raman scattering process, as shown in Fig. 2.9 (a). The excited electron-hole pair interacts with the doubly degenerate phonon modes (iTO and iLO) at the Brillouin zone center, i.e. at the Γ-point (see Fig. 2.10 (c)). These two phonon modes are in-plane vibrations of sp^2-bonded carbon atoms and are schematically depicted in Fig. 2.10 (a). The corresponding Raman shift of the G-peak is $1580\,\mathrm{cm}^{-1}$. The G-peak intensity holds information about the presence and amount of graphene, i.e. if properly calibrated it can be used to deduce the number of graphene layers present in a sample [116]. However, the line shape of the 2D-peak is a more common used criterion for the determination of the number of graphene layers,

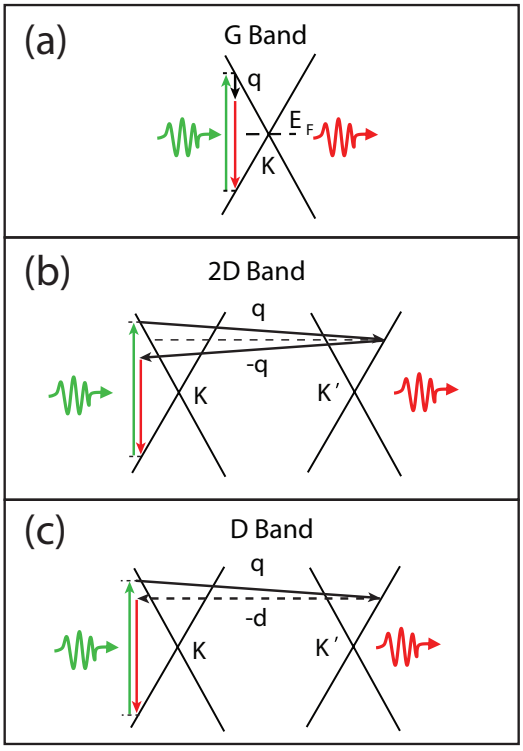

Figure 2.9: Raman processes in graphene. **(a)** G-mode Raman process depicted in k-space. The green arrows denote the incoming laser light and the excitation of the electron-hole pair, q stands for the momentum of the phonon and E_F is the Fermi energy of the system. The process takes place close to the middle of the Brillouin zone (the Γ-point). **(b)** 2D-mode Raman process with the K and K' points. The black arrows indicate the inelastic scattering events of the electron with the phonons. **(c)** D-mode Raman process. The solid arrow indicates the inelastic scattering event with an iTO phonon and the dashed arrow denotes an elastic scattering event with a defect or the edges. Fig. adapted from [115].

as described below. Furthermore, the width of the G-band can be used to measure the deformation and strain on a sample [111].

The 2D-peak is activated by an inelastic double resonance Raman process with two iTO phonons sitting close to the K-point, as indicated in Fig. 2.9 (b) and Fig. 2.10 (c). The lattice vibrations of the iTO phonons are schematically shown in Fig. 2.10 (b) and remind of a breathing-like mode of the carbon rings. The according Raman shift is dispersive and measures $\sim 2700\,\mathrm{cm}^{-1}$ for a laser excitation energy of 2.41 eV. The 2D-peak reflects the electronic band structure of graphene which allows to distinguish between SL graphene (a single Lorentzian), bilayer (BL) graphene (four Lorentzians) and graphite (two Lorentzians). Furthermore, the position of the 2D-peak holds information on the strain of graphene [110].

The D-peak originates from a double resonance Raman process with one inelastic scattering event with an iTO phonon around the K-point and one elastic scattering event with a defect or the edges (Fig. 2.9 (c) and Fig. 2.10 (b) and (c)). The corresponding Raman shift is $\sim 1350\,\mathrm{cm}^{-1}$, which is half of the 2D Raman shift. This is based on the fact that the D-mode only includes one inelastic phonon scattering event, whereas

the 2D-mode undergoes two scattering events with iTO phonons. The D-peak holds information on defect density, chirality and quality of the edges.

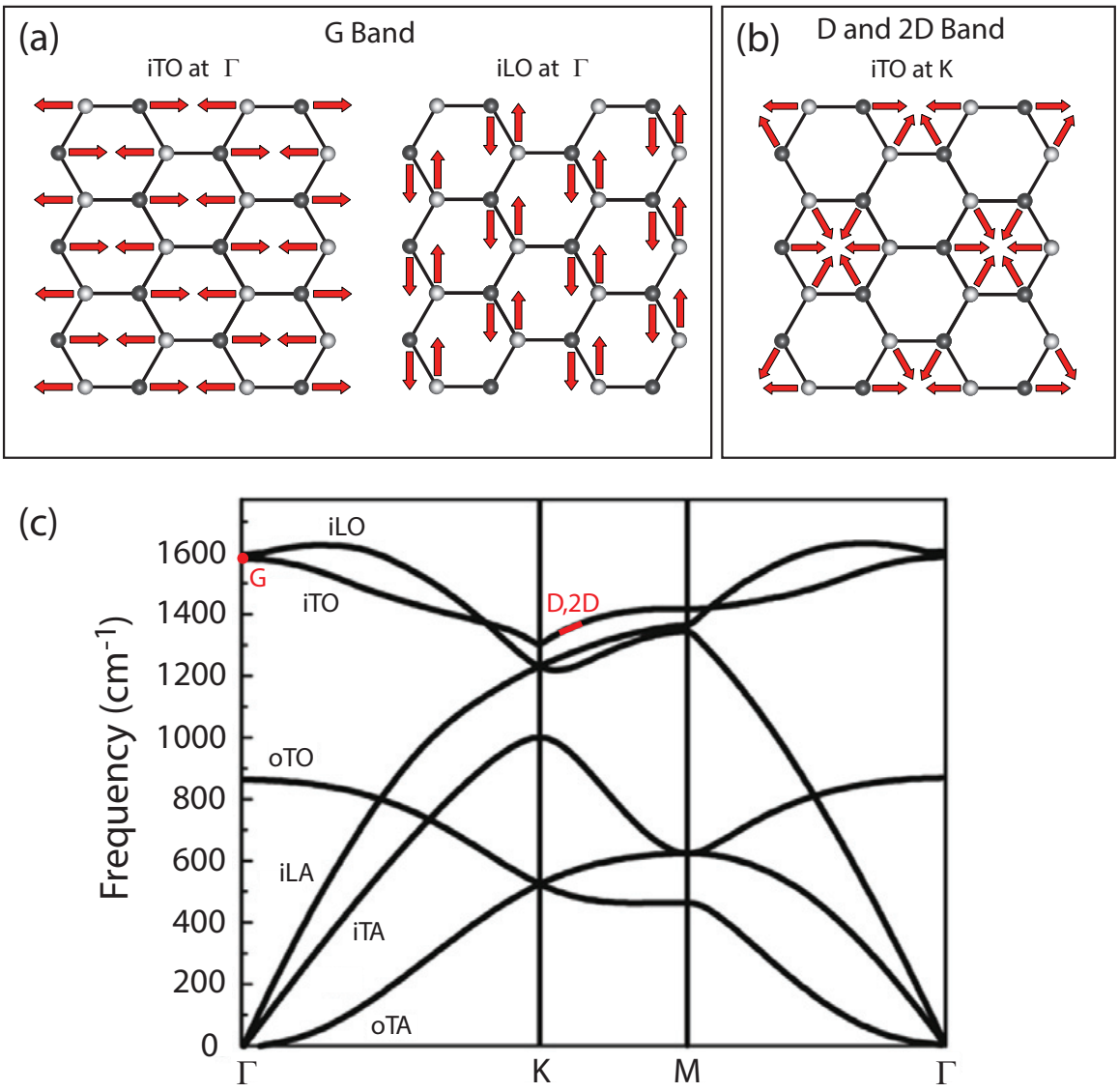

Figure 2.10: Graphene phonon modes and dispersion. **(a)** Schematic illustration of the lattice vibrations of the iTO and iLO phonons at the Γ-point which give rise to the Raman G-mode. **(b)** Illustration of the breathing-like lattice vibrations of the iTO phonons at the K-point which induce the D and 2D Raman modes. **(c)** Phonon dispersion relation of graphene with the six branches iLO, iTO, oTO, iLA, iTA, oTA where the first letter stands for in-plane (i) and out-of-plane (o), the second letter stands for longitudinal (L) and tangential (T), and the third letter stands for acoustic (A) and optic (O). The phonon states which are involved in the Raman processes for the G-, D- and 2D-peaks are indicated and labeled in red. Fig. adapted from [115].

Raman Spectroscopy at Graphene Edges

As mentioned above, Raman spectroscopy is a suitable tool to investigate the chirality and quality of graphene edges. Since Raman spectroscopy was used for this purpose in the work presented in this thesis (mainly in section 4), the aspect of edge-characterization by means of Raman spectroscopy will be described in the following. The information about the chirality and quality of the edge is captured in the D-peak of the Raman spectrum. After the incoming laser light has excited an electron-hole pair and an inelastic scattering process has sent the electron (or the hole) to the other valley, an elastic scattering process with the right momentum direction and absolute value is needed to complete the round trip in k-space and send out light with the according red-shift, giving rise to the D-peak. The elastic scattering process can happen at a graphene edge and has different momenta for ZZ and AC edges (see Fig. 2.11 (a)). Whereas an AC edge is able to connect the two valleys in k-space, the momentum associated to the scattering event happening at a ZZ edge has a different direction, which does not allow momentum conservation (see Fig. 2.11 (b) and (c)). Hence, scattering at a AC edge is D-peak active and scattering at a pure ZZ edge is D-peak inactive.

Thus, if a graphene edge exhibits no D-peak it can be concluded that the investigated edge is a pure ZZ edge. If, on the other hand, a finite D-peak intensity is measured, it is indicative of edge disorder and AC segments. Further information on the disorder type (point defects, AC segments of different orientations) can be obtained by polarized Raman studies [107, 117]. Different types of edge disorder have different polarization dependencies. Hence, it is possible to gain information on the relative weight of the different defect types by measuring the D-peak intensity as a function of the angle of the laser polarization relative to the edge. This method was applied to characterize H plasma defined graphene edges and the results are presented in section 4.

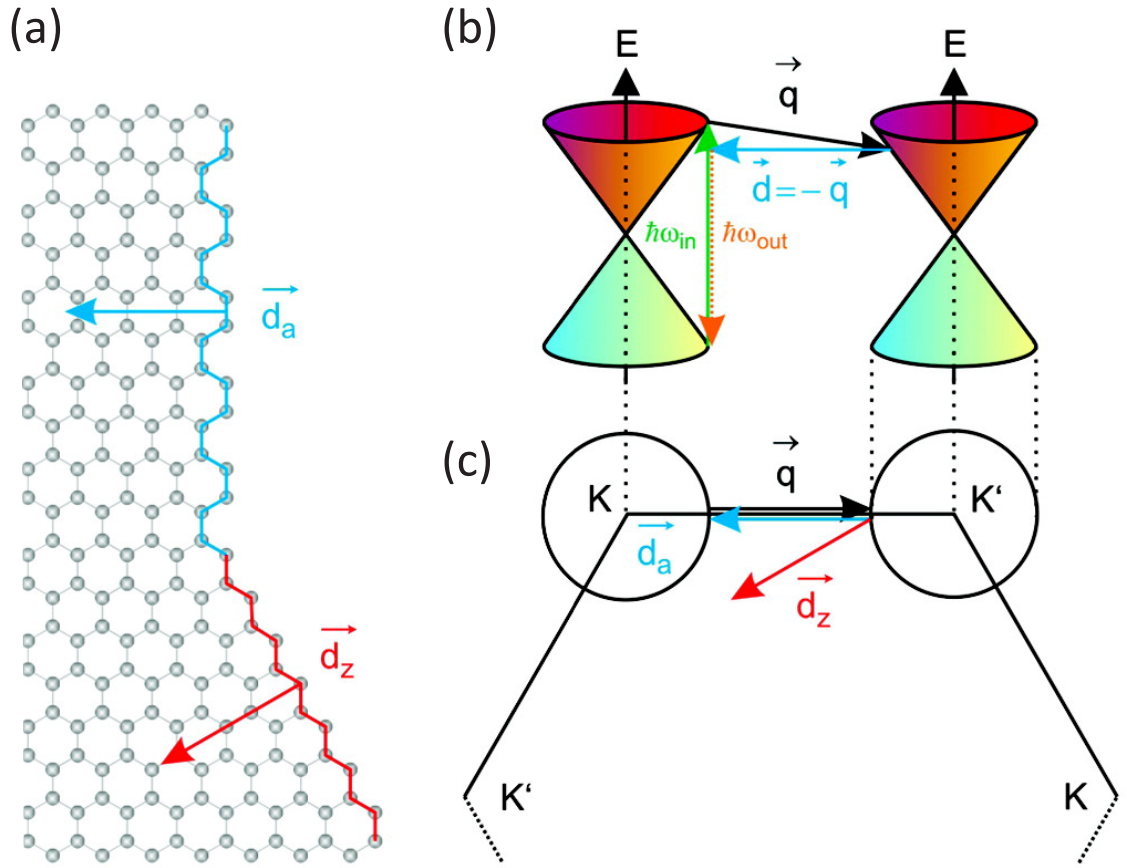

Figure 2.11: Raman scattering at pure graphene edges. **(a)** Schematic illustration of a section of a SL graphene flake with ZZ (red) and AC (blue) edges. $\vec{d_A}$ and $\vec{d_Z}$ denote the respective momentum vectors of the elastic scattering processes at the edge. **(b)** Schematic of the graphene dispersion relation close to the K and K' points, which are involved in the Raman D-mode process. The black vector $\vec{q}$ denotes the inelastic scattering with a phonon and the blue vector $\vec{d}$ indicates the momentum change due to an elastic scattering process at the edge. **(c)** Illustration of scattering processes taking place at a ZZ (red vector $\vec{d_Z}$) and a AC (blue vector $\vec{d_A}$) edge in k-space. The scattering event happening at an AC edge is able to connect the two valleys and therefore to give rise to a D-peak, whereas the ZZ edge does not fulfill momentum conservation and is D-peak inactive. Fig. taken from [52].

2.1.5 Electronic Transport

This section treats basic concepts and methods of electronic transport in graphene samples which were used in the work presented in this thesis. First, basic characterization methods and quantities are introduced, such as e.g. the conductivity, the mobility and the residual disorder density. Afterwards, an introduction to pn-interfaces will

be given and physical effects arising in such systems (e.g. Fabry-Pérot oscillations, valley-isospin oscillations) will be examined.

Electronic Characterization of Graphene Devices

Basically one can discriminate between the diffusive and the ballistic regime. In the diffusive regime, the path between two consecutive scattering events, also called the mean-free-path (l_{mfp}), is much smaller than the device dimensions (i.e. the distance between the contacts L or the width of the junction W). Hence the relation $l_{mfp} \ll L, W$ holds for the diffusive regime. In the ballistic regime, on the other hand, $l_{mfp} \geq L, W$; this case will be discussed further down. In the diffusive regime, the conductivity is given by the Drude model:

$$\sigma = \frac{ne^2\tau}{m} = \frac{2e^2\tau v_F\sqrt{\pi n}}{h} \tag{2.8}$$

where the relation $m = \hbar|\vec{k_F}|/v_F$ was used and e denotes the electronic charge, τ is the momentum scattering time, $\vec{k}$ the Fermi wave vector, v_F the Fermi velocity, h is Plancks constant and n is the charge carrier density. Depending on the nature of the scattering events, τ can have different dependencies on $|\vec{k_F}|$ [118]. Usually charge impurity scattering dominates and leads to a linear relation of the conductivity with the charge carrier density:

$$\sigma = \mu ne \tag{2.9}$$

where μ is the electronic mobility, a quantity which is often referred to regarding device cleanliness and performance. In experiment, the charge carrier density can be varied via the electric field effect by applying a voltage to a nearby gate. To convert gate voltage to charge carrier density, the so-called plate-capacitor model can be used. Thereby the conductive back gate and the graphene sheet are the two plates which are separated by a dielectric, here SiO_2 and a hBN flake. The corresponding relation reads:

$$n = \frac{\epsilon_d \epsilon_0}{de} \left(V_{bg} + V_{offset}\right) \tag{2.10}$$

where V_{bg} is the back gate voltage, V_{offset} is the offset voltage of the location of the charge neutrality point, ϵ_d and ϵ_0 are the dielectric constants of the material and free space, respectively. Hence, the conductance can be measured as a function of applied gate voltage which is then converted to charge carrier density using Equation 2.10, see Fig. 2.12 (a). An alternative possibility to convert back gate voltage to charge carrier density would be to use the following relation in the Hall regime:

$$n = \frac{1}{e} \frac{dB}{d\rho_{xy}} \tag{2.11}$$

where ρ_{xy} is the Hall resistivity and B is the magnetic field strength. The right hand side of Equation 2.11 can be extracted from a linear fit to ρ_{xy} plotted versus B in the linear regime. This can be done for each back gate voltage to obtain $n(V_{bg})$.

Once back gate voltage is converted to charge carrier density (using either Equation 2.10 or 2.11), Equation 2.9 could now be used to extract μ from the experimental data. However, since it is a two-point measurement, a series resistance ρ_S which is composed of the contact and cryostat line resistances, needs to be included in Equation 2.9 which then leads to the following equation:

$$\sigma(n) = \left(\frac{1}{\mu n e} + \rho_S\right)^{-1} \tag{2.12}$$

Note that what is measured in experiment is the conductance g which needs to be converted to conductivity in order to be able to apply Equation 2.12. For this conversion the following relation can be used: $\sigma = g\frac{L}{W}$ with L being the length and W the width of the device. By fitting Equation 2.12 to the experimental data, it is possible to extract μ and ρ_S, see Fig. 2.12 (a).

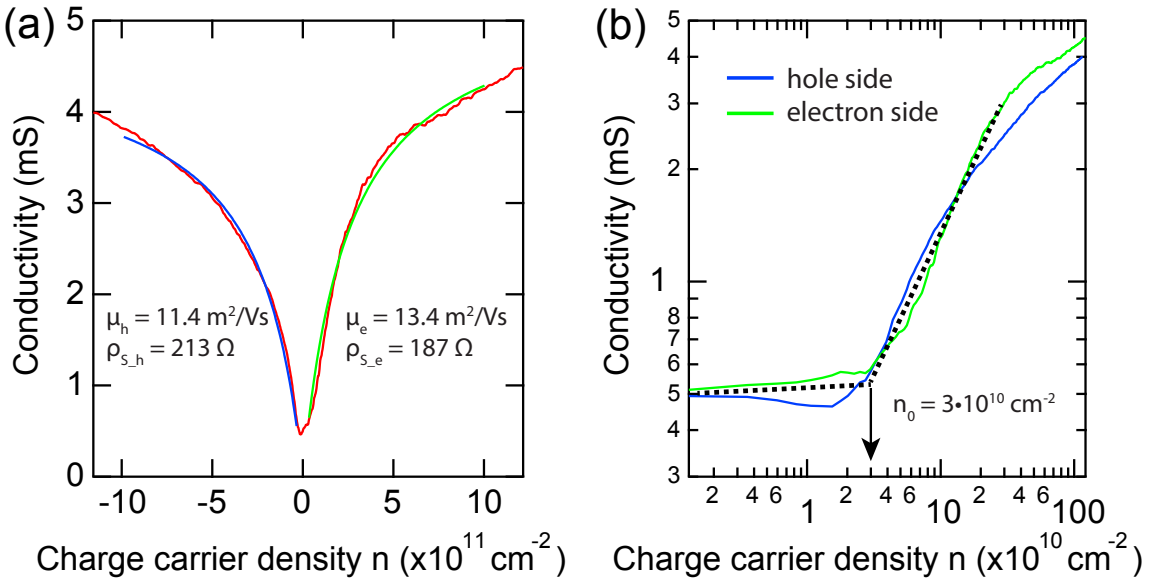

Figure 2.12: Mobility, contact resistance and residual disorder density. (a) Conductivity as a function of charge carrier density. The red curve is the experimental data, the blue and green curves are fits to Equation 2.12. The fitting parameters for the hole and electron side are marked to the left and to the right of the conductivity curve, respectively. **(b)** Conductivity as a function of charge carrier density plotted in a log-log representation. The dashed black lines are guides for the eye and the arrow indicates the location of the kink of the conductivity curve. The location of this kink on the charge carrier density axis marks the residual disorder density n_0, which in this case is $\sim 3{\cdot}10^{10}\,\mathrm{cm}^{-2}$.

In real devices, there is typically a residual disorder density n_0 which is due to charge puddles caused by impurities. This residual disorder density can be extracted directly from the experimental data by plotting conductivity versus charge carrier density in a log-log representation and determining the position of the kink, after which a decrease in density has no influence on the conductivity anymore; see Fig. 2.12 (b).

An alternative possibility to extract the mobility from experimental data is to evaluate the device behavior under magnetic field. In particular, the onset of conductance quantization at a certain B-field yields an estimation of the mobility. Theoretically, this onset can be observed if $\tau > 1/\omega_C$, with the cyclotron frequency $\omega_C = eB/m$. Using Equation 2.8 and 2.9 one ends up with $\mu = 1/B$. This access to the mobility is particularly useful if the device dimensions are not known, as they are required to make use of the above described extraction of the mobility at zero magnetic field.

So far, we assumed to be in the diffusive transport regime. Once the mean free path is equal or larger than the device dimensions, one enters the ballistic transport regime. In this regime, the conductance is limited by the width of the sample which determines how many quantum modes fit through the channel. According to the Landauer theory, the conductance is then given by [94]:

$$G = \frac{4e^2}{h} \sum_{m=0}^{\infty} \Theta \left(\frac{W k_F}{\pi} - m \right) \tag{2.13}$$

where Θ is the step function. Note that one mode gives a conduction of $4\,e^2/h$ due to valley and spin degeneracy. However, as mentioned in section 2.1.2 the conduction through a graphene constriction is strongly dependent on the nature of the edges. In particular, ribbons with AC edges have their valley degeneracy lifted and exhibit steps of $2\,e^2/h$, while ZZ ribbons maintain both degeneracies and show steps of $4\,e^2/h$.

Graphene pn-junctions

Most transport experiments presented in section 4 include the formation of pn-junctions and rely on the basic physics arising in such systems. Therefore, fundamental concepts associated to pn-interfaces in graphene devices are introduced in the following. As previously mentioned, graphene is a zero-bandgap semiconductor. Consequently there are states at all energies, and hence, charges can travel across boarders between regions of different doping (i.e. n and p). However, the transmission of the charge carriers depends on the incident angle relative to the pn-interface. For an incident angle of $\theta = 0$ the so-called Klein tunneling effect appears [26], meaning that the transmission for charge carriers hitting the interface perpendicularly equals 1. For incident angles $\theta \neq 0$, on the other hand, the transmission has values in between zero and one and Snell's law for graphene applies [119]:

$$E_n \cdot sin(\theta_n) = E_p \cdot sin(\theta_p) \tag{2.14}$$

where E_n and E_p denote the Fermi energies in the negatively and positively doped regions, and θ_n and θ_p denote the angles of the incident (n-doped region) and transmitted (p-doped region) states, respectively. Since the refractive index n is given by $n = E_n/E_p = sin(\theta_p)/sin(\theta_n)$, it has a negative sign[1], which is very much different from the situation known from classical optics.

Generally speaking, a pn-interface is a semi-transparent mirror for charge carriers. Hence it is possible to realize Fabry-Pérot-resonator-type of experiments in a graphene junction. A possible device geometry is schematically shown in Fig. 2.13 (a). With a global bottom gate and a local top gate it is possible to create two pn-interfaces which form a cavity for the charge carriers. Whenever the path difference of two different trajectories (see Ψ_1 and Ψ_2 in panel (a)) is a integer multiple of the Fermi wavelength of the charge carries (λ_F), constructive interference appears. This relation translates into the following equation: $2L = j\lambda_F$, with L being the cavity length. By using $\lambda = 2\pi/\sqrt{\pi n}$ we get $L\sqrt{n_j} = j\sqrt{\pi}$ for the j-th Fabry-Pérot oscillation appearing at density n_j. Hence, the difference between two consecutive peaks reads:

$$L = \frac{\sqrt{\pi}}{\sqrt{n_{j+1}} - \sqrt{n_j}} \tag{2.15}$$

This relation can be used to extract L, which is a lower bound for the mean-free-path, and thus provides a method to characterize the device regarding its cleanliness (see panel (b)). This method was used in the work presented in section 4. Fig. 2.13 (c) shows a map of the conductance as a function of n_{in} and n_{out}. Four quadrants are observable which are separated by the charge neutrality points of the inner and outer regions, respectively. In the two quadrants where the system is in a bi-polar regime (i.e. pnp or npn) clear fringes due to Fabry-Pérot resonances are observed. In the uni-polar regimes (i.e. nn'n or pp'p) no pn-interfaces are formed and hence no cavity for the charge carriers is present.

[1]The energies E_n and E_p are measured from the charge neutrality point, i.e. $E_n > 0$ and $E_p < 0$.

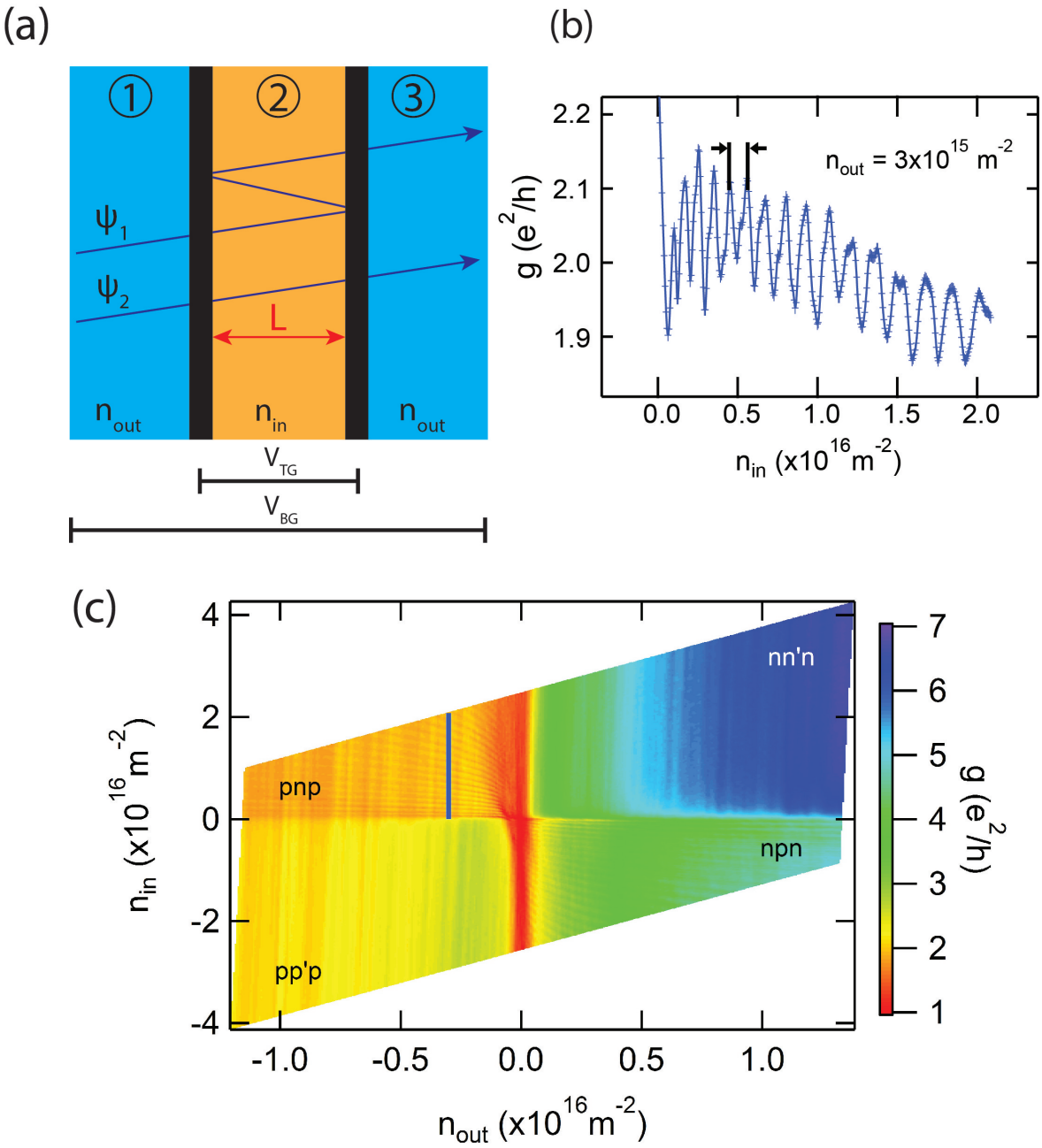

Figure 2.13: PN-junctions and Fabry-Pérot oscillations in graphene. **(a)** Schematic illustration of a graphene device with two pn-junctions (black vertical lines) which separate the device into three regions as indicated at the top. Ψ_1 and Ψ_2 are two wave functions taking two different trajectories, where Ψ_2 traverses the middle region 2 straight and Ψ_1 is reflected back and forth inside region 2. L denotes the distance between the two pn-interfaces and n_{in} and n_{out} the inner density (region 2) and the outer density (region 1 and 3), respectively. The black horizontal lines at the bottom indicate the region of influence of the global back gate and the local top gate. **(b)** Cut along the blue solid line in (c). Clear Fabry-Pérot oscillations are visible. The black vertical lines and arrows mark the density difference between two consecutive peaks, which can be used to extract the cavity length L, as described in the main text. **(c)** Conductance as a function of the inner and outer densities. Four quadrants are observable which correspond to different doping combinations of the inner and outer regions, as labeled inside the graph.

So far no external magnetic field was applied. In the following, effects which appear at finite magnetic field, when the system enters the quantum Hall regime, will be discussed. As mentioned previously, charge carriers in graphene possess spin and valley degeneracy. Not only the spin degree of freedom can be used for information processing, but also the valley degree of freedom was proposed as a potential resource for applications [120]. The valley degree of freedom can be described by a two-component spinor wave function:

$$|\nu\rangle = \begin{pmatrix} \cos(\theta/2) \\ \exp(i\alpha)\sin(\theta/2) \end{pmatrix} \tag{2.16}$$

where α denotes the angle in the equatorial plane and θ the angle with respect to the vertical axis connecting the north and south pols on the Bloch sphere which correspond here to the K and K' point, respectively; see Fig. 2.14 (a).

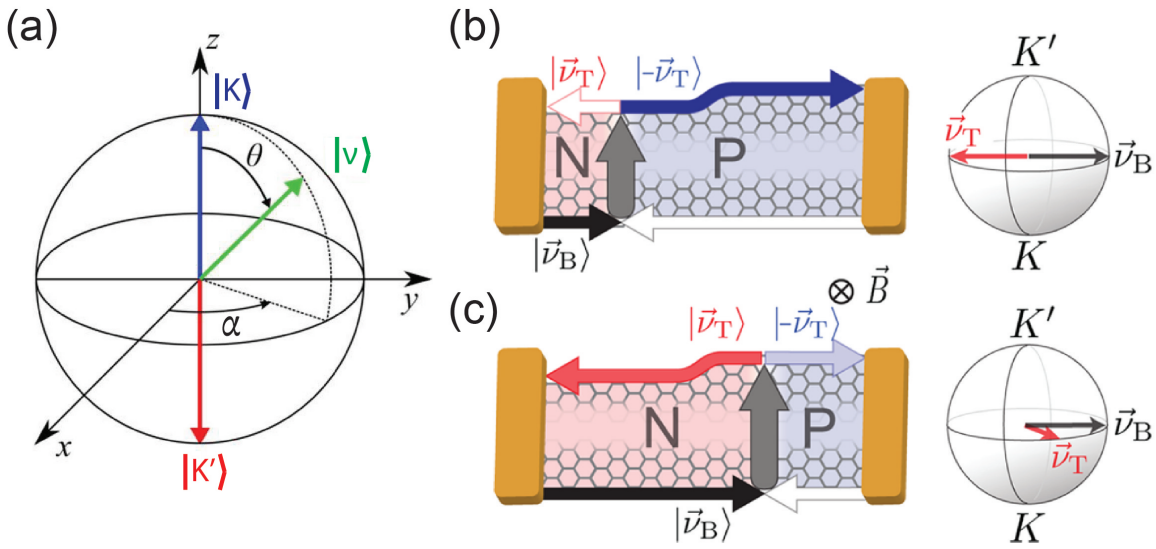

Figure 2.14: Valley-Isospin in a Bloch sphere representation. **(a)** Illustration of a Bloch sphere with the K and K' points indicated at the north and south pole, respectively. An arbitrary state $|\nu\rangle$ can be described with the two angles α and θ. **(b)** and **(c)** Two-terminal GNR devices with a pn-interface. The valley-isospin states at the bottom $|\vec{\nu_B}\rangle$ and top edges $|\vec{\nu_T}\rangle$ are indicated and drawn on the Bloch spheres to right of the ribbon models. Depending on the relative orientation of $|\vec{\nu_B}\rangle$ and $|\vec{\nu_T}\rangle$, the charge carriers are either guided to the left or to the right at the top edge, as indicated with the blue and red arrows. Panel (a) is taken from [121] and panel (b) and (c) from [122].

In the quantum Hall regime, when only the lowest Landau level (LLL) is occupied, the sub-lattice degree of freedom (A and B atoms) is linked to the valley degree of freedom (K and K') [123]. This has the consequence, that for ZZ GNRs, which have only one type of sub-lattice atoms at their edges, the valley-isospin is fully polarized to either the K or K'-point inside the LLL edge state. For AC GNRs, on the other hand, the edges consist in equal amount of sub-lattice atoms A and B. Hence, the valley-isospin lies in the equatorial plane on the Bloch sphere (see Fig. 2.14), which means that it is a superposition of K and K'-states. Tworzydlo et al. [124] proposed to build a valley-filter on the basics of the above mentioned valley-isospin physics in GNRs. In particular, a two-terminal GNR with a vertical pn-interface, connecting the two ribbon edges, is suggested; see Fig. 2.14 (b) and (c). At high magnetic field, the charge carriers move along the edges and the pn-interface [125, 126]. The conductance through the GNR is dependent on the relative orientation of the valley-isospins at the two edges, i.e. for an AC ribbon, on the angle α in between them. It is noteworthy that the valley-isospin needs to be conserved when traveling along the pn-interface from one edge to the other, i.e. clean samples without intervalley scattering are required. The conductance as a function of α for an AC GNR is then given by:

$$G = \frac{e^2}{h}\,(1 - cos(\alpha)) \tag{2.17}$$

A similar formula can be derived for the ZZ case [124]. The parameter α is related to the ribbon width, as explained below for the AC and ZZ cases; see Equation 2.18 and 2.19. In the proposed experiment [124] ribbons with step edges are considered and the pn-interface position can be changed by electrostatic gating of the n and p doped regions, respectively. Shifting the pn-interface across a step edge, which effectively changes the ribbon width and thus α, is expected to change the conduction according to Equation 2.17. Fig. 2.14 (b) illustrates the case where the valley-isospin at the bottom edge ($|\vec{\nu_B}\rangle$) and at the top edge ($|\vec{\nu_T}\rangle$) have a relative angle of $\alpha = \pi$, which leads to full transmittance of the LLL state across the pn-interface at the top edge and to the

right contact. If the pn-interface is moved to the right across a step, see panel (c), the ribbon width changes and thus the relative angle between $|\vec{\nu_B}\rangle$ and $|\vec{\nu_T}\rangle$ changes as well, here becoming smaller. Hence, the LLL state is partially transmitted and partially reflected which leads to an intermediate conductance through the device, according to Equation 2.17. To summarize, in AC GNRs, the following conductance values are expected depending on the ribbon width, given in the number of unit cells N between the bottom and top edge:

$$G_{AC} = \begin{cases} 2\,e^2/h & \text{N mod } 3 = 2 \quad (\alpha = \pi) \\ 0.5\,e^2/h & \text{N otherwise} \quad (\alpha = \pm\pi/3) \end{cases} \tag{2.18}$$

For the ZZ case a similar derivation leads to the following conductance values:

$$G_{ZZ} = \begin{cases} 2\,e^2/h & \text{N odd} \quad (\alpha = 0) \\ 0\,e^2/h & \text{N even} \quad (\alpha = \pi) \end{cases} \tag{2.19}$$

With the above described physics and the device proposal of Tworzydlo [124], it is thus possible to scan the pn-interface along the edge and thereby gain information on the edge configuration and roughness, by analyzing the conductance through the device. This method was used in this thesis to acquire insight into the edge quality of H plasma defined GNRs, see section 4.

2.1.6 Sample Fabrication

This section describes the fabrication techniques which were used to produce the graphene samples investigated in this thesis. In particular, the transfer technique of graphene onto a hBN substrate [127] and a technique used for full encapsulation of graphene into hBN flakes, will be described.

For the fabrication of SL graphene on hBN samples, one starts with two Si/SiO_2 wafer pieces. On one of them, hBN is exfoliated directly via the scotch tape method [21].

On the second wafer piece, a polymer stack consisting of a water-soluble layer (either polyvinyl alcohol (PVA) or dextrane) and a PMMA layer, are spin coated consecutively. Afterwards, graphene is exfoliated on top of the polymer stack with the scotch tape technique. This second wafer is put into de-ionized (DI) water, where the water soluble layer is dissolved and the PMMA layer with the graphene flakes on top floats on the water surface (see Fig. 2.15 (a) and (b)). In a next step, the PMMA layer is fished with a glass plate which has a hole in the middle. In doing so, the graphene flake should be inside the hole of the glass plate, see panel (c). Afterwards, the graphene flake can be aligned to the hBN flake from the first chip and transferred on top via a mask aligner setup, see panel (d).

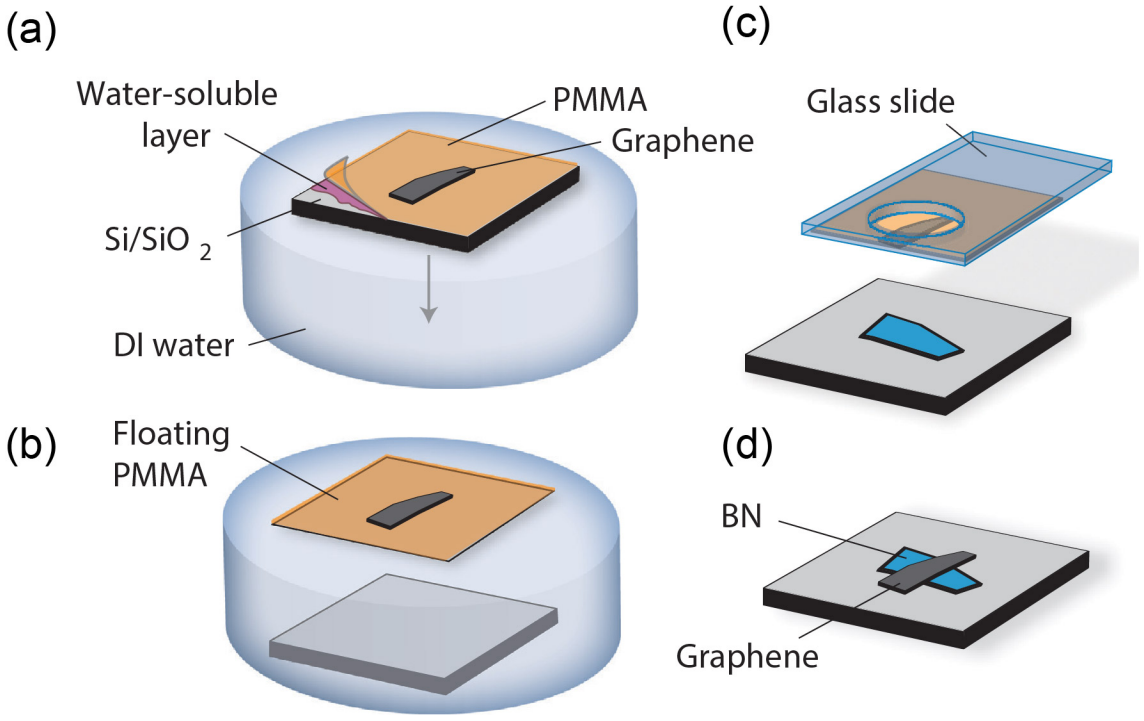

Figure 2.15: Transfer process of graphene onto a hBN flake. **(a)** The chip with the polymer stack and the graphene on top is put into a petri dish filled with DI water and the water-soluble layer is dissolved. **(b)** The PMMA layer with graphene on top floats on the water surface and the chip sinks to the ground. **(c)** A glass slide with a hole in the middle is used to fish the PMMA layer with graphene on top. **(d)** A mask aligner setup is used to align the graphene and hBN flakes and bring them together. Fig. taken from [127].

Subsequently, a PMMA etch mask is fabricated and round shaped defects are introduced into the SL graphene flake by means of RIE in an Ar/O_2 plasma. After lift-off

the sample is etched in the H plasma setup to create hexagonal shaped etch pits which can be studied with AFM and Raman spectroscopy to get inside into their edge quality, as done and presented in section 4.

A second type of devices to study the electronic transport properties in H plasma defined GNRs, is fabricated as follows. First, a SL graphene flake is transferred onto a hBN flake as described above. In a second step, the graphene flake is structured in such a way that it forms GNRs after H plasma etching, i.e. round defects are introduced in close proximity (see Fig. 2.16 (a)) or strips following the ZZ direction of the graphene lattice are defined by means of RIE in an Ar/O_2 plasma (see panel (c)). Upon H plasma exposure, the roundish defects transform into hexagons which define a GNR (type 1) in between them which has H plasma defined edges (see panel (b)).

A strip following the ZZ direction is etched from the edges to form a H plasma defined GNR (type 2), as shown in panel (d). Note that type 1 GNRs have self aligned edges, while type 2 GNRs rely on an initial alignment to the ZZ direction of the graphene lattice which is as good as possible. H plasma defined graphene edges were seen to follow the ZZ direction and are presumably of high quality [62, 63]. However, how good the quality of the edges really is, is subject of ongoing research. The results presented in section 4 shed light on this open question.

Once the desired GNR structures are etched into the graphene flake, it is encapsulated by transferring a second hBN flake on top. This is done to preserve the cleanliness of the devices while electrical contacts are fabricated. Encapsulated samples also show a higher stability in device performance compared to open devices where residues can be introduced directly onto the graphene surface.

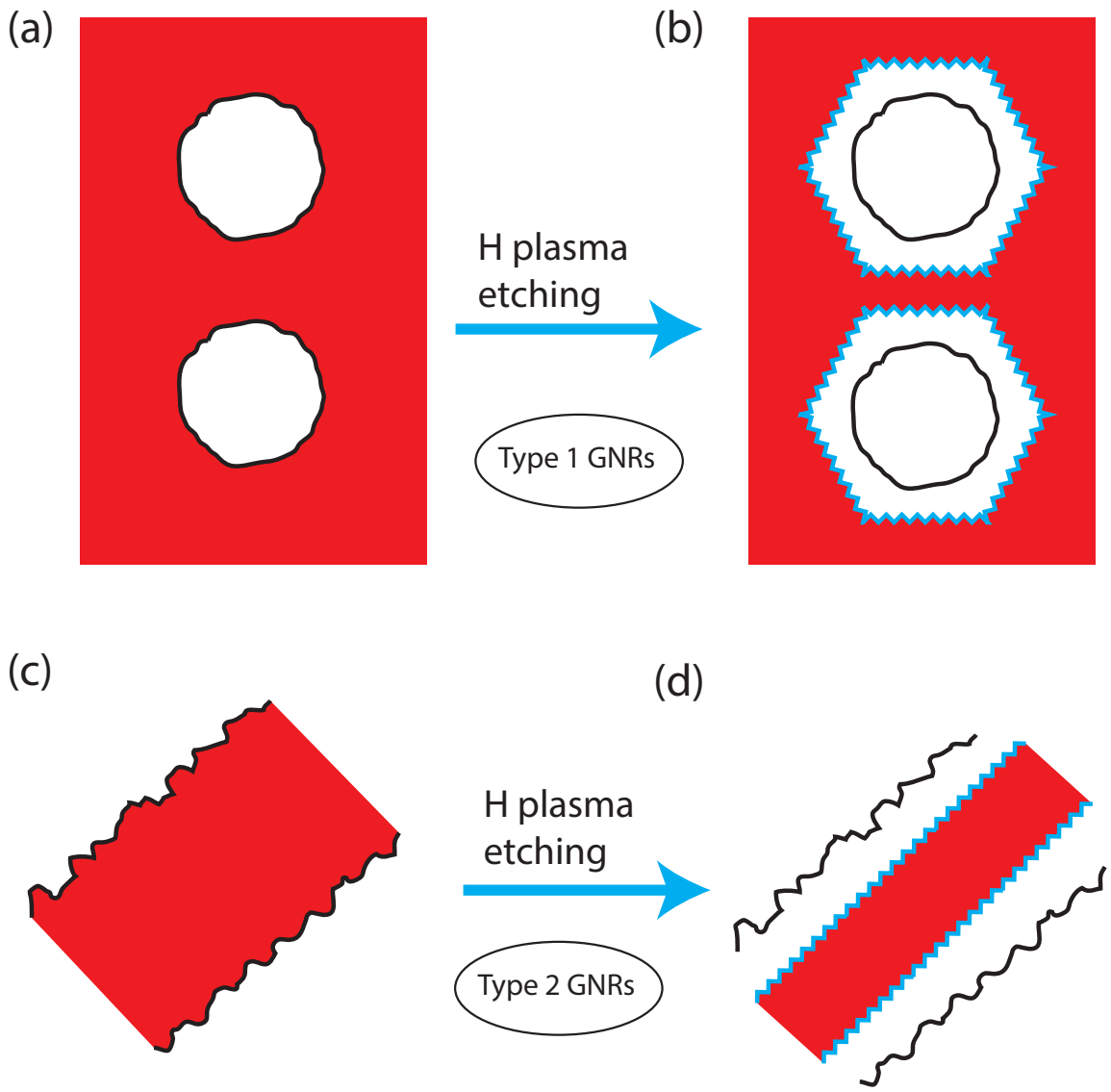

Figure 2.16: Formation of H plasma defined GNRs. **(a)** Schematic of RIE defined roundish defects etched into the graphene layer, which is demarcated in red. **(b)** H plasma anisotropic etching transforms the artificial defects into hexagons terminated with ZZ edges and thus forms a GNR with ZZ edges in between the hexagons. **(c)** RIE defined GNR running along the ZZ direction but with rough edges. **(d)** H plasma exposure etches the GNR only from the edges and heals out defects to form a ZZ terminated GNR.

The encapsulation process is shown in Fig. 2.17 and described in the following. In a first step, a Si/SiO_2 wafer is covered with a layer of poly-propylene carbonate (PPC) with a thickness of $\sim 1\mu$m. A scotch tape with a window is placed on top and hBN is exfoliated onto the PPC layer (see panel (a) and (b)). Thereafter, a suitable hBN flake is chosen by means of optical microscopy (OM). From the color of the flakes one

can estimate the flake thicknesses and in dark field OM mode it is possible to see if the flake has any cracks or larger impurities on its surface. Afterwards, the PPC layer is carefully peeled off the substrate by removing the scotch tape, and placed on a polydimethylsiloxane (PDMS) cube which lies on a glass slide; see panel (c). The chosen hBN flake is then aligned to the graphene flake which has a GNR structure inscribed and was fabricated as described in Fig. 2.15 and 2.16. With a mask aligner setup the top hBN flake (t-hBN) is brought into contact with the structured graphene layer which lies on the bottom hBN flake (b-hBN); see panel (d). Due to adhesive Van-der-Waals forces, which are strong between 2D-materials, the flakes stick together and build a complete stack as shown in panel (e).

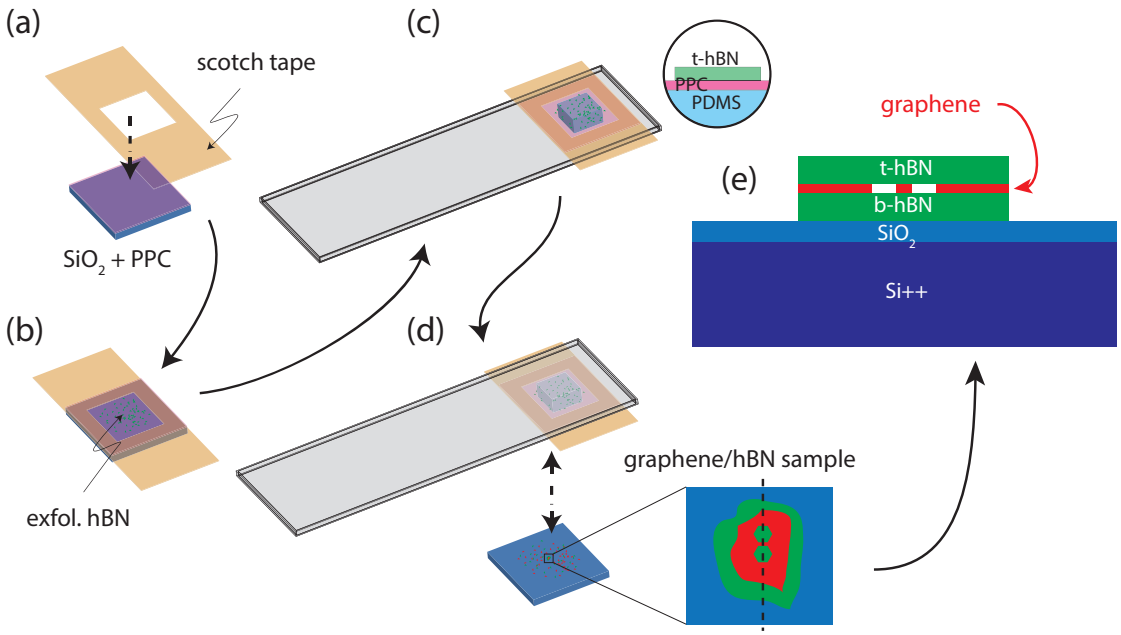

Figure 2.17: Schematic illustration of the encapsulation technique. **(a)** Scotch tape with a window is pressed on SiO_2/PPC chip. **(b)** hBN is exfoliated on the PPC layer. **(c)** The PPC layer is removed by carefully peeling off the scotch tape and subsequently placed on a glass plate with a PDMS cube on top to form a stamp. **(d)** A suitable hBN flake is chosen and aligned to the graphene/hBN sample with the GNR structure. With a mask aligner setup the layers are brought into contact. **(e)** Cross section of the complete stack along the black dashed line in (d) after lift-off of the PPC layer. Fig. adapted from [128].

When 2D-materials are assembled as described above, a common phenomenon is the formation of bubbles, which are presumably dirt residues and/or air trapped in between the layers. These can introduce scattering and lower the electronic quality of devices. To get rid of these bubbles, an annealing of the entire stack can help. The annealing does not eliminate the trapped dirt particles, but it makes them aggregating in smaller spaces, which in turn leads to larger clean spaces.

After the stack is assembled, electrical contacts need to be fabricated in order to investigate electronic transport through the GNRs. Since the graphene layer is encapsulated inside the hBN flakes and therefore not accessible for top-contacts, a special technique needs to be applied, which is the fabrication of so-called 1D-side-contacts [129]. After etching through the stack with an $SF_6/Ar/O_2$-plasma the graphene edges are accessible. Subsequent evaporation of Cr/Au-contacts creates relatively low-resistive ohmics, generally in the range of a few hundreds of $\Omega\mu m$. Details on the fabrication processes described in this section are given in the Appendix A.

2.2 Ge/Si Core/Shell Nanowires

2.2.1 Special Characteristics of Ge/Si Core/Shell Nanowires

In this section, Ge/Si nanowires (NWs) are introduced and their special characteristics are described. The wires investigated in this thesis were grown by our collaborators A. Li and E. Bakkers at the Technical University Eindhoven. The growth process basically comprises three steps, see illustration in Fig. 2.18 (a). First, Au colloids are distributed on a [111] Ge substrate and act as nucleation centers for the NW growth. In a vapor-liquid-solid growth process, with germane gas introduced into the growth chamber, mono-crystalline Ge wires with lengths between 1 - 10 μm grow perpendicularly to the substrate wafer surface. During this process, important parameters such as pressure and temperature are tuned in order to have growth only vertically and no growth in radial direction is happening. In the second step, the process gas is changed to silane gas and a Si separation segment is grown which prevents the diffusion of Au from the nucleation center into the Ge NW. In the last step, the growth parameters are changed such that side-wall growth of Si occurs and a Si shell of variable thickness can be produced.

It is important to note that, despite the [111] Ge substrate, three different growth directions are obtained: [110], [111], and [112]. It was found [130] that NWs in [110] growth direction have the lowest amount of defects and exhibit the highest electronic mobility compared to the other two crystal directions. In Fig. 2.18 (b) a TEM image of a longitudinal cross section of a Ge/Si core/shell NW is depicted and shows the high epitaxial quality of the material layers. Due to the valence band offset of Ge and Si of 0.5 eV, the Fermi level lies inside the Si band gap but below the valance band edge of the Ge core, thus allowing for holes to accumulate and generate a 1D-hole gas, see Fig. 2.18 (c). It is notable that no dopants are necessary to form this hole gas which is advantageous because dopants introduce potential scattering centers and can lower the electronic mobility of devices.

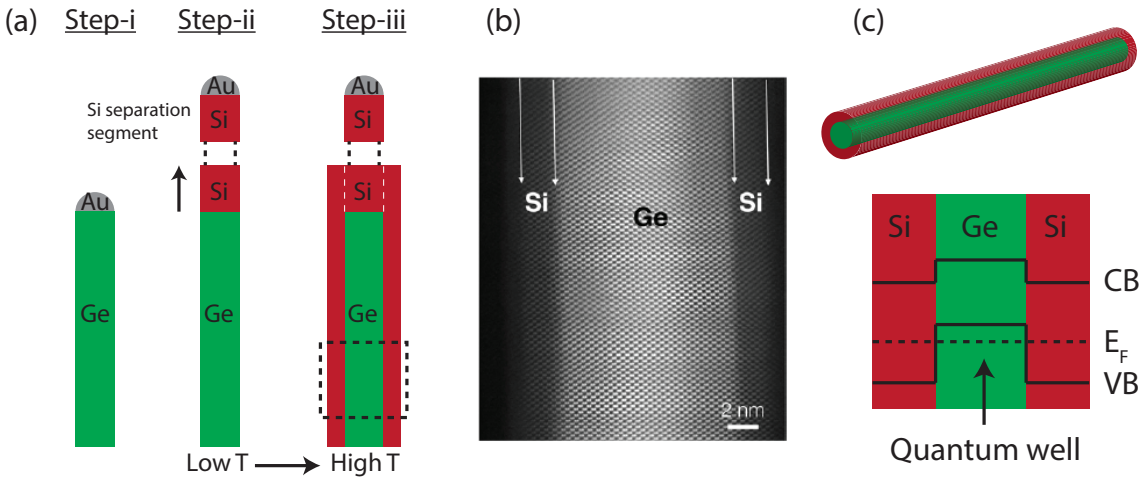

Figure 2.18: Growth process and band structure of a Ge/Si core/shell NW. **(a)** Illustration of the 3-step growth process of Ge/Si core/shell NWs. (i) Growth of the Ge core. (ii) Formation of Si-separation layer at low temperature. (iii) Growth of Si shell at high temperature. Fig. adapted from [130]. **(b)** Transmission electron microscopy (TEM) image of a region as marked by the dashed rectangle in panel (a). The highly uniform and defect-free shell structure is visible. Fig. taken from [130]. **(c)** Illustration of the wire architecture and the electronic band structure. The Fermi level (E_F) lies within the valence band (VB) inside the Ge core but lies in the band gap of the Si shell, thus forming a highly confined 1D-hole gas. Fig. adapted from [131].

This high-mobility hole gas has interesting electronic properties arising from the strong transverse confinement and fundamental properties of the charge carriers. In particular, a strong and tunable spin-orbit interaction (SOI) of Rashba-type is theoretically predicted [13]. Direct dipolar coupling to a moderate electric field ($\approx$ V/μm) leads to the so-called direct Rashba SOI (DRSOI) which is on the order of meV and hence 10 - 100 times larger compared to the conventional Rashba SOI. This large SOI enables the creation of helical modes with large spin-orbit energies where holes of opposite spin move in opposite directions, hence enabling electrical spin control. In Fig. 2.19 (a) the dispersion relation for holes in a Ge NW is shown for different electric field strengths applied across the wire. As can be seen in the Fig., the DRSOI has qualitatively a similar effect on the band structure as the conventional Rashba SOI, i.e. horizontal shifting of the two parabolas for the different spin species. When combined with a superconductor, Ge/Si NWs provide a useful platform for Majorana fermions [13].

In addition to the DRSOI, an electric field tunable g*-factor[2] is predicted to arise in this system [14], and was experimentally observed by Brauns and co-workers [15]. In Fig. 2.19 (b) g* is plotted against the magnetic field angle Θ for different orientations of the electric field ($\mathbf{E} \parallel \hat{x}$ and $\mathbf{E} \parallel \hat{y}$) and different field strengths. It can be seen that the magnitude of the g*-factor depends on both, the orientation of the electric field and the orientation of the magnetic field relative to the NW. Furthermore, the g*-factor can be tuned by the applied electric field strength, generally being lower at higher fields.

Both, the strong SOI and a tunable g*-factor are essential ingredients for the realization of quantum computation schemes with spin-qubits [6]. Namely, a strong and tunable SOI facilitates fast and all-electrical spin manipulation and a locally tunable g*-factor allows to selectively couple individual spin-qubits to microwave cavities [132]. A notable advantage of group IV materials, such as Ge and Si, is their relatively low nuclear spin content. Hence, decoherence due to hyperfine interaction is anticipated to be small which is advantageous for spin-qubit applications where long coherence times are desired. Ge and Si could in principle be isotopically purified to lower the amount of naturally abundant nuclear spins even further. Moreover, there is no contact hyperfine interaction due to the p-type character of holes, which is again beneficial for the coherence of the system.

[2]Since the spin states are mixtures of heavy hole and light hole states, the spin quantum number $m_s \neq 0$. This is accounted for in the effective g-factor g*.

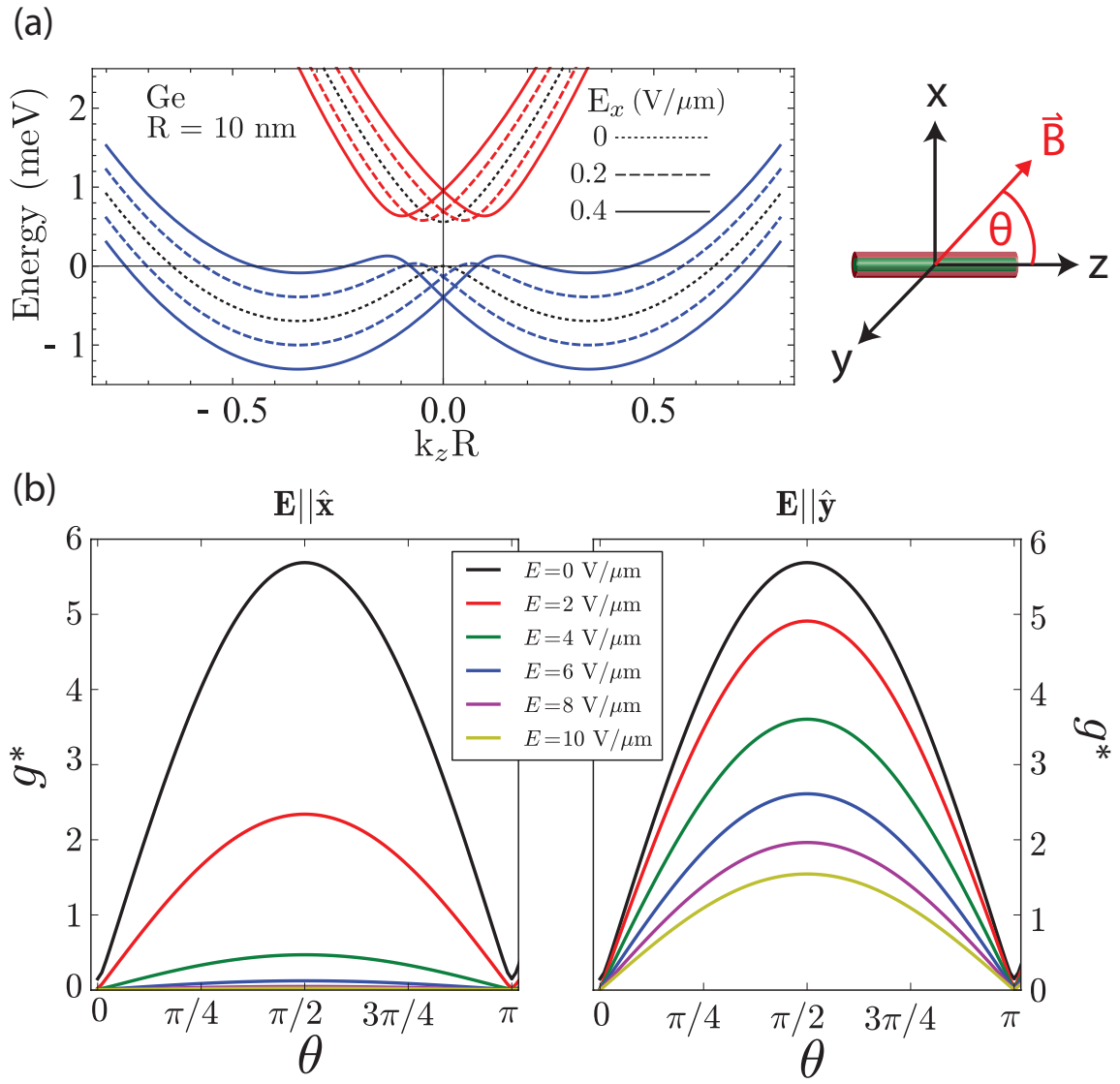

Figure 2.19: Tunable SOI and g*-factor anisotropy. **(a)** Effect of an external electric field (E_x) on the electronic band structure of a Ge wire with radius $R = 10\,\text{nm}$. The direct Rashba SOI shifts the spin-degenerate bands on the k-axis and in principle allows to tune the system into a helical regime where opposite spins travel in opposite directions. Fig. adapted from [13]. **(b)** Electric-field dependent g*-factor anisotropy. Left panel: effective g-factor as a function of the angle (Θ) of the magnetic field $\vec{B}$ with respect to the z-axis/wire-axis for an externally applied electric field **E** along the x-axis. Right panel: Similar plot as in the left panel, but with **E** aligned along the y-axis. The color coding represents different electric field strengths as labeled in between the panels. Fig. taken from [14].

2.2.2 State of the Art

In this section a brief review of important experiments performed with Ge/Si core/shell NWs is given. The list is chronologically ordered and not meant to be exhaustive.

In 2002, growth of the first Ge/Si core/shell NWs by means of a chemical vapor deposition method was reported [133].

In 2005, Lu and co-workers [131] have shown the accumulation of a 1D-hole gas without the use of dopants in Ge/Si NWs. Moreover, they have fabricated transparent contacts and observed ballistic transport at liquid He and room temperature, manifested in conductance quantization.

In 2006, results on the fabrication and characterization of NW field effect transistors (NW-FETs) based on Ge/Si core/shell NWs were published. The device characteristics were shown to out-perform standard Si MOSFET devices by far [134].

In 2007, the formation of a double QD with a charge sensor in form of an adjacent wire was reported [135].

In 2008, Roddaro et al. [136] have observed sequential spin-filling in single quantum dots (QDs) in a Ge/Si NW. Furthermore, they extracted g-factor values and tentatively identified a hole exchange interaction strength.

In 2010, magneto-conductance measurements were presented which revealed an electric-field tunable SOI. In addition, phase coherence times and SOI strengths were extracted from fitting of weak-antilocalization peaks [137].

In 2012, measurements of relaxation times and the integration of a charge sensor via a floating gate was reported [138].

In 2014, Higginbotham and co-workers [139] have measured relaxation and decoherence times in a Ge/Si double QD. In the same year, they published a work on Coulomb blockade antilocalization from which they extracted a SOI length [140].

In 2016, Brauns et al. published three papers on the investigation of Ge/Si NWs. In a first work, highly tunable hole QDs were presented [141]. In the second work [15], an electric field dependent g-factor anisotropy was observed, which is in good agreement with theoretical predictions from [14]. Furthermore, they observed shell-filling and anisotropic PSB in a double QD [142].

In 2017, a thorough study on the correlation of electronic mobility, crystal direction, wire diameter and coherent strain was published [130]. In the same year, the electrical modulation of weak-antilocalization and SOI in dual gated Ge/Si NWs was reported [143]. Furthermore, Zarassi et al. investigated the magnetic field evolution of PSB and extracted an upper bound for the SOI length [144].

In 2018, Watzinger and co-workers reported results on the investigation of Ge hut wires. These hut wires have a triangular cross-section and exhibit a strain pattern which leads to a large heavy hole - light hole splitting and thus to a low mixing of the respective states. This leads to an Ising-type hyperfine interaction which is favorable for long coherence times [145].

2.2.3 Single Quantum Dots

A QD is a small solid-state object in which charge carriers (i.e. electrons or holes) are confined in all three dimensions of space. Thus, QDs resemble atoms and are also called *artificial atoms*. The charging energy $E_C = e^2/C$, where e is the elementary charge and C is the capacitance of the QD, needs to be provided to load one additional charge carrier onto the QD. In order to observe charging effects, E_C needs to be much larger than the thermal energy k_BT and the energy associated to the tunnel coupling $h\Gamma$, hence $E_C \gg k_BT, h\Gamma$.

In addition to the classical charging energy, the spatial confinement of charge carriers leads to quantized energy levels in the QD, which is a purely quantum mechanical effect. The energy difference between two consecutive orbital states E_{orb} gives rise to a shell-filling effect. Due to the Pauli exclusion principle [146] at most two fermions

(e.g. holes or electrons) with opposite spin can occupy the same orbital. Hence the addition energy E_{add}, which needs to be paid to add an additional charge carrier to the QD, equals the charging energy for additions of charge carriers into the same orbital and $E_{add} = E_C + E_{orb}$ if a new orbital is getting populated. In order to observe effects associated to E_{orb}, again temperature and tunnel-coupling need to be smaller than E_{orb}: $E_{orb} \gg k_B T, h\Gamma$.

In Fig. 2.20 (a) a schematic diagram of the chemical potentials and the relevant quantities in a QD is shown. At zero source-drain bias, i.e. $V_{SD} = \mu_S - \mu_D \approx 0$, current can only flow through the QD if the chemical potential of a certain QD-level μ_{dot} is aligned with the chemical potentials of source μ_S and drain μ_D, hence $\mu_S = \mu_{dot} = \mu_D$; otherwise current flow is suppressed and the system is in *Coulomb blockade*. The chemical potentials of the QD levels can be tuned via the electric field effect by applying a voltage V_g to a nearby gate which is capacitively coupled to the QD. A typical measurement of the differential conductance dI/dV through a QD versus gate voltage is shown in Fig. 2.20 (b) where regularly spaced Coulomb peaks are observed. The separation of two consecutive Coulomb peaks in gate voltage can be translated to energy via the lever-arm α and corresponds to $E_{add} = \alpha \Delta V_g$.

If a finite source-drain bias is applied, i.e. $V_{SD} = \mu_S - \mu_D > 0$, a transport window exists which allows a current to flow only when at least one QD-level lies inside this window ($\mu_S > \mu_{dot} > \mu_D$). A typical measurement of the differential conductance $\mathrm{d}I/\mathrm{d}V_{SD}$ versus V_{SD} and V_g is schematically drawn in Fig. 2.20 (c). The gray areas form the so-called *Coulomb diamonds* where the system is in Coulomb blockade and no current flows through the QD. The contours of these areas correspond to configurations where a certain QD-level is aligned with either μ_S or μ_D. The height of the Coulomb diamonds corresponds to E_{add} and the width is related to E_{add}, again via the lever arm as $\alpha \Delta V_g = E_{add}$. If $V_{SD} \geq E_{orb}$ transport trough excited states is enabled, see the blue and purple dashed lines in panel (a) and (c).

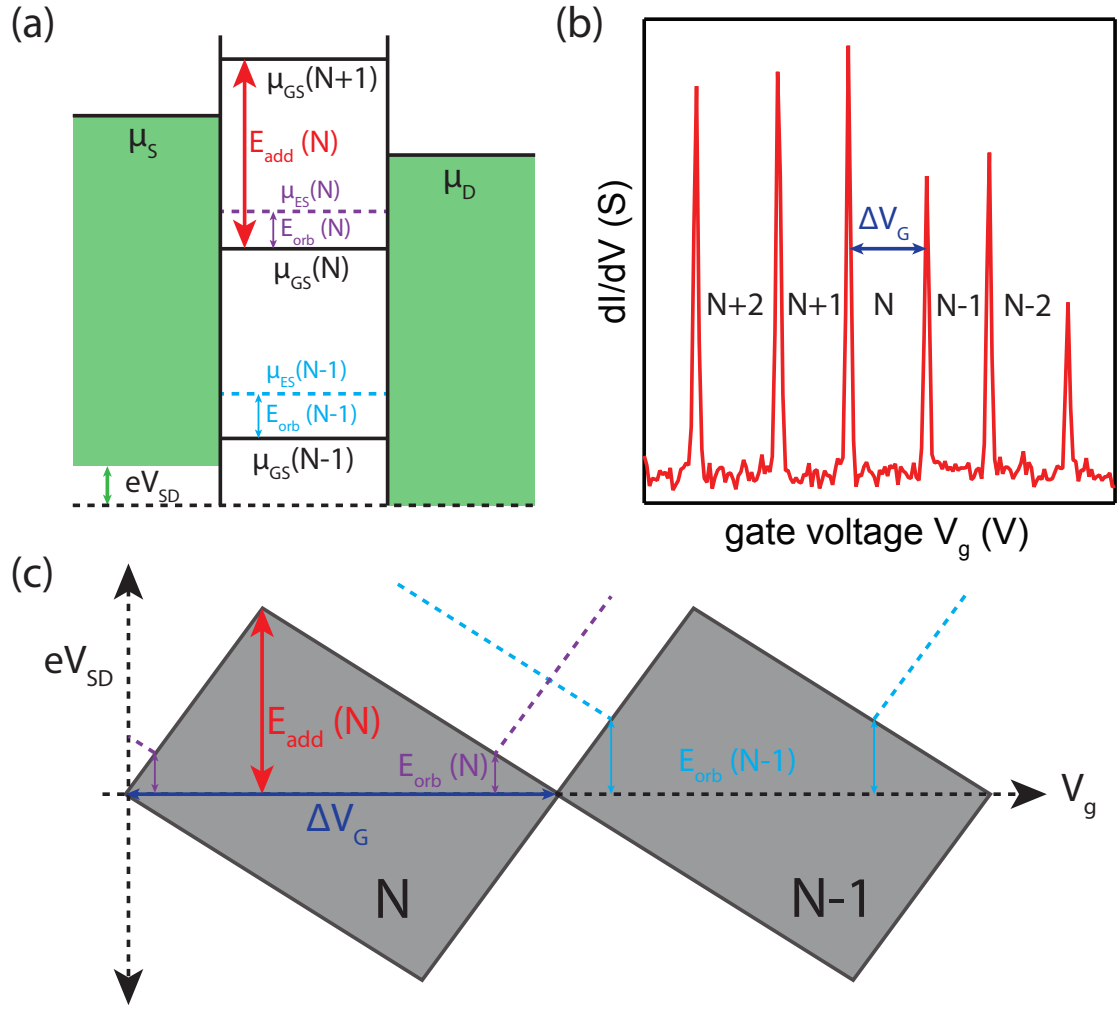

Figure 2.20: Single quantum dot level and stability diagrams. **(a)** QD level diagram with the chemical potential of the source (μ_S) and the drain (μ_D) indicated. The black horizontal lines depict ground states (GS) whereas the blue and purple dashed lines illustrate excited states (ES). Consecutive ground states are separated by the addition energy (E_{add}) and the energy separation of an excited state to its ground state is the orbital energy (E_{orb}). Fig. adapted from [147]. **(b)** Differential conductance dI/dV as a function of gate voltage at zero source-drain bias (i.e. $V_{SD} = 0$). Clear Coulomb peaks are visible which are separated by regions of zero conductance corresponding to Coulomb blockade. The relative occupation numbers are inscribed. **(c)** Schematic illustration of the QD stability diagram at finite source-drain bias (i.e. $V_{SD} \neq 0$). The gray areas correspond to combinations of bias and gate voltage values which prohibit conduction through the quantum dot which is due to Coulomb blockade. The contours of these Coulomb blockade areas correspond to conditions where a QD level is in resonance with either the source or drain chemical potential and current can flow through the QD. The blue and purple dashed lines correspond to excited states as marked in panel (a). From the height and width of a diamond the addition energy and the lever arm can be extracted. Fig. adapted from [147].

2.2.4 Double Quantum Dots

Double QDs are systems where two single QDs are tunnel coupled and capacitively coupled to each other. The corresponding electric circuit diagram of a serial double QD is shown in Fig. 2.21. In addition to the coupling between the dots, a coupling to the source (S) and drain (D) reservoirs as well as a purely capacitive coupling to two nearby gates is given. By applying voltages to these gates it is possible to tune the electrochemical potentials of the individual QDs (μ_1 and μ_2) and therefore to modulate the respective occupation numbers (N_1 and N_2).

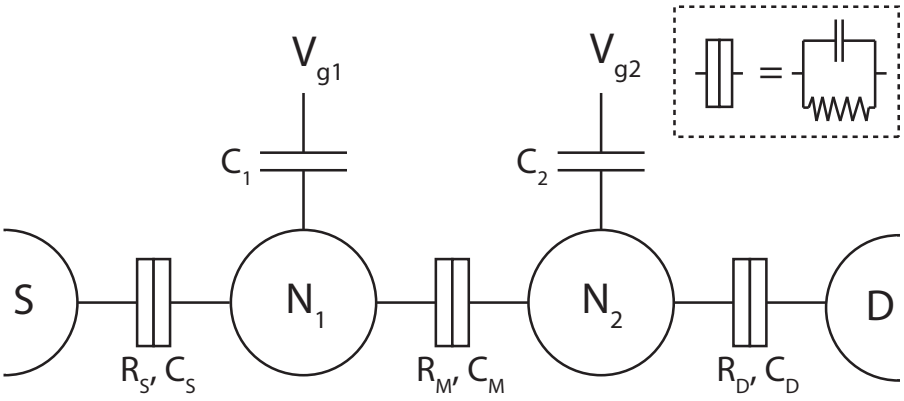

Figure 2.21: Double quantum dot circuit. Two QDs with occupation numbers N_1 and N_2 are tunnel coupled (R_M) and capacitively coupled (C_M) to each other and to the source (S) and drain (D) reservoirs. In addition the two QDs are capacitively coupled ($C_{1,2}$) to nearby gates which allow to individually tune the electrochemical potentials of the QDs. Fig. adapted from [148].

By measuring the conductance through the double QD as a function of the gate voltages V_{g1} and V_{g2}, a so-called charge stability diagram (CSD) can be recorded. The appearance of such a CSD depends on the mutual capacitive coupling C_M between the two QDs and on the applied source-drain bias. In Fig. 2.22, three CSDs are shown, each for a different regime of C_M and all for zero source-drain bias. If $C_M \approx 0$, conduction through the double QD is only possible if all four chemical potentials (μ_S, μ_1, μ_2 and μ_D) are aligned. This results in the situation depicted in panel (a), hence only at the black points conduction can be observed. However, if only one dot level is resonant

with a reservoir potential, the occupation number of the respective dot can be changed without current flow through the whole double QD (black dashed lines in panel (a)).

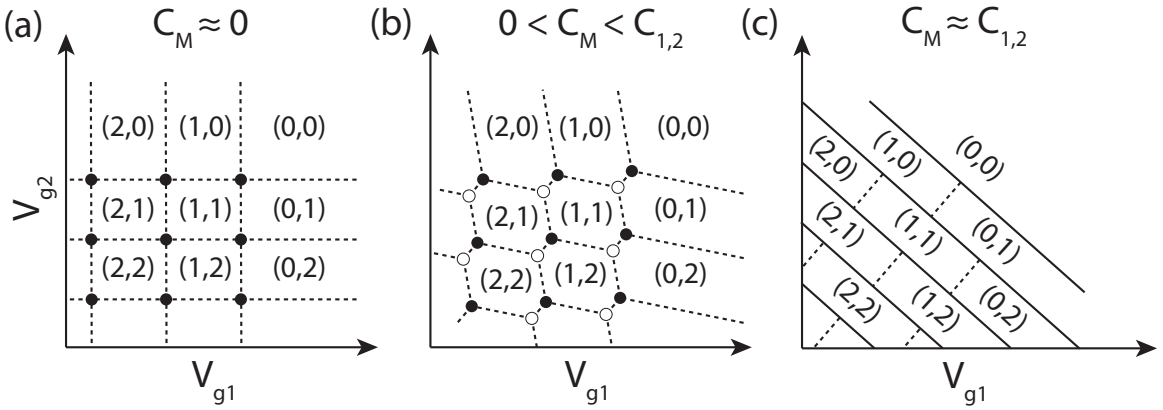

Figure 2.22: Double quantum dot stability diagrams. **(a)** Charge stability diagram for $C_M \approx 0$. Conduction is only possible at the black dots, where all chemical potentials, μ_S, μ_D , μ_1, μ_2, are aligned. The dashed lines correspond to situations where only one dot level is aligned with a reservoir potential. The occupation numbers of the double QD are indicated inside regions of constant charge states. **(b)** Charge stability diagram for $0 < C_M < C_{1,2}$. The points of finite conductance split up into triple-points where three charge states are degenerate. **(c)** Charge stability diagram for $C_M \approx C_{1,2}$. The double QD effectively behaves as a large single QD with occupation $N_1 + N_2$. Conduction is possible along the solid diagonal lines. Fig. adapted from [148].

For intermediate values of C_M, i.e. $0 < C_M < C_{1,2}$, the points where conduction through the double QD is possible split up into triple-points, see panel (b). Here, three charge states are degenerate. Again the dashed lines correspond to situations where only one of the two dots is in resonance with a reservoir potential. The rectangular pattern for $C_M \approx 0$ is thus transformed into a hexagonal pattern when a finite interdot coupling C_M is switched on.

The third regime, where $C_M \approx C_{1,2}$, resembles a large single QD with an occupation of $N_1 + N_2$. The corresponding charge stability diagram is shown in panel (c). Transport trough the double QD is possible on the solid black lines which run diagonally through the charge stability diagram.

So far the discussion only considered transport at zero source-drain bias, i.e. $V_{SD} = \mu_S - \mu_D \approx 0$. When a finite source-drain bias is applied, the triple points in Fig. 2.22 (b) evolve into triangular areas where finite conductance is possible, see Fig. 2.23. Transport inside the triangles is governed by inelastic processes [149] and co-tunneling [150]. The blue dashed line indicates an excited state which would appear as a current step inside the bias triangle.

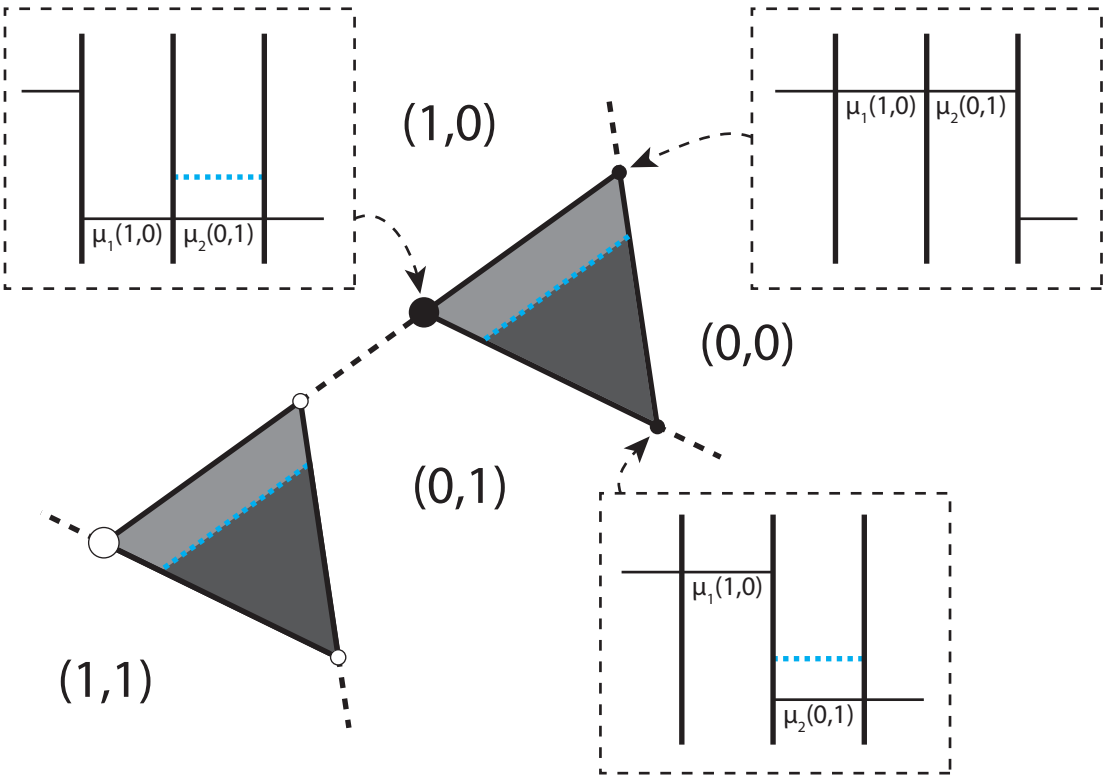

Figure 2.23: Double quantum dot bias triangles. Grey triangular areas mark regions where finite conductance is possible. At the three corners of the upper triangle, the corresponding level diagrams are shown. The blue dashed line depicts an excited state which is apparent inside the bias triangles as a step of increased conductance. Fig. adapted from [148].

2.2.5 Pauli Spin Blockade

Pauli spin blockade (PSB) is a phenomenon which can be observed in double QD systems and is based on the Pauli exclusion principle [146]. The effect was first shown in 2002 by Ono and co-workers [151] and has become a valuable method for spin-

state detection via spin-to-charge conversion. PSB is an effect which leads to selective current rectification, hence transport is possible through the double QD for one sign of applied source-drain bias V_{SD} and blocked for the inverted direction. The basic mechanism is schematically depicted in Fig. 2.24. In the unblocked situation (see panel (a)), $V_{SD} > 0$ and a current flows from left to right. Assuming the left QD is filled with a spin-up hole, the second hole which is filled into this QD can either be a spin-down hole and thus form a singlet state S(2,0)[3], or it can be a spin-up hole and form a triplet state T(2,0)[4]. While the S(2,0) state requires only the charging energy to be paid, the T(2,0) can only be formed if the second hole can access a new orbital and therefore needs the charging energy E_C plus the orbital energy E_{orb} to be energetically accessible. In addition, a finite exchange energy E_{ex} is present, thus the energy difference between the singlet and triplet states reads $\Delta_{ST} = E_{orb}\text{-}E_{ex}$. However, for the positive bias-direction both, the S(2,0) and the T(2,0) state, lie inside the bias window and are thus accessible for transport. If a hole tunnels to the second dot again a singlet S(1,1) or a triplet T(1,1) state can be formed. At zero magnetic field, the S(1,1) and T(1,1) are spaced by an exchange energy J which is arising due to the finite tunnel-coupling t between the dots: $J = 4t^2/E_C$. Because typically, $t \ll E_C$, J is small on the scale of the energy difference between the S(2,0) and T(2,0) states. Since both the S(1,1) and T(1,1) states are above the drain chemical potential, a hole can exit the dot and finish a transport cycle.

If the bias direction is reversed, i.e $V_{SD} < 0$, the situation encountered is depicted in panel (b). Again assuming a permanent spin-up hole in the left dot, a hole entering the right dot can either form a singlet S(1,1) or a triplet T(1,1) state with the first hole. If a S(1,1) state is formed, the hole on the right dot can tunnel to the left dot, thus forming a S(2,0) state and then exit the dot which leads to current flow. If, on the other hand, a spin-up hole enters the right dot and forms a T(1,1) state, it can only tunnel to the T(2,0) state because of spin-conservation. However, the T(2,0) state lies

[3]In terms of the single-particle spins, the singlet state can be defined as $S = 1/\sqrt{2}\,|\uparrow\downarrow - \downarrow\uparrow\rangle$

[4]The three triplet states T_0, T_+ and T_- are degenerate at zero magnetic field and can be written as $T_0 = 1/\sqrt{2}\,|\uparrow\downarrow - \downarrow\uparrow\rangle$, $T_+ = |\uparrow\uparrow\rangle$ and $T_- = |\downarrow\downarrow\rangle$

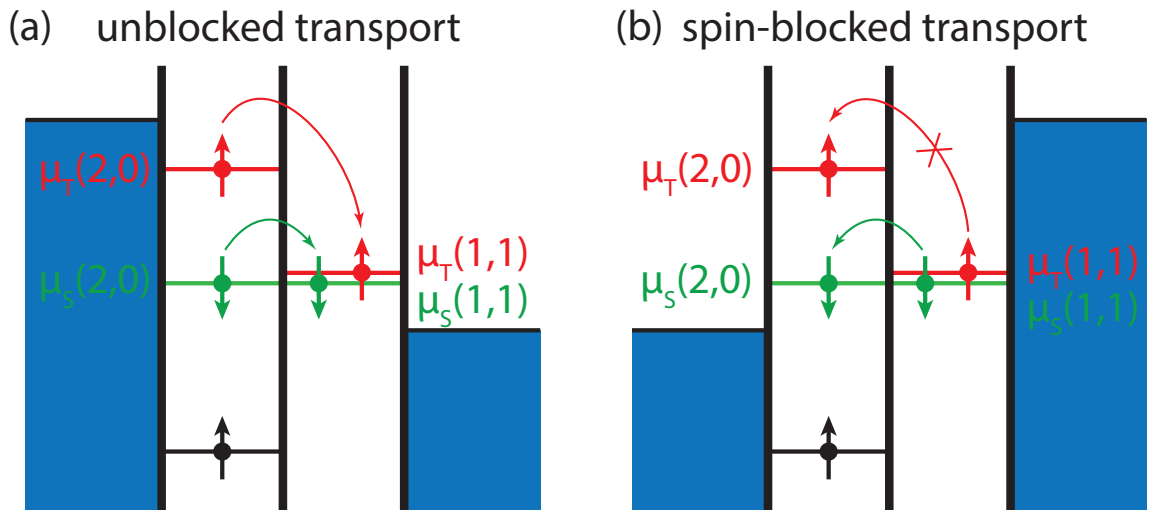

Figure 2.24: Pauli spin blockade. **(a)** Unblocked transport through the double QD for $V_{SD} > 0$. The green spins form singlet states with the initially present black spin while the red spins form triplet states. All states are available for transport. **(b)** Spin-blocked transport for the opposite bias direction $V_{SD} < 0$. Transport is only possible for the singlet states but blocked for the triplet states. Fig. adapted from [152].

higher in energy and is thus not accessible, i.e. as soon as a spin-up hole enters the right dot and a T(1,1) state is formed, the system is trapped in spin-blockade.

The blockade can be lifted if the detuning ϵ, defined as the energy difference between the S(1,1) and S(2,0) states, is larger than $\Delta_{ST} - J$. However, also for zero detuning, processes exist which can change the spin orientation and thus lead to the transition from a T(1,1) to a S(1,1) state which is then able to lead to transport through the dot via the S(2,0) state, hence giving rise to a leakage current I_{leak}. Mainly three mechanisms are important which lead to spin-relaxation and lifting of the spin-blockade:

- **Hyperfine interaction**

  Spin-relaxation can be caused by coupling to nuclear spins which produce randomly fluctuating magnetic fields [153]. These magnetic fields mix spin-up and spin-down states and therefore allow for transitions from T(1,1) to S(1,1). However, in Ge/Si NWs hyperfine interaction is expected to be small because the natural abundance of spin-carrying nuclei is low, i.e. 4.7 at. % of ^{29}Si in natural Si [154] and 7.8 at. % of ^{73}Ge in natural Ge [155]. Furthermore, the contact

hyperfine interaction is expected to be small due to the p-type wave function of holes [156].

- **Spin-flip cotunneling**

  Spin-flip cotunneling describes the process where a trapped spin (from the T(1,1) state) is exchanged with a spin of opposite orientation from the closest lead reservoir, and thus forms a S(1,1) state giving rise to a leakage current [157]. Further insight into the process can be gained by B-field dependent measurements of the leakage current. At finite magnetic field, the triplet states $T_-(1,1)$ and $T_+(1,1)$ are split by the Zeeman energy E_Z from the $T_0(1,1)$ state. Since both, the virtual intermediate state and the state of the hole tunneling into the dot, come from the temperature-broadened Fermi level in the lead reservoir, the process is suppressed if $E_Z > k_BT$, where k_B is the Boltzmann constant and T the temperature [158].

- **Spin-orbit interaction**

  Spin-orbit interaction effectively introduces non-spin conserving tunneling and thereby couples the T(1,1) and S(2,0) states [159]. Insight into the process can be gained by investigation of the magnetic field dependence of the leakage current. The SOI mixes all four (1,1) states and creates four new eigenstates of the system. At zero magnetic field, three out of four eigenstates are blocked and the leakage current is given by the relaxation rate Γ_{rel} of the blocked states to the unblocked state, i.e. $I_{leak} = 4/9 \cdot \Gamma_{rel}$. At high magnetic field, only one out of four eigenstates is blocked which increases the leakage current by a factor of nine, i.e. $I_{leak} = 4\Gamma_{rel}$. Hence, the magnetic field dependence of the leakage current shows a dip around zero field, which can be analyzed and used to gain information on the strength of the SOI [144, 159].

3 Anisotropic Etching of Graphite and Graphene in a Remote Hydrogen Plasma

D. Hug, S. Zihlmann, M. K. Rehmann, Y. B. Kalyoncu, T. N. Camenzind, L. Marot, D. M. Zumbuehl

Department of Physics, University of Basel, CH-4056 Basel, Switzerland

K. Watanabe, T. Taniguchi

National Institute for Material Science, 1-1 Namiki, Tsukuba 305-0044, Japan

This chapter was published in *npj 2D Materials and Applications* **1**, 21 (2017).

Abstract

We investigate the etching of a pure hydrogen plasma on graphite samples and graphene flakes on SiO_2 and hexagonal Boron-Nitride (hBN) substrates. The pressure and distance dependence of the graphite exposure experiments reveals the existence of two distinct plasma regimes: the *direct* and the *remote* plasma regime. Graphite surfaces exposed *directly* to the hydrogen plasma exhibit numerous etch pits of various size and depth, indicating continuous defect creation throughout the etching process. In contrast, anisotropic etching forming regular and symmetric hexagons starting only from preexisting defects and edges is seen in the *remote* plasma regime, where the sample is located downstream, outside of the glowing plasma.

This regime is possible in a narrow window of parameters where essentially all ions have already recombined, yet a flux of H-radicals performing anisotropic etching is still present. At the required process pressures, the radicals can recombine only on surfaces, not in the gas itself. Thus, the tube material needs to exhibit a sufficiently low H radical recombination coefficient, such as found for quartz or pyrex. In the *remote* regime, we investigate the etching of single layer and bilayer graphene on SiO_2 and hBN substrates. We find *isotropic* etching for single layer graphene on SiO_2, whereas we observe highly *anisotropic* etching for graphene on a hBN substrate. For bilayer graphene, anisotropic etching is observed on both substrates. Finally, we demonstrate the use of artificial defects to create well defined graphene nanostructures with clean crystallographic edges.

3.1 Introduction

Graphene nanoribbons (GNRs) have emerged as a promising platform for graphene nano devices, including a range of intriguing quantum phenomena beyond opening of a confinement induced band gap [10, 12, 30, 95, 160]. In armchair GNRs, giant Rashba spin-orbit coupling can be induced with nanomagnets, leading to helical modes and spin filtering [11]. Further, Majorana fermions localized at the ends of the ribbon were predicted in proximity of an s-wave superconductor [11]. Zigzag ribbons, on the other hand, were proposed as a promising system for spin filters [160]. Theory showed that electronic states in zigzag ribbons are strongly confined to the edge [10, 95, 160], recently observed in experiments [79, 81, 82, 161]. Further, edge magnetism was predicted to emerge at low temperatures [10, 29, 30, 59, 95], with opposite GNR edges magnetized in opposite directions. High quality, crystallographic edges are very important here, since edge disorder suppresses magnetic correlations [29] and tends to cause electron localization, inhibiting transport studies. GNRs fabricated with standard electron beam lithography (EBL) and Ar/O_2 etching typically exhibit pronounced disorder [86, 87, 89, 162–165], complicating transport studies.

Fabrication methods creating ribbons with clean crystallographic edges were recently developed, including carbon nanotube unzipping [36, 37], ultrasonication of intercalated graphite [38], chemical bottom up approaches [39, 40], anisotropic etching by nickel nanoparticles [46], or during CVD processing [47–49], or carbothermal etching of graphene sheets [51–54]. Here, we use a hydrogen (H) plasma etching technique [60, 62–65] because it allows precise, top-down and on-demand positioning and tailoring of graphene nanostructures. Such nanostructures can easily be designed to spread out into larger graphene areas incorporated into the same graphene sheet, thus providing for a relatively easy way to make electrical contacts.

3.2 Main Experimental Findings

In this work, we investigate the anisotropic H plasma etching of graphite surfaces in dependence of the gas pressure and the sample - plasma distance (see Methods). We find that the etching characteristics can be divided into a direct and a remote plasma regime. In the *direct* plasma regime, the sample is placed within the glowing plasma, and surfaces show many hexagons of various sizes indicating a continuous defect induction throughout the etching process. In the *remote* plasma regime, on the other hand, the sample is placed downstream of the glowing plasma, and etching occurs only from preexisting defects which makes the fabrication of well defined graphene nanostructures possible. Further, we have prepared single layer (SL) and bilayer (BL) graphene flakes on SiO_2 and hexagonal boron nitride (hBN) substrates and exposed them to the remote H plasma. We observe a strong dependence of the anisotropy of the etch on the substrate material. SL graphene on SiO_2 is etched isotropically, confirming previous findings [63, 66], whereas we observe highly anisotropic etching of SL graphene on hBN [65], producing very regular and symmetric hexagonal etch pits. Anisotropic etching of SL graphene on hBN offers the possibility to fabricate diverse graphene nanostructure with well defined edges (e.g. GNRs) and allows investigation of their intrinsic electronic transport properties.

3.3 Results and Discussion

3.3.1 Distance Dependance

We first investigated graphite flakes, allowing for rather simple and fast processing. The graphite specimen [166] were cleaned by peeling with scotch tape and subsequently exposed for one hour to a pure H plasma at a temperature $T = 400\,^{\circ}\mathrm{C}$ and a distance d from the end of the surfatron. We first present the distance dependence of the H plasma process. Figure 3.1a shows AFM topography scans for exposures of one hour at four different distances at constant pressure $p = 1\,\mathrm{mbar}$. At the larger distances,

etch pits of monolayer step height are created upon plasma exposure, exhibiting a regular hexagonal shape and demonstrating a strongly anisotropic process [60, 62]. All observed hexagons exhibit the same orientation. From previous studies, it is known that hexagons created by exposure to a remote H plasma exhibit edges pointing along the zigzag direction [60, 62]. As the sample is brought closer to the plasma, significantly more etch pits appear, often located at the border of existing holes, sharing one common hexagon side (see Figure 3.1a, $d = 42\,\mathrm{cm}$). For the closest position $d = 37\,\mathrm{cm}$ – unlike the larger distances – the sample is located within the visible plasma glow region, resulting in a strong and several layers deep scarring of the entire surface.

To quantitatively study the distance dependence, we evaluated larger images to gather better statistics and plot histograms showing the number of holes as a function of diameter, see Figure 3.1b-d. The overall number of holes obviously increases strongly with decreasing sample-surfatron distance d. For small distances, a wide distribution of diameters is seen, ranging from several 100 nm down to nearly vanishing hexagon size, suggesting that new defects serving as etch seeds are created throughout the exposure time. The width of the hole diameter distribution is given by the anisotropic etch rate and the exposure duration in this regime. For larger d, on the other hand, the few holes seen have comparable diameters, consistent with etching proceeding predominantly from preexisting graphite defects, without adding new defects. This results in a narrow width of the distribution of hole sizes. As previously reported [60, 62, 63], exposure to energetic ions seems to create defects, while exposure to hydrogen radicals appears to result in anisotropic etching and growth of hexagons centered around preexisting defects and borders.

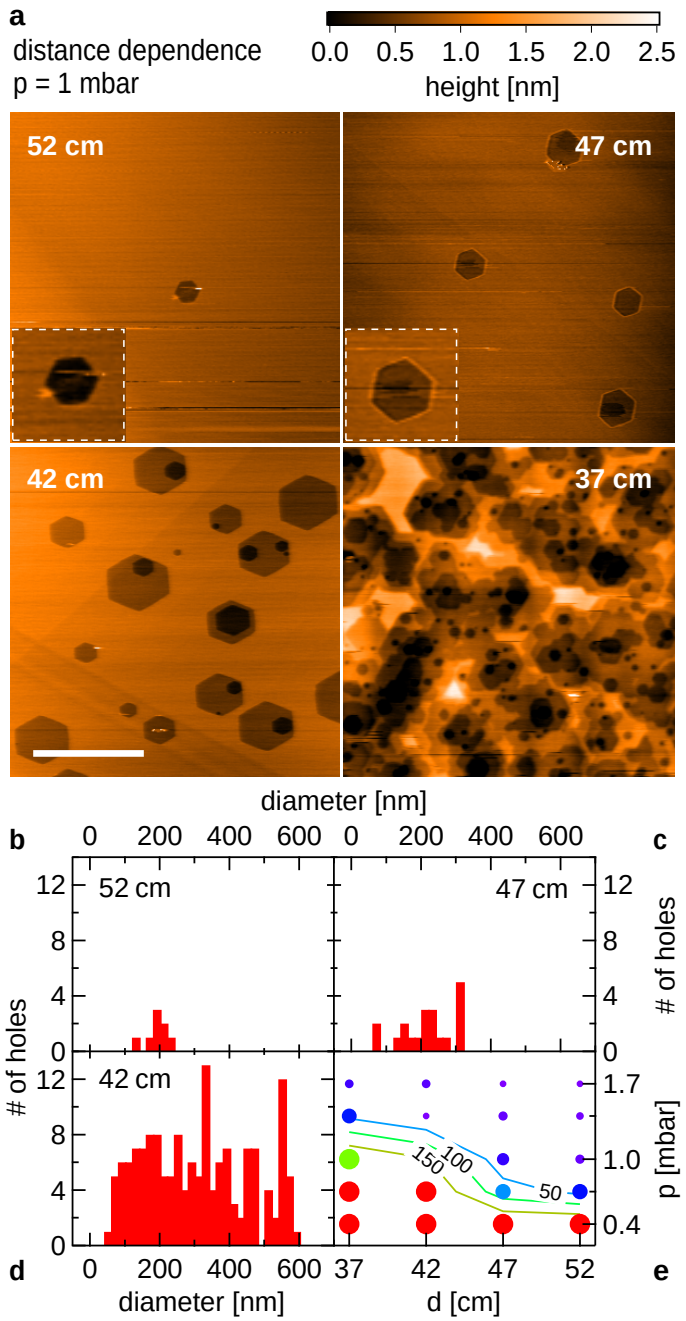

Figure 3.1: Distance dependence of graphite exposures (a) AFM images (tapping mode) of graphite surfaces for various distances d, as labeled, all exposed to the plasma for 1 h at $p = 1$ mbar and $T = 400°C$, all shown on the same color scale. Main panels are $3 \times 3\,\mu m^2$, scale bar is $1\,\mu m$, insets (dashed white boxes) are $0.25 \times 0.25\,\mu m^2$. Slight hexagon distortion at 42 cm is an imaging artefact due to drift. See SOM for the complete distance and pressure matrix. (b-d) Histograms obtained from $10 \times 10\,\mu m^2$ scans, showing the number of holes against hole diameter (bin size 20 nm). (e) The size of the circle markers corresponds to the width of the diameter distribution. The color indicates the number of holes, with red corresponding to large number of holes. For samples located within the glowing plasma (red circles), a lower bound of 300 holes and a minimum width of distribution of diameter of 600 nm is shown.

3.3.2 Pressure Dependance

Next, we turn to the pressure dependence. In Figure 3.2a, AFM topography images are shown at four different pressures p at constant distance $d = 52\,\mathrm{cm}$. The number of holes increases with decreasing pressure, similar to decreasing distance, giving rise to etch pits of monolayer step height at intermediate pressures. At the highest pressures, however, no etch pits were observed, in strong contrast to the lowest pressure, where ubiquitous and deep etching is seen, demonstrating the strong influence of p. Analyzing the etch pits using histograms confirms that p and d have a similar influence on the etching process (compare Figure 3.2b, c with Figure 3.1b-d). Figure 3.1e summarizes the histograms of all investigated graphite samples (see supplementary online material (SOM)), using color to represent the number of holes, while the size of each marker is proportional to the width of the distribution of hole diameters. A clear correlation between the number of holes and the width of the distribution is seen: the largest circles are red, while the small circles are purple.

The analysis of the graphite exposure data leads to two qualitatively different types of processes: the *direct* and the *remote* plasma regime. In the *direct* plasma regime (large, red circles, Figure 3.1e), the sample is located directly within the plasma discharge region, hence exposing it to large densities of radicals and ions, capable of inducing defects throughout the exposure, giving a broad hole diameter distribution. In the *remote* plasma regime (small, purple circles, Figure 3.1e), on the other hand, the sample is positioned outside, downstream of the plasma generation region, where ions have recombined and only a residual flux of radicals is present. There, etching proceeds predominantly from preexisting defects and edges, leaving the basal planes mostly untouched. In this regime, a narrow distribution of hole diameters results, centered around the diameter given by the anisotropic etch rate and the exposure time. See SOM for more details.

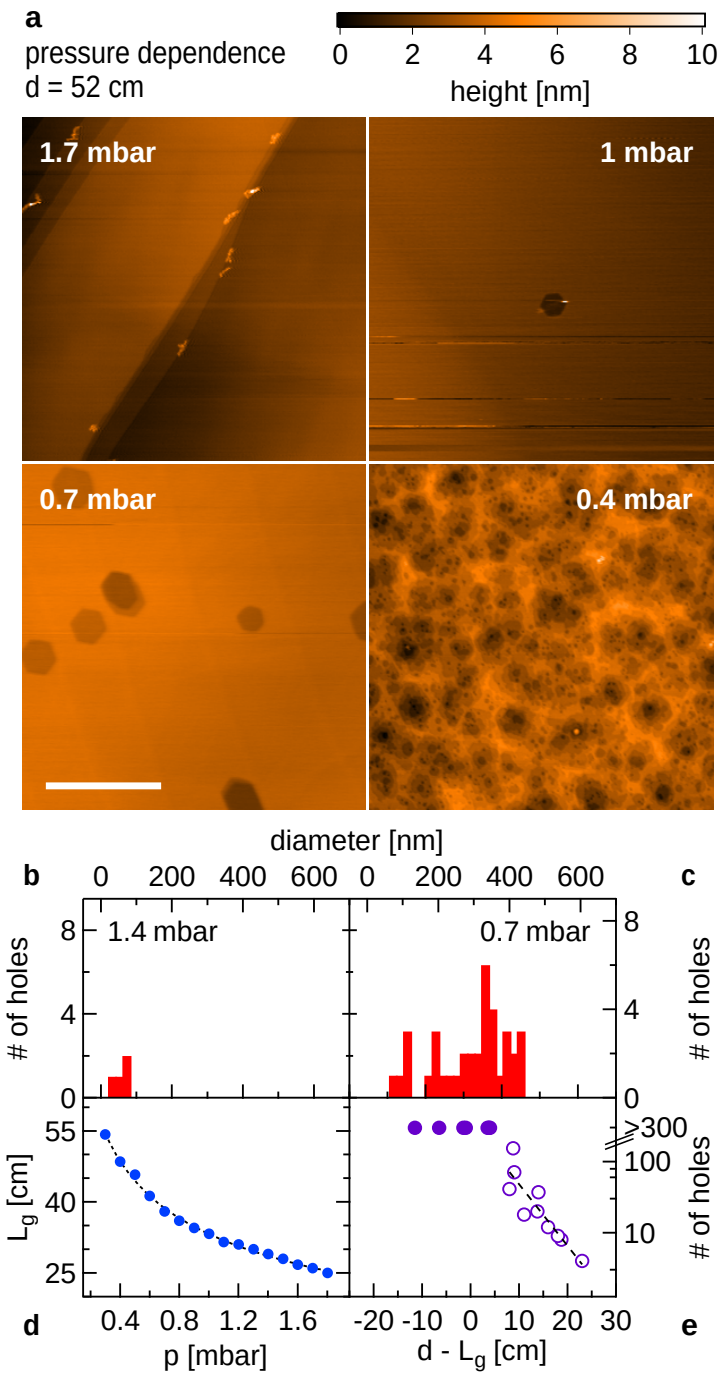

Figure 3.2: Pressure dependence of graphite exposures (a) AFM images (tapping mode) of graphite surfaces for various p, as indicated, exposed for one hour at $d = 52\,\mathrm{cm}$ and $T = 400°\mathrm{C}$, all shown on the same color scale. All panels are $3 \times 3\,\mu\mathrm{m}^2$, scale bar is $1\,\mu\mathrm{m}$. (b,c) Histograms from $10 \times 10\,\mu\mathrm{m}^2$ scans, displaying the number of holes against hole diameter (bin size 20 nm) for p as labeled. (d) Length L_g of the optically visible plasma as a function of p. The dashed curve is a $1/\sqrt{p}$ fit. (e) Number of holes versus distance from plasma edge $d - L_g$. A lower bound of 300 holes is given for the heavily etched cases where an exact hole-count was not feasible. The dashed black line is an exponential fit to the data with < 300 holes with 1/e decay length ~ 5 cm.

Further, there is an intimate connection between distance and pressure: lower pressure results in a longer gas mean free path and therefore a larger average distance for recombination in the diffusive gas. This results in a larger length of the plasma column $L_g(p)$, measured from the edge of the visibly glowing plasma to the surfatron, see Figure 3.2d. Thus, changing the pressure with fixed sample position modifies the distance between sample and plasma edge. Hence, it is useful to introduce an effective distance $d' = d - L_g(p)$, the distance from the sample to the edge of the glowing plasma. Thus, $d' \lesssim 0$ roughly marks the direct plasma regime while $d' \gg 0$ signifies the remote plasma regime. Reactive particles are generated inside the plasma column and start recombining once they have left the plasma generation region.

The reaction kinetics in low temperature H plasmas are highly non-trivial despite the relatively simple chemical composition [167]. Nevertheless, it is well known that at the pressures used here ($p \sim 1\,\mathrm{mbar}$), the predominant radical decay mechanism is surface mediated association rather than gas collisions. Two colliding H atoms require a third body to carry away the excess energy for association to occur [168]. However, under the present conditions, three body collisions are very unlikely, thus leaving only the surface assisted process (which also leads to surface heating [96]). Recombination of ions, in contrast, can also occur through an additional collisional channel, in absence of a surface. Which species – ions or radicals – decay on a shorter length scale downstream of the plasma edge thus depends on both the surface properties and gas parameters. For anisotropic etching without defect creation, a flux of H radicals in absence of ions is needed, as previously reported [60, 62, 63], thus requiring the ion density to decay on a shorter length than the radicals.

The surface attenuation of H radicals thus plays an important role, and was previously studied [96, 97]. Some glasses such as pyrex or quartz – as used in our experiments – were identified as materials with a low recombination coefficient, particularly compared to some common metallic surfaces such as stainless steel and aluminum. This weak surface attenuation can open a downstream window offering a flux of H radicals while

essentially all ions have already recombined, as desired and achieved here, see e.g. Figure 3.1b, 3.2b and 3 (below). Nevertheless, the etch rate in the downstream window was observed to decrease slowly over long periods of time, reaching a vanishingly small etch rate after more than 100 hours of plasma exposure. The elevated temperatures in the furnace may enhance impurity migration towards the surfaces of the tube, possibly amplifying the surface attenuation of H radicals. Larger anisotropic etch rates were observed when utilizing higher purity quartz tubes manufactured from synthetic fused silica [169], supporting the assumption of the role of impurities. High impurity content and even small amounts of metallic deposition on the tube wall give wave damping due to dielectric losses and result in an enhanced decay of radicals.

To study the decay of reactive species, we note that the ion flux is proportional to the number of holes created. We find a roughly exponential decrease of the number of holes with distance, see Figure 3.2e and SOM, with a 1/e decay length of about 5 cm. The anisotropic etch rate, on the other hand, is related to the flux of H radicals. We extract the anisotropic etch rate, defined as the growth per unit time of the radius of a circle inscribed to the hexagonal etch pit, averaged over a number of holes, shown in Figure 3.4a. Only the largest set of hexagons of each exposed graphite sample were evaluated to obtain the etch rate, since smaller holes might not have etched from the beginning of the exposure. As expected, the anisotropic etch rate is largest for small distances, falling off quickly with increasing separation from the plasma edge. There is also an apparent pressure dependence, with larger pressures tending to give lower etch rates, see Figure 3.4a. Given only two or three points along the d-axis for each pressure, and only few holes for some parameter sets (d, p), a reliable H-radical decay length cannot be extracted from these data. A theoretical estimate gives an H-radical decay length of $\sim 12\,\mathrm{cm}$, see SOM, in agreement with observations in Figure 3.4a, and longer than the ion decay length of 5 cm, as observed. The etch rates we extract are a few nm per min at 400 °C, consistent with previous reports [62, 63].

3.3.3 Substrate Dependance

Next, we study the plasma exposure of SL and BL graphene exfoliated onto a SiO_2 substrate using the established tape method [21]. We patterned disks using standard EBL and reactive ion etching with an Ar/O_2 plasma, resulting in circular graphene holes which were subsequently exposed to the remote H plasma in the regime where H radicals but essentially no ions are present, as determined from the graphite experiments. BL graphene grows regular hexagons with parallel sides (see Figure 3.3b), as expected from the graphite results. SL graphene, on the other hand, displayed mostly round holes (see Figure 3.3a), though some weakly developed, irregular hexagonal shapes are also occasionally seen. Further, several additional, not EBL defined holes appear on the SL after exposure, all smaller than the EBL initiated etch pits. After a second plasma exposure, the number of holes on the SL increased further, indicating generation of new defects, while only EBL defined holes appear on the BL. Note that the SL and BL regions shown in Figure 3.3a and b are located on the same graphene flake, ensuring identical plasma conditions.

In addition, the average hole diameter on SL is visibly larger than on the BL (Figure 3.3a and b) after the same exposure time, indicating a faster etch rate on SL. Thus, SL on SiO_2 is more reactive when exposed to the plasma and no longer anisotropic when exposing. This is consistent with previous reports [63, 65, 66], and is suspected to arise from charge inhomogeneities in the SiO_2 substrate [170–172] or other SiO_2 surface properties. A broad range of plasma parameters in the remote regime were investigated for SL and BL samples on SiO_2, giving qualitatively similar results (isotropic SL etching).

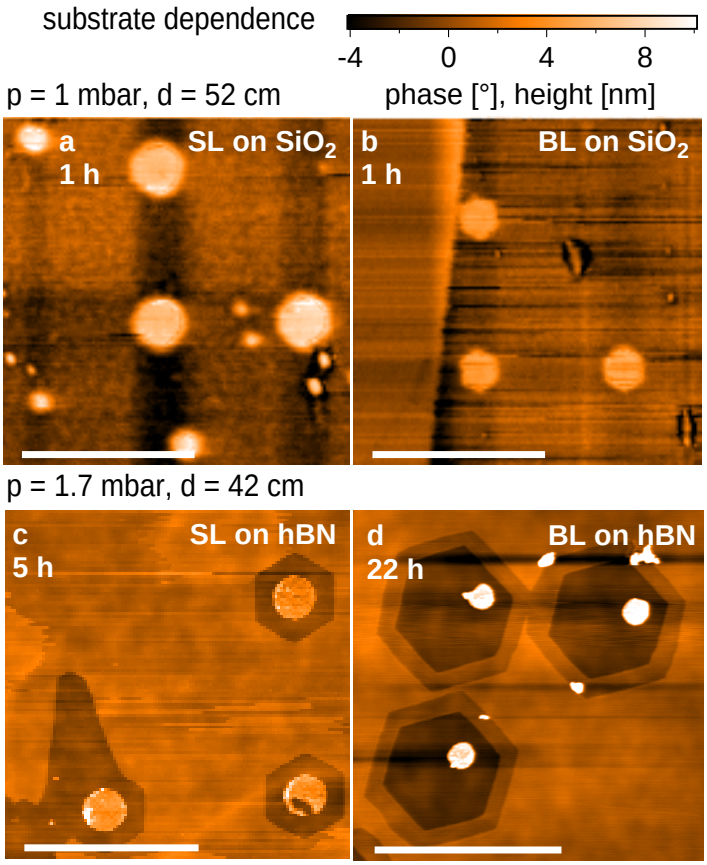

Figure 3.3: Substrate dependence of SL/BL graphene (a,b) AFM phase contrast images of a SL (a) and BL (b) section of the same flake on a SiO_2 substrate, etched for 1 h at $T = 450\,°C$. Round holes of 50 nm diameter were defined before H-etching. AFM topography image of a SL (c) and BL (d) flake on hBN etched for 5 h and 22 h, respectively. Holes of 200 nm (SL) and 100 nm (BL) were defined before etching. For (d) the color scale values are divided by four. The scale bars on all images are 1 μm.

The etch rate for SL and BL on SiO_2 is shown in Figure 3.4b. For the SL samples, only the EBL defined holes were evaluated, ignoring the plasma induced defects, since these do not etch from the beginning of the exposure. Clearly, for all plasma parameters studied, SL exhibits a significantly larger etch rate compared to BL [62, 66], as already visible from the AFM images in Figure 3.3a and b. The temperature dependence of the etch rate for both SL and BL on SiO_2 is shown in Figure 3.4c. The etch rates are strongly reduced at temperatures far above and below the process temperature, consistent with previous reports [62, 66], and consistent with reported hydrogen recombination rates on quartz increasing dramatically with temperature [173].

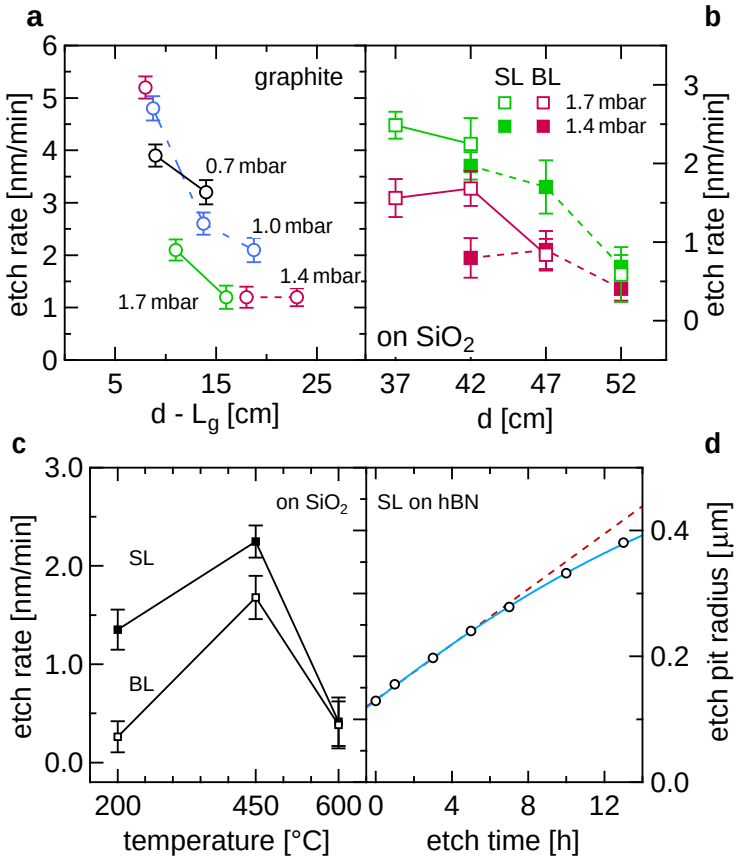

Figure 3.4: Anisotropic etch rates (a) Graphite anisotropic etch rate versus distance from plasma $d - L_g$ for several configurations. (b) Etch rate of SL and BL on SiO_2 at indicated parameters. (c) Temperature dependence of the etch rate of SL and BL samples on SiO_2. Error bars are standard deviations. (d) Average radius of a circle inscribed to the hexagonal etch pits as a function of exposure time for SL on hBN. Several etch pits were evaluated in order to obtain average size and standard deviation, where the latter is smaller than the diameter of the marker circle. The dashed red line is a linear fit to the points at ≤ 5 h, the blue curve is a tanh-fit shown as a guide for the eye.

To study the substrate dependence, we use high-quality hBN crystals as grown in Ref. [174]. SL and BL graphene were aligned and deposited onto areas covered with several 10 nm thick hBN lying on a SiO_2 substrate, following the recipe of Ref. [127]. Then, the same fabrication steps were repeated as before to fabricate circular graphene holes. Figure 3.3c shows an AFM topography image of SL graphene on hBN after 5 h of remote H plasma exposure. Clearly, very regular and well aligned hexagonal holes are visible, indicating a highly anisotropic etch. Etching of the hBN substrate by the H plasma was not observed, see profiles in SOM. We observed this anisotropic SL graphene

etching on hBN in more than 10 samples demonstrating the high reproducibility of the process.

In Figure 3.3d we present an AFM topography image of a BL graphene flake on hBN which was exposed to the H plasma for 22 h. We observe anisotropic etching of the BL flake with a slightly higher etch rate for the top layer (~ 0.3 nm/min) compared to the bottom layer (~ 0.2 nm/min), leading to a staircase-like structure at the etch pit borders. As seen in Figure 3.3d, the hexagons in the bottom and the top layer are of the same orientation. We note that the bottom layer is on hBN while the top layer is laying on graphene. The situation of the top layer is comparable to the SL etching on a graphite surface, where it was shown that the edges of the hexagons are aligned with the zigzag direction of the graphite lattice [60, 62]. Since the bottom layer exhibits hexagons oriented in the same direction as the hexagons emerging on the top layer, this further confirms that the etching of SL graphene on hBN is yielding etch pits oriented along the zigzag direction. The ribbon defined by the two left hexagons in Figure 3.3d has a width of about 20 nm, demonstrating the fabrication of nanoscale graphene structures with a remote H plasma.

The size of the SL hexagons as a function of exposure time is shown in Figure 3.4d. A linear fit (dashed red) is clearly over estimating the etch rate for long exposure times, deviating from the data by several standard deviations for the longest times. This hints towards either an insufficient H atom collection mechanism as the etch pits are growing larger or an aging effect of the tube as discussed above.

Raman spectroscopy on SL and BL samples on hBN was performed before and after H plasma etching. The D and D' disorder peaks were not seen (see SOM), both before and after H plasma etching. This suggests that neither defect formation nor hydrogenation [104, 114, 175, 176] is occurring in the bulk 2D during plasma etching, taking into account the annealing of the sample during the cool down phase [114], opening the door for high quality electrical properties.

The EBL defined circles stand very clearly visible in the center of the hexagons as an

elevated region, as seen in Figure 3.3c and d, growing in height but not diameter upon further H plasma exposure. These discs appear also away from the graphene flakes directly on the hBN, wherever circles were EBL/Ar/O_2-plasma defined. However, these elevated regions are also observed to shrink in height in ambient conditions. For a better understanding of the composition and behaviour of these surface structures, further investigations are required, which are however beyond the scope of this work. In addition, the adhesion between graphene and hBN often appears to be rather poor. Graphene flakes of several micrometres in length seem to be tilted with respect to the circular pillars induced by EBL. AFM tip forces or elevated temperatures may have shifted the flakes from their original position [177, 178].

3.4 Conclusion

In conclusion, we have investigated the pressure and distance dependence of the anisotropic etching of graphite surfaces in a H plasma. We have found that the etching characteristics can be divided into two regimes, the remote and the direct plasma regime. In the remote region of the plasma ($d' > 0$) etching only occurs at preexisting defect sites whereas for $d' < 0$ new defects are induced. Further, we have prepared SL and BL graphene flakes on SiO_2 and hBN substrates and exposed them to the remote H plasma. We observed isotropic etching of SL graphene on SiO_2, whereas on hBN it is highly anisotropic, exhibiting very regular and symmetric hexagonal etch pits. BL graphene, on the other hand, did not show a substrate dependence of the etching character and was anisotropic for both substrates.

By inducing artificial defects by lithographic means it becomes possible to pattern graphene nanostructures of various geometries with clean crystallographic edges defined by the etching in a remote H plasma. This leads to the opportunity to fabricate GNRs with well defined edges on a well suited substrate for electronic transport experiments, such as hBN. It would be interesting to study the etching process in dependence of the graphene electrochemical potential, which can be adjusted in-situ with a back gate

during the etching process. Also, a remote nitrogen plasma [179] could be investigated to be potentially used in a similar way to define armchair edges via anisotropic etching of atomic nitrogen.

3.5 Materials and Methods

A pure H plasma was created in a quartz tube through a matching network by a 13.56 MHz radio frequency (RF) generator at a typical power of 30 W. See Figure 3.5 for a sketch of the setup. This RF power was capacitively coupled to the 80 mm diameter tube by an outer electrode acting as a surfatron [180]. The pressure was regulated using a needle valve for 20 SCCM H gas flow of purity 6N. The sample was placed at a distance d from the end of the surfatron, was electrically floating and a three-zone furnace controlled the temperature T. The ion impact energy is roughly the difference between the plasma potential and the floating potential and is around $10 - 15$ eV with an average ion mass of 2 amu. We estimate the ion flux to be significantly lower than 10^{15} ions/cm^{2}s measured for a similar plasma setup but at lower pressure [176]. In order to characterize and optimize the anisotropic etching process, we studied the influence of pressure, distance, and temperature on the etching process, generally finding good repeatability. In particular, the graphene on hBN exposures have been reproduced more than ten times. Data points where a technical malfunction has occurred are not included in the evaluation.

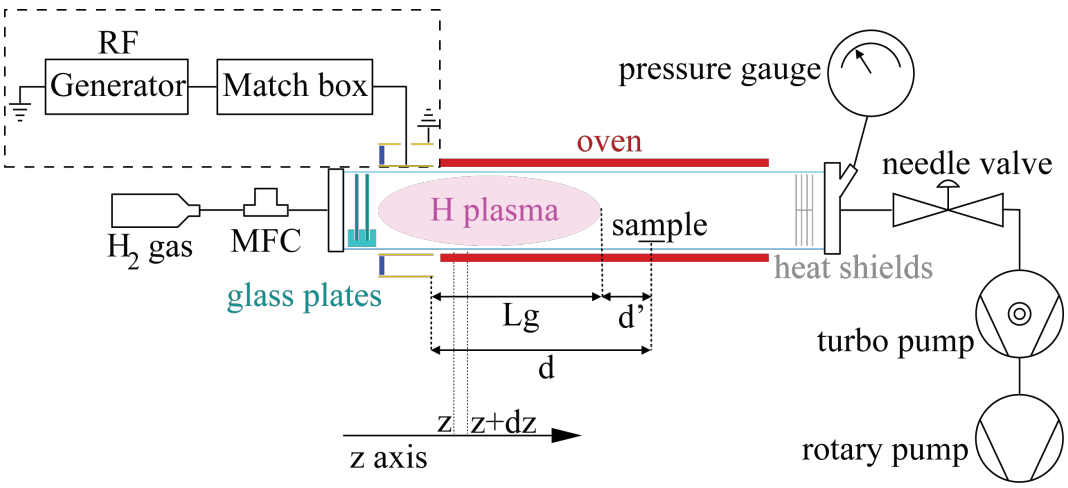

Figure 3.5: Setup of the plasma furnace. The quartz tube has a length of ca. 1 m and a diameter of 80 mm (drawing not to scale).

3.6 Acknowledgements

We would like to thank B. Eren, R. Maurand, C. Schönenberger and R. Steiner for helpful discussions. We acknowledge support from the Swiss Nanoscience Institute (SNI), NCCR QSIT and Swiss NSF. Growth of hexagonal boron nitride crystals was supported by the Elemental Strategy Initiative conducted by the MEXT, Japan and JSPS KAKENHI Grant Numbers JP26248061, JP15K21722 and JP25106006.

3.7 Author Contributions

D. H., S. Z., M. R., Y. K. and T. C. prepared samples and carried out the measurements. D. H., M. R. and D. Z. wrote the manuscript with contributions from all authors. L. M. helped with the plasma setup. K. W. and T. T. provided the hexagonal Boron Nitride.

3.8 Supplementary Information

3.8.1 Direct and remote plasma region

In Figure 3.6, AFM scans acquired after exposure of natural graphite samples for 1 hour to a pure hydrogen (H) plasma at a power of 30 W depict the influence of the

pressure and distance on the etching strength and type. For every pressure and distance combination a new graphite sample was fabricated as described in the main text. The matrix representation of the AFM scans of the complete set of investigated parameters remarkably demonstrates the transition from soft anisotropic etching (above or to the right of the cyan line) including only H atoms, to strong etching parameters (below or to the left of the cyan line) comprising also ions. The separation between the two regimes is based upon the size distribution of the hexagonal pits as ions are expected to induce defects acting as new etch sites throughout the whole exposure time. Lowering the pressure as well as decreasing the distance has the effect to increase the number of holes as well as the size distribution and depth of the etch pits, demonstrating an increase of the reactive particle density. On some of the AFM images, unintentional growth or deposition of some additional nanostructures such as worms or particles is seen, e.g. $d = 42\,\mathrm{cm}$ and $p = 1.4\,\mathrm{mbar}$ or $p = 0.7\,\mathrm{mbar}$.

For all AFM scans shown in Figure 3.6, the number of holes and their respective diameters are evaluated and plotted in histograms shown in Figure 3.7, describing a comparable picture as the AFM topography scans. Again, not only the amount of holes but also the width of the diameter distribution shows a strong dependence on pressure and distance. As for the AFM scans, the remote (upper right) and the direct (lower left) plasma region can be distinguished using the widths of the distributions in the histograms. In the lower right panels we estimated the number of holes for each diameter to > 12 and the width of the diameter distribution to be at least 600 nm, since an exact investigation of the hole number and diameter was not feasible (see Figure 3.6).

The number of hexagons etched into the graphite surface as well as the width of the hole diameter distribution reflect the number of ions inducing defects on the graphitic surface, assuming a low intrinsic defect density on the surface of the graphite samples.

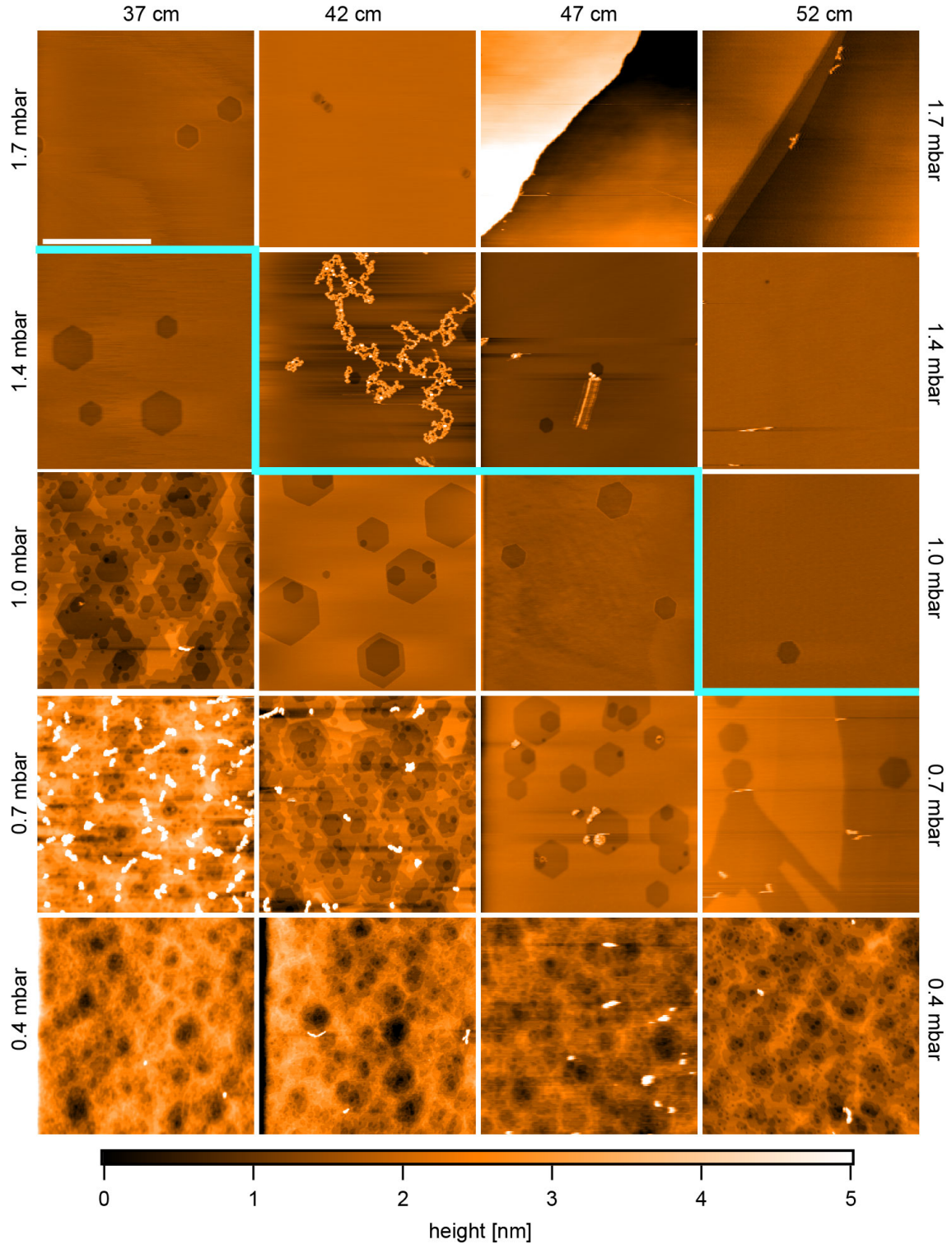

Figure 3.6: Distance and pressure dependence of graphite plasma exposure. AFM topography scans at all parameters investigated in Figure 1E in the main paper. All AFM images are $2 \times 2\,\mu\mathrm{m}^2$ in size. The cyan curve marks the transition from the remote (upper right) to the direct (lower left) plasma region. On some surfaces, particles are visible which probably are amorphous carbon residues, either grown or deposited during the etching process (see AFM scans for $p = 0.7\,\mathrm{mbar}$ and $d = 37\,\mathrm{cm}$ or $p = 1.4\,\mathrm{mbar}$ and $d = 42\,\mathrm{cm}$).

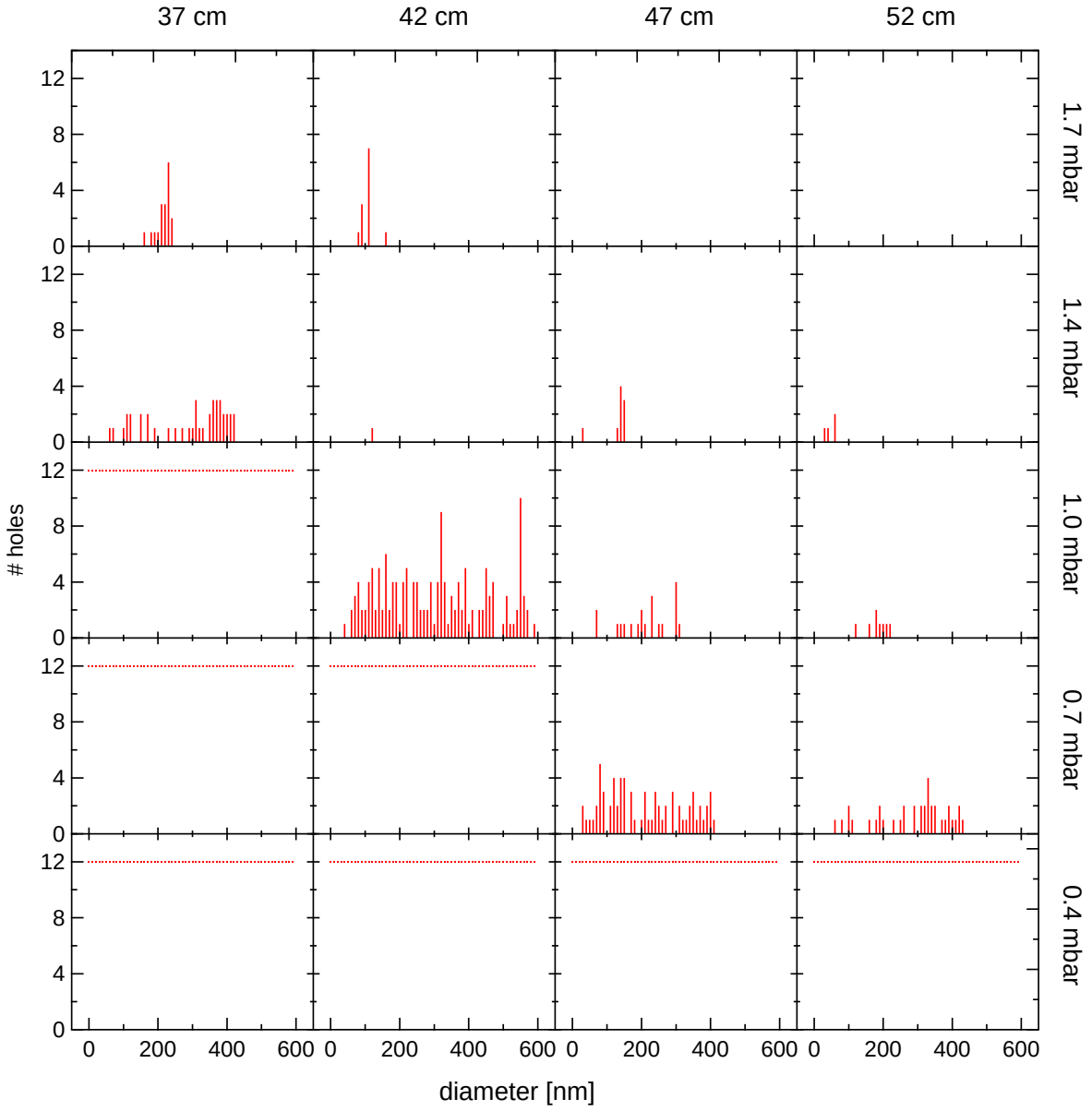

Figure 3.7: Distance and pressure dependence of graphite plasma exposure. Histograms (10 nm bin size) showing the number of holes for all pressure and distance parameters corresponding to Figure 3.6, obtained from $10 \times 10\,\mu\mathrm{m}^2$ AFM scans. For AFM scans of strongly etched surfaces, we plot 12 holes for every hole diameter.

3.8.2 Exponential decay of reactive particles

The number of holes (purple) and the width of the diameter distribution (orange) is shown in Figure 3.8 against the distance between the plasma edge and the sample, $\mathrm{d}' = d - L_g$. For $\mathrm{d}' < 0$ the sample is directly exposed to the glowing plasma, hence experiencing the impact of ions perforating the graphite surface with uncountable,

several layers deep holes. For d′ > 0 on the other hand, the hole number and the width of the hole distribution both appear to roughly decay exponentially with larger sample-plasma distance, with an 1/e decay length of ∼ 5 cm extracted from a fit to an exponential (dashed lines).

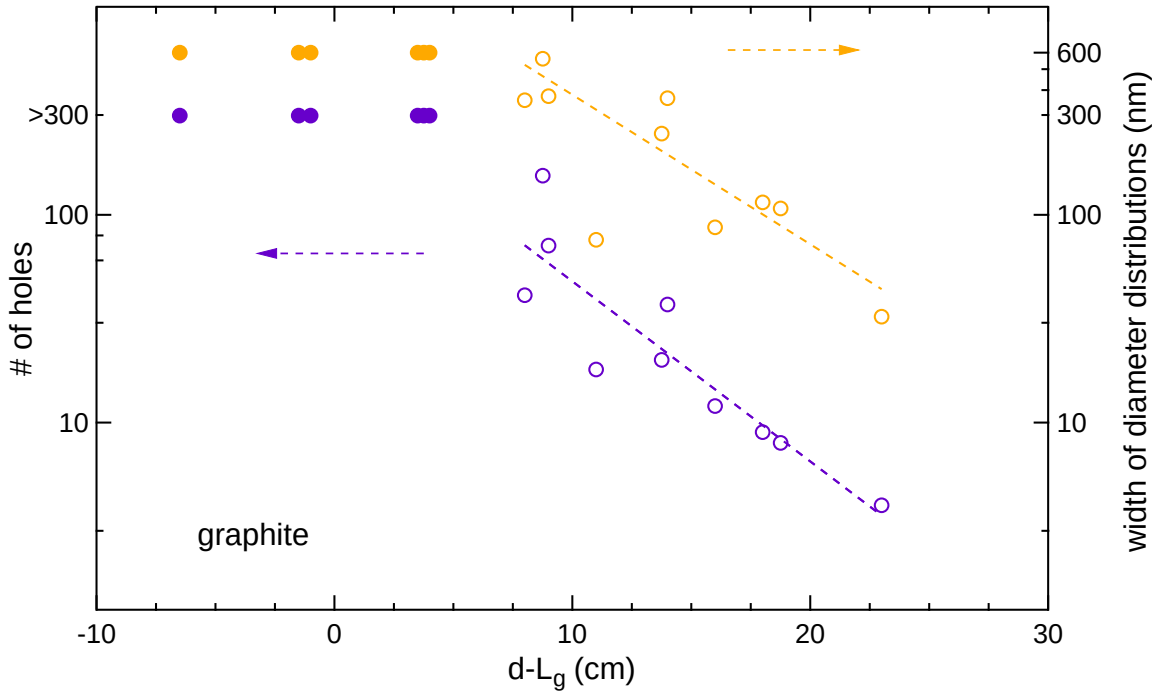

Figure 3.8: Number of holes (purple, left axis) and width of diameter distribution (orange, right axis) as a function of effective distance $d' = d - L_g$.

The radical concentration is decaying exponentially when moving down the axis of the tube, and is given by [96, 173]

$$[H] = [H]_0 \cdot \exp\{(-a\sqrt{p}d')\} \tag{3.1}$$

with sample-plasma edge distance d', concentration $[H]_0$ at $d' = 0$, pressure p, and the geometrical factor a:

$$a = \sqrt{\frac{v_{therm}\gamma}{R \cdot D'}}. \tag{3.2}$$

Here, $v_{therm} = \sqrt{8k_BT/(\pi m)} \approx 2'750\,\mathrm{m/s}$ is the molecular H_2 thermal velocity, with Boltzmann constant k_B, hydrogen mass m and temperature T. The material dependent

recombination coefficient [96, 173] of the radicals is $\gamma \approx 7.5{\cdot}10^{-4}$, $R = 4\,\mathrm{cm}$ is the radius of the quartz tube and $D' = 7.39\,\mathrm{atm\ cm^2/s}$ is the temperature dependent diffusion coefficient [181, 182] taken here at $\sim 700\,\mathrm{K}$ from Ref. [181]. Note the explicit pressure dependence of the decay length. Here, this results in a decay length of $\approx 12\,\mathrm{cm}$ at $p = 1\,\mathrm{mbar}$, which is consistent with our data. As mentioned in the main manuscript, the recombination of the radicals in the gas phase is expected to be irrelevant and the radicals only recombine at the surface of the quartz tube for the pressure range $p \sim 1\,\mathrm{mbar}$ used here.

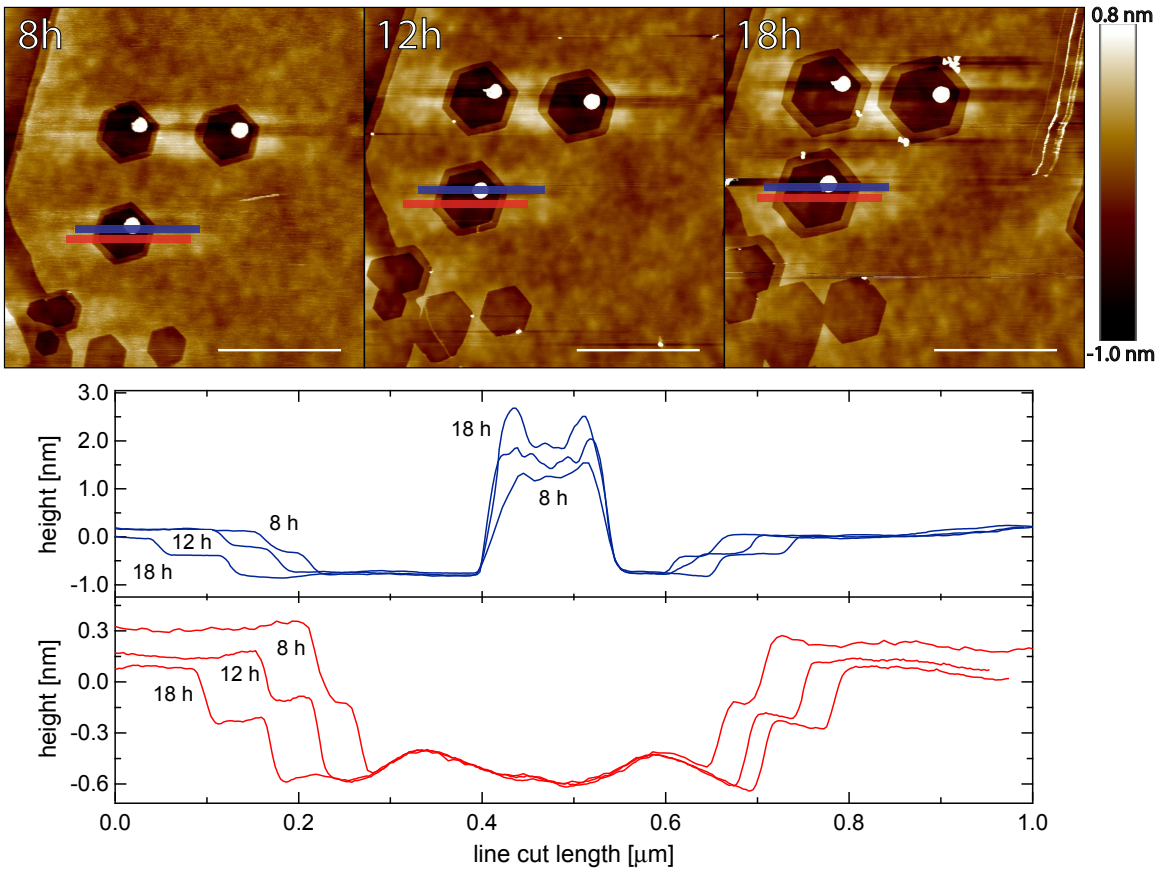

Figure 3.9: AFM images of BL graphene on an hBN substrate time series after 8 h, 12 h and 18 h of remote H-plasma exposure (upper panel). AFM profiles (lower panel) taken along paths indicated in upper panel (color coded). Averaging over the vertical range as indicated by the finite vertical width bars in the upper panel is performed to obtain an improved signal. These cuts demonstrate that the hBN substrate is not etched by the H-plasma, since the graphene step height is independent of exposure time. The center pillar appears to be growing with exposure time.

3.8.3 Raman measurements before and after plasma exposure

The influence of the H atoms on the graphene quality was further investigated by performing Raman measurements before, after 3 h and after 5 h of plasma exposure, as shown in Figure 3.10. To compare the Raman traces, we subtracted the background before normalizing the traces with the graphene G peak height at $\approx 1582 cm^{-1}$. The Raman scans taken on the bare hBN substrate in panel D are normalized to the SiO_2 peak (not visible) to allow comparison. All Raman measurements presented in this work were acquired with a green laser with a wavelength of $\lambda = 533\,\text{nm}$, where the bulk hBN E_{2g} peak at $1366\,\text{cm}^{-1}$ and the graphene D-peak at $1350\,\text{cm}^{-1}$) are close to each other. Nevertheless, in many cases a weak D-peak can still be reliably extracted.

Panel D shows Raman spectra of the hBN flake before (yellow), after 3 h (blue) and after 5 h (red) of remote H plasma etching. The hBN E_{2g} peak [183] shape, height and position does not significantly change, indicating no or only insignificant interaction of the hBN with the H plasma. Panel E shows Raman spectra acquired on bulk graphene, again before (yellow), after 3 h (blue) and after 5 h (red) of H plasma etching. We did not observe a D-peak in the bulk of the graphene flakes even after 15 h of plasma etching (not shown), indicating no induction of defects or hydrogenation of our samples [104, 114]. Note that after the end of the plasma exposure, the samples are annealed in vacuum while the oven is cooling down from process temperature to room temperature.

Significant information about the type and quality of edge can in principle be obtained from Raman spectra of the graphene edge [52]. However, care needs to be taken to not overheat and possibly reconstruct or otherwise change the edge with the laser [184] when illuminating the graphene edge on SiO_2 at a laser power of 1.5 mW or more. Our spectra do not meet these low power requirements. The damage threshold for graphene on hBN is not known, and study of these effects goes beyond the scope of this work.

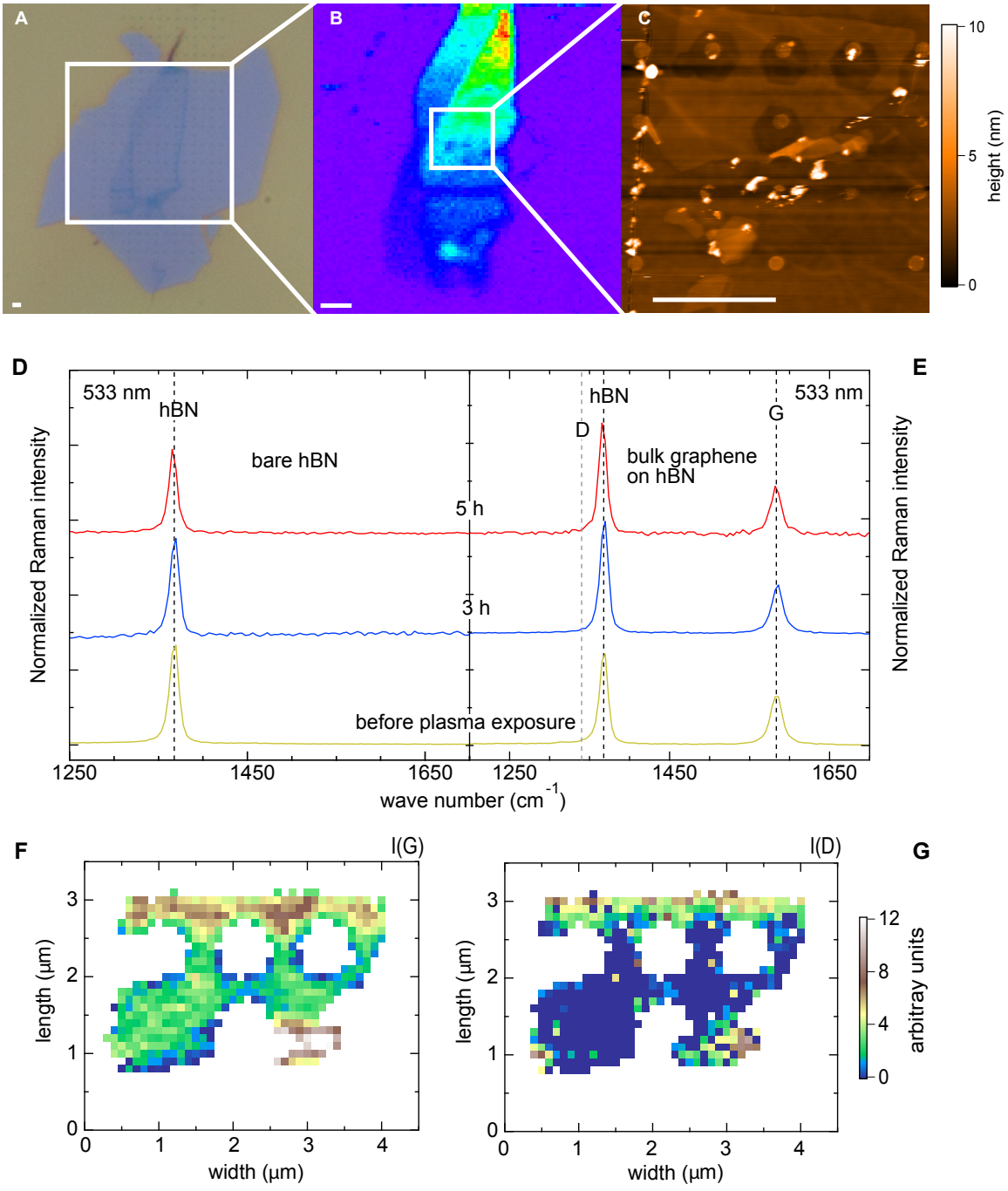

Figure 3.10: Raman spectra and spatially resolved Raman scans of the hBN sample in the main paper. Panel A: optical image of a graphene on hBN sample. Panel B: Raman map of the 2D peak of the same graphene flake before H plasma exposure. Panel C: AFM topography scan showing the region where the Raman single spectra were taken. The scale bars in Panel A to C are 2 μm. Panel D and E: Raman spectra of the bare hBN flake (panel D) and bulk graphene on hBN (panel E) before (yellow), after 3 h (blue) and after 5 h (red) of remote plasma exposure. The Raman spectra are vertically shifted for clarity. Panel F and G: 2D maps of the G peak (panel F) and D peak (panel G) of the flake region shown in panel C.

4 Characterization of Hydrogen Plasma Defined Graphene Edges

Mirko K. Rehmann*, Yemliha B. Kalyoncu*, Marcin Kisiel, Fabian Müller, Ernst Meyer and Dominik M. Zumbühl

Department of Physics, University of Basel, CH-4056 Basel, Switzerland

Nikola Pascher

Nanosurf AG, Gräubernstrasse 12, 4410 Liestal, Switzerland

Franz J. Giessibl

Department of Physics, University of Regensburg, 93053 Regensburg, Germany

Kenji Watanabe and Takashi Taniguchi

National Institute for Material Science, 1-1 Namiki, Tsukuba 305-0044, Japan

Ming-Hao Liu

Department of Physics, National Cheng Kung University, Tainan 70101, Taiwan

This chapter is in preparation for publication.

Abstract

We investigate the quality of hydrogen plasma defined graphene edges by Raman spectroscopy, atomic resolution AFM and low temperature electronic transport measurements. The exposure of graphite samples to a remote hydrogen plasma leads to the formation of hexagonal shaped etch pits, reflecting the anisotropy of the etch. Atomic resolution AFM reveals that the sides of these hexagons are oriented along the zigzag direction of the graphite crystal lattice and the absence of the D-peak in the Raman spectrum indicates that the edges are high quality zigzag edges. In a second step of the experiment, we investigate hexagon edges created in single layer graphene on hexagonal boron nitride and find a substantial D-peak intensity. Polarization dependent Raman measurements reveal that hydrogen plasma defined edges consist of a mixture of zigzag and armchair segments. Furthermore, electronic transport measurements were performed on hydrogen plasma defined graphene nanoribbons which indicate a high quality of the bulk but a relatively low edge quality. These findings are supported by tight-binding transport simulations. Hence, further optimization of the hydrogen plasma etching technique is required to obtain pure crystalline graphene edges.

4.1 Introduction

Graphene edges play an important role in many physical phenomena [10, 95]. In particular, the edge shape defines the electronic properties of graphene nanoribbons (GNRs). Crystallographic edges of the armchair (AC) type are predicted to enable the creation of helical modes and Majorana fermions [11] and to be excellent candidates for the implementation of spin qubits [12]. For pure zigzag (ZZ) edges, edge-magnetism was predicted to emerge which can be used for spin filtering [30]. For these effects to be observable in experiment, high quality edges are necessary because edge disorder suppresses magnetic correlations [29] and leads to electron localization which complicates transport studies [86, 89, 162–165]. It has been observed, that GNRs fabricated by ebeam lithography and reactive ion etching (RIE) in an Ar/O_2 plasma have a high degree of edge disorder [86, 89, 163–165]. Hence, other approaches to create GNRs with high quality edges are pursued such as carbon nanotube unzipping [36, 37, 185], ultrasonication of intercalated graphite [38], chemical bottom up synthesis [39, 40], anisotropic etching by nickel nanoparticles [46], anisotropic etching during CVD processing [47–50], or carbothermal etching of graphene sheets [51–54, 54]. Another promising approach which was considered to create high quality crystallographic graphene edges is to employ a hydrogen (H) plasma to perform anisotropic etching of graphite and graphene [60–67, 79, 186].

4.2 Main Experimental Findings

In this study, we characterize H plasma defined graphene edges on graphite and single layer (SL) graphene on hexagonal boron nitride (hBN) by means of atomic force microscopy (AFM), Raman spectroscopy and low temperature electronic transport measurements. We find high quality ZZ edges on graphite surfaces, manifested by the absence of the D-peak in the Raman spectrum [187, 188]. In contrast, SL graphene on hBN edges exhibit a large D-peak which is indicative of the presence of edge disorder

and AC segments. In comparison, the D-peak intensity measured at H plasma defined edges is twice as large as on edges created with RIE. Polarization dependent Raman measurements reveal an edge configuration which consists of approx. 60 % ZZ and 40 % AC segments. Moreover, electronic transport measurements performed across a *pnp* junction of a H plasma treated graphene flake exhibit Fabry-Pérot oscillations, reflecting the high electronic quality of the bulk graphene flake after H plasma exposure. However, at high magnetic field valley-isospin oscillations appear and indicate a rather low edge quality. In a second device we investigate transport through narrow GNRs with RIE defined edges and H plasma defined edges and find comparable mobilities for these two edge types.

The results from the Raman experiments and the electronic transport studies give a consistent picture, indicating the presence of disorder at H plasma defined graphene edges and thus the need for optimization of the etching process to enable the creation of high quality ZZ edges.

4.3 Results and Discussion

4.3.1 High Quality ZZ Edges on Graphite

In a first step of the experiment, we intend to visualize the edge of a hexagon created by H plasma exposure, to learn its crystallographic direction and its atomic configuration. Therefore, we record topography and force images by means of ambient qPlus based atomically resolving AFM [189] (Figure 4.1a - c) on a graphite surface which shows several hexagons. In panel a we show one corner of a hexagon, and its edges are demarcated with white dashed lines. From a to c, black squared regions are scanned with higher resolution with the same sample orientation. Figure 4.1c is a constant height atomic resolution force image of the graphite surface close to the edge and the hexagonal lattice structure is superimposed on the image. The green dashed line in panel c is drawn parallel to the white dashed lines in panel a and b. This picture clearly

shows that the edge is in parallel to the ZZ direction, in agreement with recent findings [62]. Although the above discussed AFM measurements allow to unambiguously assign the macroscopic edge orientation of the hexagons to the ZZ direction, thermal drift hindered to position the edge inside the scan range for the atomic resolution imaging, hence it was not possible to actually visualize the atomic configuration of the hexagon edge.

To access information about the edge configuration on the atomic level, Raman measurements are conducted on a graphite flake which was exposed to H plasma under similar conditions as the sample investigated in Figure 4.1a to c. 41 Raman spectra are taken over a $5 \times 5\,\mu\mathrm{m}^2$ region, covering the whole area as shown in Figure 4.1d with the grid of black circles. This web of spectra makes sure that the surface is fully covered. The resulting 41 spectra are laid on top of each other in panel e. These 41 spectra are essentially the same; in particular, the G and 2D-peaks fit to each other and there is no D-peak as seen in Figure 4.1e. The absence of the D-peak in any of these spectra indicates high quality ZZ edges since any edge disorder would result in some D-peak intensity [107–109, 187, 188].

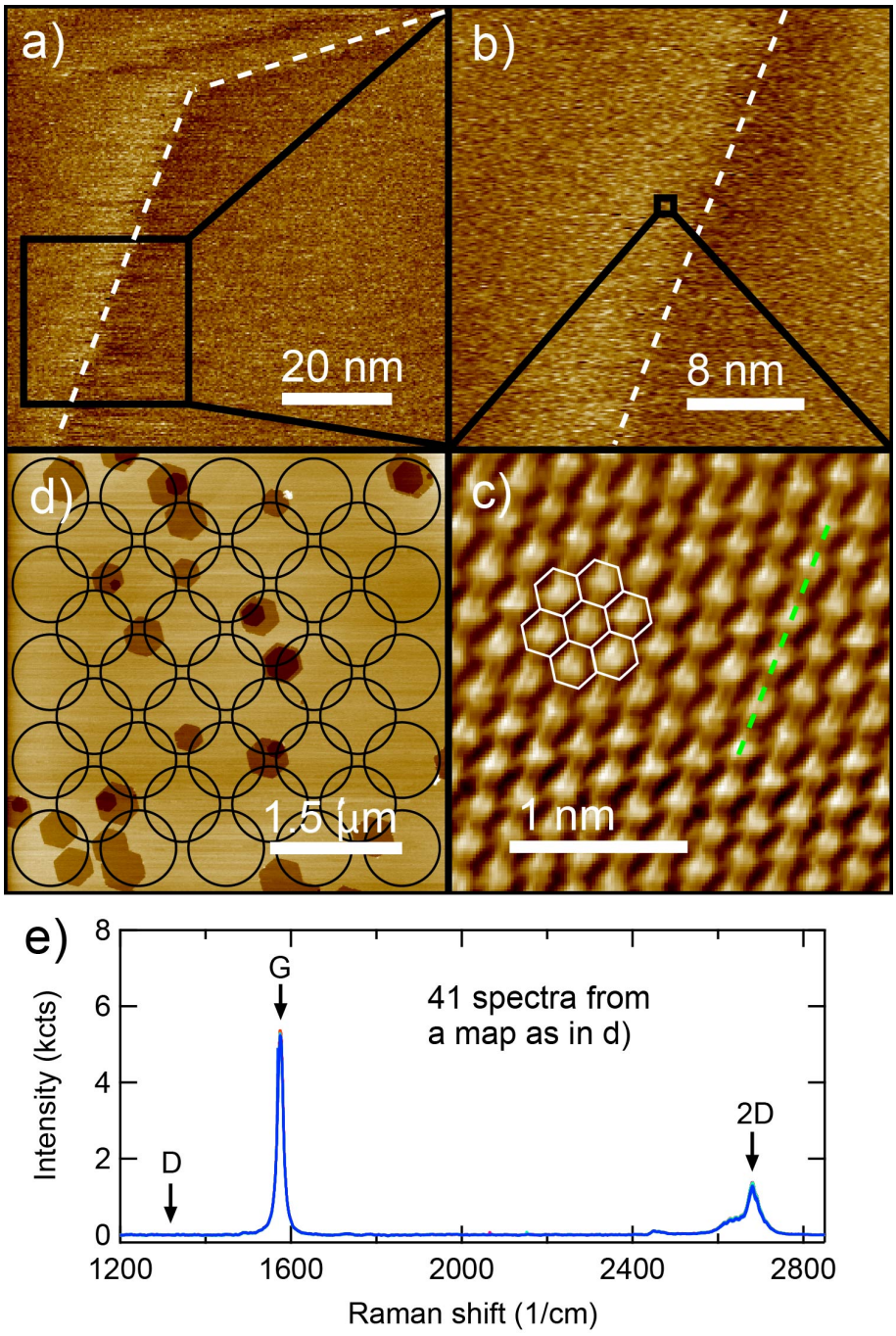

Figure 4.1: AFM maps and Raman spectra of H plasma etched graphite (a) AFM height image of a section of a hexagonal shaped etch pit on a graphite flake which was exposed to a remote hydrogen plasma. (b) Zoom-in on data shown in panel a. (c) Atomic resolution AFM force image of the black squared region in b. The graphene lattice is superimposed in white. The green dashed line indicates the ZZ direction and is parallel to the hexagon edges (white dashed lines in a and b). (d) Tapping mode AFM image of a $5 \times 5\,\mu m^2$ area of a graphite flake. The black circles with a diameter of 800 nm, given by the laser spot size, indicate the locations at which Raman spectra were taken. (e) 41 Raman spectra laid on top of each other, all recorded with circularly polarized light.

4.3.2 Raman Spectroscopy on SL Graphene Hexagons on hBN

Next, we investigate the edge quality of hexagons created in SL graphene flakes on a hBN substrate. In a previous work [67], we showed that the character of the etch is substrate dependent and that it is also possible to get highly anisotropic etching if SL graphene is placed on a hBN substrate. However, it remains unclear how good the edge quality is on a microscopic level. To find out, we prepare a SL graphene flake on a hBN substrate and etch it for 4 h in a remote H plasma to perform Raman measurements at the created graphene edges.

Figure 4.2a shows an AFM height image of a SL graphene flake on a hBN substrate. The two darker disks are induced defects which we fabricated by means of ebeam lithography and RIE in an Ar/O_2 plasma. Upon H plasma exposure, they transform into regular hexagonal shaped etch pits. Moreover, smaller hexagons grow next to the two big ones. Those smaller hexagons are either grown from lattice defects already present after exfoliation or induced during H plasma exposure (i.e. by highly energetic ions). To learn about the edge quality of such SL graphene edges, we record Raman spectra at the locations indicated by the red and green dashed circles in panel a and show them in panel b. We observe the graphene related G and 2D-peaks and the hBN peak coming from the substrate. More importantly, the graphene D-peak appears to the left of the hBN peak at both measurement locations. The difference in intensity could stem from differences of the probed edge segment length. Further, we overlay a spectrum taken on the graphite sample shown in Figure 4.1 (blue curve). Apparently, there is no D-peak for the graphite case whereas we do observe a D-peak for the SL graphene on hBN edges. This indicates, that there is a significant amount of disorder present at the hexagon edges in SL graphene.

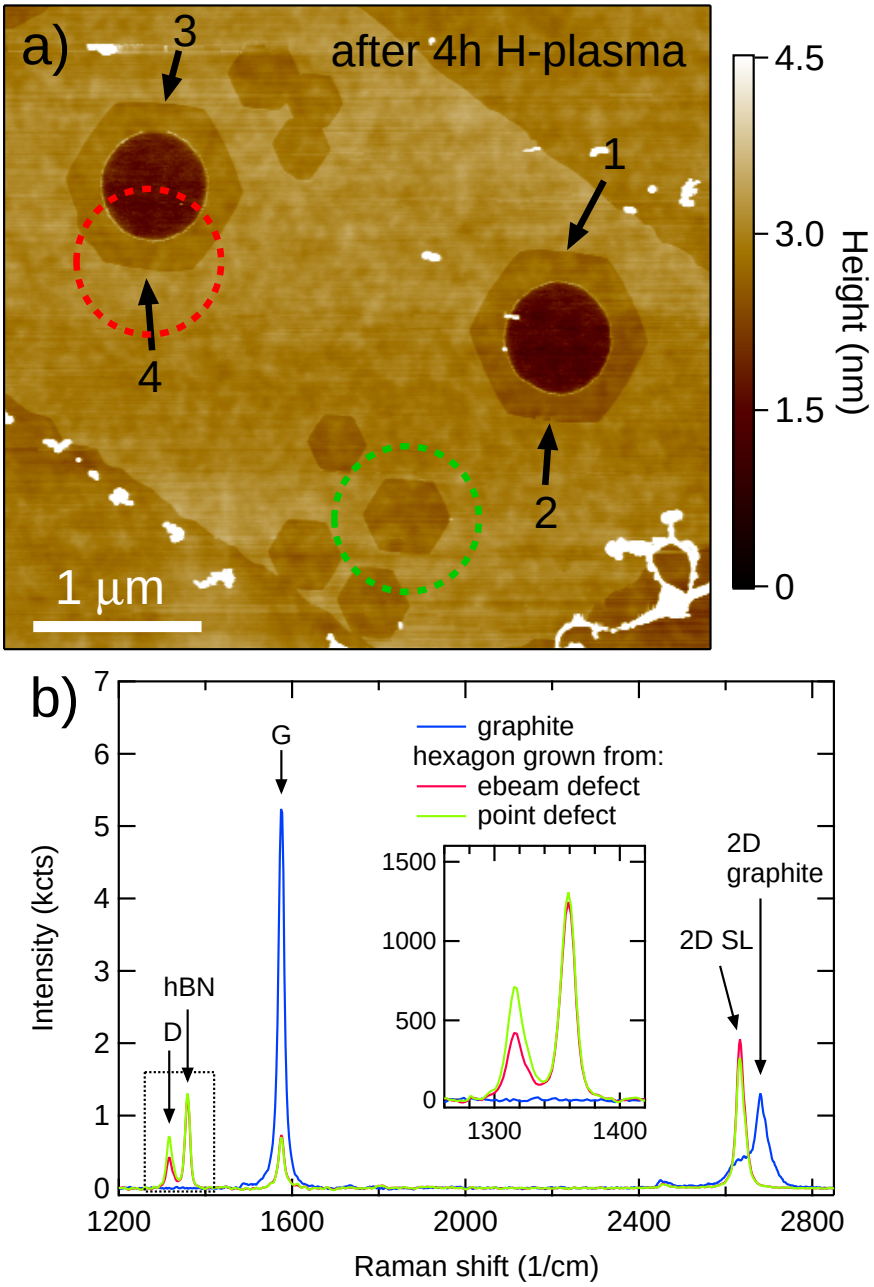

Figure 4.2: AFM height image and Raman spectra of H plasma defined SL graphene edges (a) AFM height image of a SL graphene flake on a hBN substrate after 4 h of remote H plasma exposure. Two round shaped defects of a diameter of 600 nm were created by ebeam lithography and RIE etching in a Ar/O_2 plasma. They serve as nucleation centers for the anisotropic etch which transforms them into hexagonal etch pits. Besides the two patterned defects, there are defects which grow into the smaller hexagons visible next to the larger ones. The red and green dashed circles indicate the locations at which the Raman spectra shown in b were recorded. The black numbers denote the different investigated edge segments of which the measurements are shown in Figure 4.3f. (b) Raman spectra of graphite (blue) and of SL graphene edges encircled by the green and red dashed circles in panel a. The inset shows the region of the D-peak. All spectra are recorded with circularly polarized light.

Obviously, the hexagon edges created in SL graphene on hBN are of different quality compared to the edges of hexagons formed on graphite. Already in our previous study [67] we have observed that the substrate has a big influence on the etching character. Although hBN as a substrate allows for highly anisotropic etching, the edge configuration on a microscopic level is different from the one on graphite surfaces. This could be due to several reasons, e.g. the different lattice constants of graphene and hBN could potentially lead to strain effects [190] or to the appearance of Moiré superlattice effects [172] which could influence the quality of the H plasma etching process.

4.3.3 Evolution of the Raman D-mode from RIE to H Plasma Defined Graphene Edges

Next, we study the evolution of the observed D-peak over a time sequence of the etching process. This series of measurements shows how the edge quality evolves from a RIE defined circular hole to H plasma defined edges and further studies the effect of annealing. We started with defining circular holes by means of ebeam lithography and RIE with an Ar/O_2 plasma, which creates disordered edges without any defined crystal orientation [86, 89, 163–165, 191]. The AFM image of this RIE defined circular hole is shown in Figure 4.3a. Raman single spectra were recorded with circularly polarized light at the bottom edge of the hole indicated by the black dashed circle. Circular polarization ensures that the Raman signal is collected equally at every point of the edge, regardless of the edge direction. After the measurements, the sample is exposed to the remote H plasma first for 2 hours and then 2 more hours, creating hexagonal etch pits of increasing diameter as shown in Figure 4.3b and c. As a final step, we annealed the sample in vacuum. After each step, Raman spectra are measured at the same location.

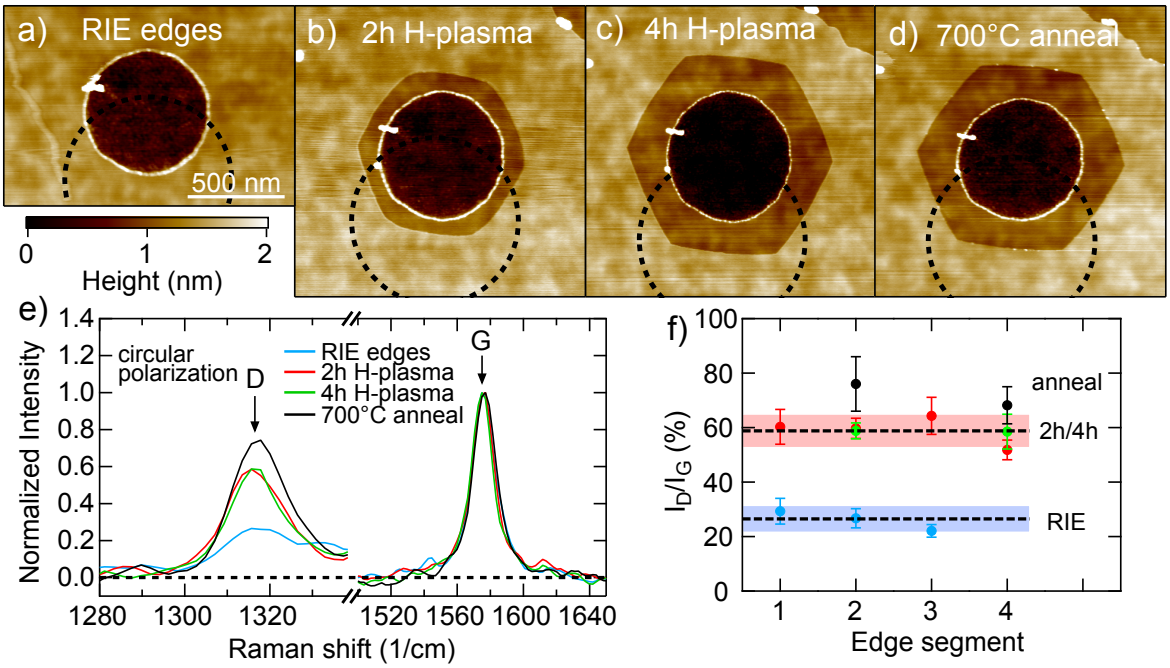

Figure 4.3: Comparison of RIE defined edges with H plasma defined edges (a) to (d) AFM height images of ebeam defined defects in SL graphene on hBN, after RIE a, after 2 h b and 4 h c of remote H plasma etching and after annealing at $T = 700\,°C$ for $30\,min$ at a pressure of $1.6 \cdot 10^{-3}$ mbar d. The black dashed circles indicate the spot size of the Raman measurements. (e) Raman spectra recorded with circularly polarized light at the bottom edge of the right hole (edge segment #2, see Figure 4.2a after RIE, 2 h, 4 h and after annealing at $T = 700\,°C$. The spectra are normalized to the G-peak and each curve is an average of five measurements. (f) Normalized D-peak intensities recorded at different edge segments as labeled in Figure 4.2a. The blue and red shaded bands are the standard deviations from all the corresponding measurements.

In Figure 4.3e, four Raman spectra measured at different stages shown in a to d are plotted, normalized to the G-peak height. All spectra are averages over five measurements recorded under same conditions and looking all very similar. As expected, the RIE defined hole shows a D-peak (blue curve). After the first H plasma etching (red curve) the D-peak intensity surprisingly increases approximately by a factor of two and stays at this level for further etching (green curve). Finally, annealing at an elevated temperature of 700 °C again increases the D-peak (black curve), suggesting structural edge defects as the D-peak origin, since annealing likely would reduce, not increase, the amount of edge hydrogenation. We note also that when investigating bulk graphene with Raman spectroscopy, where no edge segments are inside the laser spot, we do not observe any D-peak, consistent with previous work [114], indicating the absence of bulk

hydrogenation (see supplementary online material (SOM) S1), though it is in principle possible that annealing at even higher temperatures might be required to remove hydrogen from the edge. The bright circular rim of the RIE defined circular hole on hBN (Figure 4.3b - d) does not contribute to the graphene bands in the Raman spectrum (see SOM S1). Further, changes in both graphene area and edge length enclosed in the laser spot are giving negligible contributions to the evolution of the D-peak; see SOM S5 for details. In Figure 4.3f we find the same trend in D-peak intensity for all four different edge segments which are indicated in Figure 4.2a by the black arrows and numbers. The values for different edge segments stay in a narrow window, giving consistent results.

The increase of the D-peak upon the first H plasma exposure could stem from the formation of AC segments at the edges, since AC edges are highly D-peak active [107–109, 187, 188]. From previous studies [67], it is clear that the direction of the edge generally goes along the ZZ direction. Hence, we conclude that the SL graphene edges on hBN run along the ZZ direction but have a substantial amount of disorder, probably at least partially in form of AC segments. To test this hypothesis, we study the edge disorder with the angular dependence using linearly polarized light [107, 117].

4.3.4 Polarization Angle Dependent Raman Measurements

Xu and coworkers in ref. [117] have observed edge reconstruction on ZZ edges due to thermal treatment. Since we etch our samples at a temperature of $T = 400\,^{\circ}\mathrm{C}$, it might be that also our graphene edges experience thermal reconstruction. Indeed, it is theoretically predicted that an AC edge has lower energy compared to a ZZ edge [192]. A model to extract the relative abundance of AC-30° segments and point defects was proposed in ref. [117]. We apply this model to our data and see that the observed D-peak signal only comes from AC-30° segments and that essentially no point defects are present (see SOM S4). Furthermore, Casiraghi et al. in ref. [107] proposed a theory to calculate the ratio of ZZ segments to AC-30° segments which we apply to our data; see

Figure 4.4. Panel a shows an AFM height image of a hexagon created in SL graphene supported on a hBN substrate. The Raman spectra were recorded at the laser spot indicated by the white dashed circle. The angle θ of the polarization with respect to the edge is marked in light blue. In panel b we plot the normalized D-peak intensities as a function of θ. The blue curve is a fit to equation 1 of ref. [107]. Since our hexagons exhibit rather straight edges, we take an equal amount of +30° and -30° AC segments. We find that our graphene edge consists of about $59 \pm 2\,\%$ ZZ and $41 \pm 2\,\%$ AC-30° segments. This is in excellent agreement with a second data set acquired on a different hexagon on the same graphene flake (see SOM S4 for data taken at different stages of the etching process).

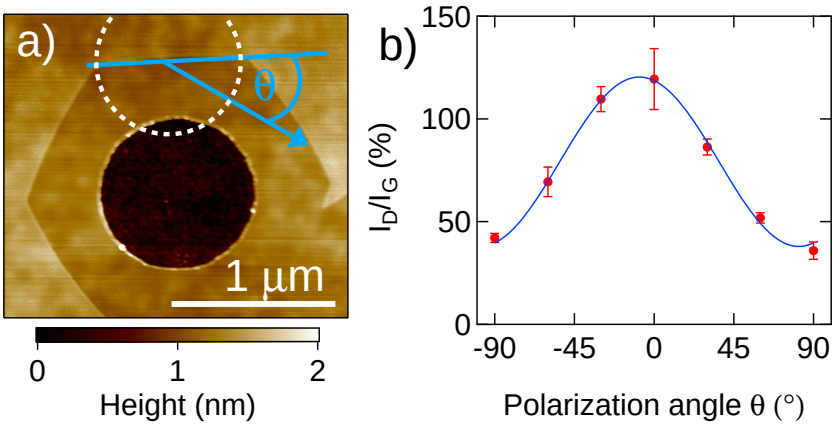

Figure 4.4: Polarization angle dependence of a SL/hBN graphene edge (a) AFM height image of a hexagonal etch pit in a SL graphene flake on a hBN substrate after 6 h of remote H plasma exposure. The white dashed circle indicates the laser spot where the Raman spectra were recorded and θ denotes the angle of the laser light polarization with respect to the graphene edge. (b) Normalized D-peak intensity for different polarization angles θ. The blue curve is a fit to equation 1 of ref. [107] yielding $I(D)_{min} = 38 \pm 2$, $I(D)_{max} = 120 \pm 2$ and $\theta_{max} = -8 \pm 1$.

Besides the polarization dependence of the D-peak, the G-peak can also serve to get insight into the structure of graphene edges [193, 194]. In particular, a clean AC edge is expected to exhibit a $\cos^2(\theta)$ dependence and a clean ZZ edge a $\sin^2(\theta)$ dependence. An edge with a mixture of ZZ and AC segments would result in a corresponding mixed angular dependence with a weak amplitude of modulation. This is what is seen in our data and is thus again consistent with a similar mixture of ZZ and AC segments.

4.3.5 Fabry-Pérot Interference in a H Plasma Defined GNR pnp Junction

Next, we investigate the influence of H plasma treatment on the electronic property of graphene. In particular, we address the quality of bulk graphene and features arising from the H plasma defined graphene edges. To this end, we fabricate a SL GNR with H plasma defined edges following the ZZ direction of the crystal lattice, done as follows. After a first exposure of the graphene flake to the remote H plasma, a few hexagons grow from which we can learn the crystallographic orientation of the flake. Next, the graphene flake is cut into stripes which run parallel to the hexagon sides and hence parallel to the ZZ direction of the crystal lattice (see Figure 4.5a). Subsequently, another H plasma exposure leads to etching from the ribbon edges and thus leaves a GNR with H plasma defined graphene edges. We note that the investigated GNR is free of defects in form of missing carbon atoms, because otherwise these defects would have grown into hexagons (see panel b). The white dashed rectangle in panel b indicates the location of the top gate which was fabricated after encapsulation with hBN [129]. In panel c, a schematic of the cross section of the device is shown.

The local top gate and the global back gate allow to tune the charge carrier densities inside and outside the top gated regions individually. This enables the possibility to tune the system into bipolar regimes, i.e. *pnp* or *npn*, thus creating two *pn* junctions which can form a resonance cavity for the charge carriers. If the charge carriers move ballistically inside such a cavity, Fabry-Pérot resonances appear [195–197]. In panel d, we show the conductance as a function of back gate voltage V_{BG} and top gate voltage V_{TG} in the *pnp* regime, at zero magnetic field. Clear fringes due to Fabry-Pérot resonances are seen to be parallel to the diagonal white dashed line which marks the zero carrier density in the dual-gated region. This indicates that the observed fringes come from Fabry-Pérot interferences within the topgated cavity. The grayscale inset overlaid on Figure 4.5d is obtained by a quantum transport simulation based on an infinitely wide graphene lattice [197, 198], with the electrostatically simulated barrier profile following the geometry of the device implemented. The simulation is obtained

without fit parameters and matches very well with the experiment.

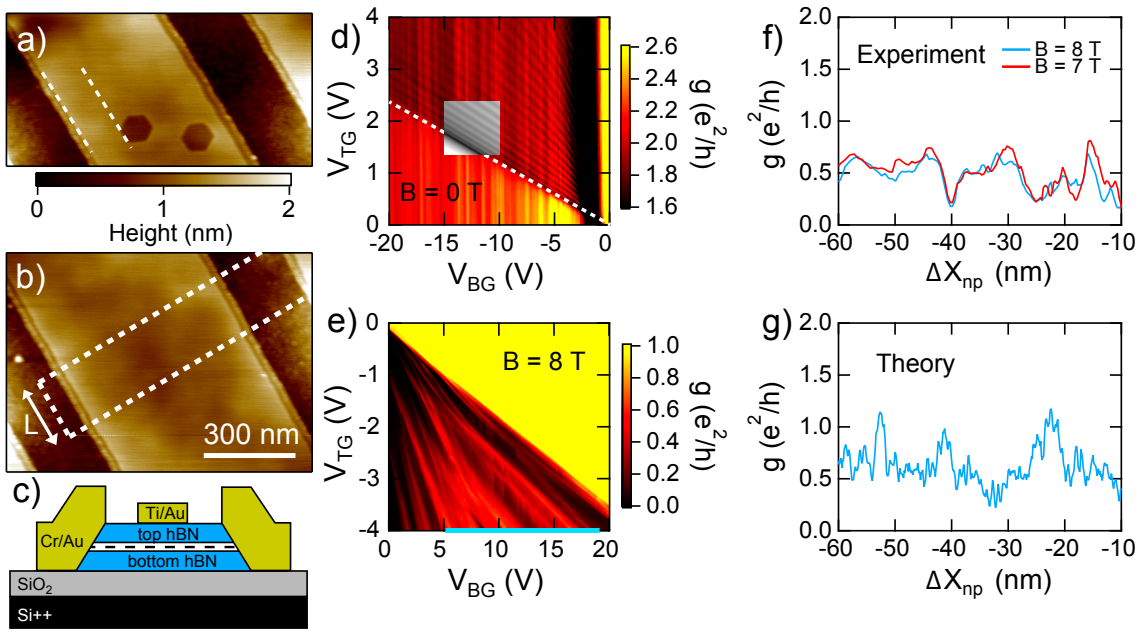

Figure 4.5: Electronic transport measurements of encapsulated GNR with H plasma defined edges (a) AFM height image of a SL GNR. The white dashed lines indicate that the hexagon edges are well aligned with the GNR edges. (b) AFM height image of the GNR on which electronic transport was measured. The white dashed lines indicate the location of the 200 nm top gate which was evaporated on top of a hBN capping layer. The length L of the charge carrier cavity is tunable with gate voltages. (c) Device schematic of the encapsulated GNR with a global back gate and a local top gate. The black dashed line indicates the SL GNR. (d) Differential conductance as a function of back gate V_{BG} and top gate V_{TG} voltage at $B = 0\,T$ in the *pnp* region (n under the top gate). The greyscale inset is obtained by a simulation and matches very well with the experiment. The white dashed line marks the charge neutrality point in the dual gated regime. (e) Similar map as in d but recorded at $B = 8\,T$ and in the *npn* regime. In the bi-polar regime, resonances fanning out linearly from the charge neutrality point are visible. (f) Cut along the blue line in e and an additional curve recorded at same gate voltages but at $B = 7\,T$. The x-axis was converted from V_{BG} to the *np*-interface location relative to the physical top gate edge ΔX_{np}; see SOM S7 and S8 for details. (g) Calculation of the conductance through a GNR following the ZZ direction with disorder in form of AC-30° segments and a bulk disorder of 35 meV plotted versus ΔX_{np}.

The oscillation frequency of the Fabry-Pérot resonances is linked to the cavity length L. We extract values for L in the range of $L = 160\,nm$ to $330\,nm$ (see SOM S3 for details about the cavity length extraction). Since L represents a lower bound for the mean free path, we can calculate the corresponding lower bound of the mobility, which

is approximately 60 000 cm^2/Vs, reflecting the high electronic quality of graphene after H plasma exposure.

4.3.6 Valley-Isospin Dependent Conductance Oscillations in a H Plasma Defined GNR

We continue with high-field magnetotransport measurements, and follow an analysis based on ref. [122] to study the edge quality of our GNR sample. At high magnetic field, the edge state of the lowest Landau level is valley-isospin-polarized depending on the edge of the GNR [124]. By tuning the gate voltages, the zero-density region, i.e., the *pn* and *np* interfaces, can be controllably moved along the edges of the GNR, revealing the edge-specific conductance oscillations [122].

The conductance map $g(V_{\mathrm{BG}}, V_{\mathrm{TG}})$ at $B = 8\,\mathrm{T}$ is shown in Figure 4.5e, where the fringes fanning out from the origin seen in the *npn* regime (bottom left part) behave qualitatively similar as those reported in ref. [122], indicating the emergence of the valley-isospin physics. Similar behavior is also found in the *pnp* regime (not shown). In Figure 4.5f, we show a cut (blue curve) from the map of panel e at $V_{\mathrm{TG}} = -4\,\mathrm{V}$ (marked by the blue line) showing weak oscillations around $\sim 0.5\,e^2/h$. We re-interpret the back gate voltage values in terms of Δx_{np}: the change of the position of the gate-defined *np* interface with respect to the left edge of the top gate based on our electrostatic simulation (see SOM S7 and S8). Another cut (red curve) recorded at $B = 7\,\mathrm{T}$ shows a rather similarly oscillating curve, indicating that the oscillations have already developed at lower field. This further gives a sign that the observed oscillations originate from the edge-specific valley-isospin.

To further confirm the origin of the experimentally observed conductance oscillations shown in Figure 4.5f, we have performed quantum transport simulations for both AC and ZZ edges with various types of disorder, see Figure 4.6; see SOM S7 for details.

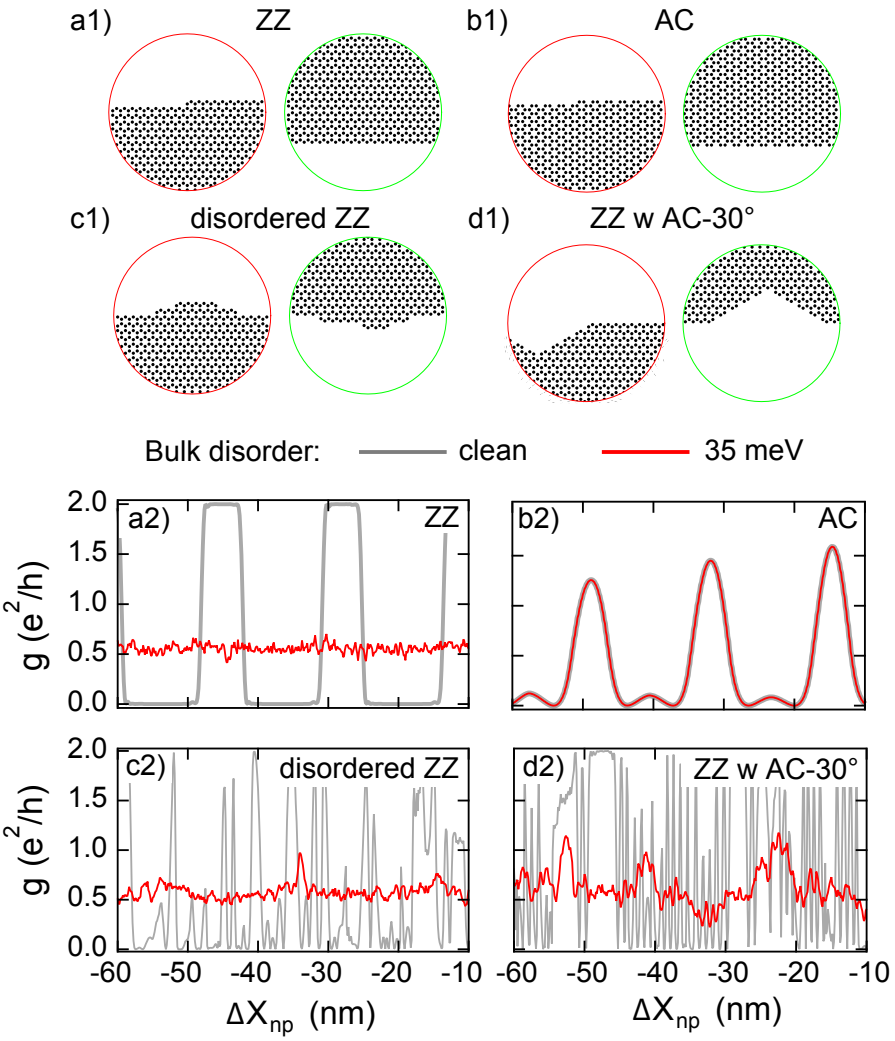

Figure 4.6: Quantum transport simulations (a1) Ribbon with a perfect ZZ edge at the bottom and one-atom steps at the top edge. (b1) Similar case as in a1 but following the AC direction. (c1) Ribbon following the ZZ direction but with a large amount of edge disorder on both edges. (d1) ZZ edge ribbon with 40% fraction of randomly distributed AC-30° segments on both sides (as found in experiment) with a depth of 1 nm. The red and green circles are zoom-ins on the top and bottom edges of the ribbons,respectively. (a2) to (d2) Conductance as a function of ΔX_{np} with and without disorder, as labeled. Only the ZZ with AC-30° segments case qualitatively agrees with the experiment.

Ideal ZZ or AC GNRs with perfect edges result in a constant conductance. In presence of edge disorder with one-atom steps on either only one edge (see Figure 4.6a1 and b1) or on both edges (see Figure 4.6c1 and d1), the conductance alternates between 0 and $\sim 2\,\mathrm{e}^2/\mathrm{h}$ whenever the np-interface sweeps across a single atom step for both ZZ (panel a2) and AC (panel b2) edges with zero bulk disorder. Stronger edge disorder with more

frequent steps at the edges results in a correspondingly higher frequency of oscillation of the conductance, see Figure 4.6c2 and d2. When a realistic *bulk* disorder of 35 meV strength is added (extracted from the experiment based on the width of the Dirac peaks), the oscillations in the ZZ case collapse to a roughly constant conductance of $\sim 0.5\,e^2/h$, while the conductance in the AC case remains strongly oscillating. Both of these behaviors are not consistent with the experiment. A ribbon which follows the ZZ direction with disorder in form of AC-30° segments shows oscillations in the simulations which are relatively robust against bulk disorder and which look qualitatively similar to the ones found in experiment (see Figure 4.5g and Figure 4.6d2). Hence, these findings are in agreement with AFM data indicating edges along the ZZ direction and are also in agreement with the Raman results presented above, i.e. graphene edges on hBN created by remote H plasma exposure follow the ZZ direction but contain significant edge disorder in form of AC-30° segments.

4.3.7 Electronic Transport Through H Plasma Defined Constrictions

In Figure 4.7, we show transport measurements for narrower and shorter graphene constrictions fabricated in a different way. Prior to encapsulation, we define two round holes of small diameter into the graphene layer with Ar/O_2 plasma and expose these to the remote H plasma to create hexagons sandwiching a GNR with ZZ edges between them, see Figure 4.7b. Here, the round seed hole is relatively small, only about 100 nm in size, and most of the $\sim$ 500 nm hexagon was etched with the H plasma process in an exposure of about 5 hours. For the Fabry-Pérot sample, in contrast, only a relatively small amount of H plasma etching was performed (about 1 hour), enlarging the Ar/O_2 plasma defined structures only slightly. It would be interesting to compare in transport experiments ribbons with long and short H plasma exposure, even tough no time dependence of the edge quality was observed on the Raman samples (see Figure 4.3). It is plausible that longer exposure has a healing effect on the edge, such that it removes defects more efficiently and creates less disordered atomic arrangements.

Plus, for longer exposures the ribbon direction is solely determined by the graphene lattice since the etching starts from a round defect and evolves naturally to a hexagon with edges along the ZZ crystal axis. In the Fabry-Pérot sample (short exposure), a small misalignment between the overall ribbon direction and the ZZ crystal axis may remain after the H plasma etching. Also, the ebeam defined circles are clearly visible as an elevated region. Such regions are known to appear after H plasma exposure and have been observed in many samples [67]. However, further investigation is required to better understand these features.

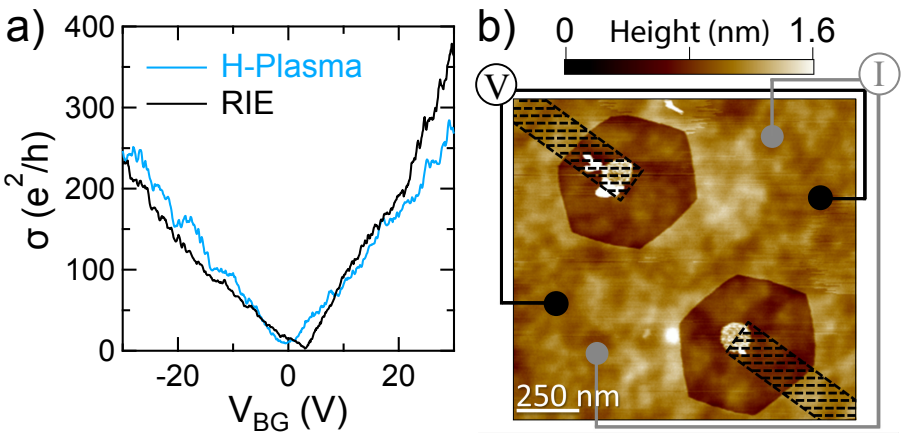

Figure 4.7: Comparison between H plasma and RIE ribbon. (a) Four-wire conductivity σ as a function of gate voltage for two GNRs etched in the same encapsulated sample, fabricated as labeled. A series resistance is subtracted from each curve, consistent with the the number of squares between the ribbon and the contacts ($\sim 200\,\Omega$ for blue and $\sim 400\,\Omega$ for black curve). (b) AFM height image of H plasma etched GNR with a width of $\sim 300\,$nm. Two Cr/Au edge contacts (not shown) are evaporated on each side of the ribbon after encapsulation and the black dashed regions are etched out to prevent short circuiting of the ribbon.

Figure 4.7 shows an example of such a ZZ GNR, with 4-wire conductivity as a function of global back gate voltage plotted in panel a, comparing a H plasma defined ribbon (blue) with a RIE defined ribbon (black). Both ribbons are fabricated on the same graphene flake, allowing direct comparison. As seen, the two curves are very similar, resulting in comparable mobilities, and no plateaus of quantized conductance are clearly evident. We note that for most of the gate voltage range the mean free path is larger than 500 nm in bulk, determined from a separate Hall bar sample, see SOM S6. Even tough the ribbons are about a factor of 2 shorter than the bulk mean free path,

conductance quantization is not observed. Thus, we conclude that the edges are the dominant source of scattering, irrespective of whether they are defined with H plasma or RIE. We note that none of the wiggles seen in these conductivity traces obviously develop into a conductance plateau even under application of a magnetic field.

4.4 Conclusion

In conclusion, we have found that H plasma defined hexagons on graphite did not show any D-peak intensity, and thus seem to display high quality ZZ edges. In contrast, in SL graphene on hBN, a relatively large D-peak is seen on H plasma defined edges. Polarization dependent Raman measurements revealed an edge configuration consisting of approximately 60 % ZZ and 40 % AC-30° segments. Valley-isospin oscillations in quantum transport are again consistent with edge disorder with 40 % AC-30° segments. Moreover, transport through narrow graphene constrictions showed similar mobilities for RIE defined edges and H plasma edges. Interestingly, bulk graphene shows high electronic quality after H plasma exposure, manifested in Fabry-Pérot resonances. Thus, exposure of graphene to the remote H plasma is an excellent cleaning method, since it removes residues very efficiently without degrading the quality of the graphene crystal lattice. This is further confirmed by Raman spectroscopy (no D-peak in the bulk), AFM (very clean surfaces without PMMA residues) and electronic transport measurements (high electronic mobility).

Further investigations are needed to identify possible origins of the disorder such as e.g. hBN-graphene interactions where the relative rotation angle could play a role [172, 199], or a too high thermal energy leading to edge reconstruction [117]. Thus, further optimization of the H plasma etching process is required in order to obtain high quality crystallographic graphene edges.

4.5 Methods

AFM specifications: Two different AFM instruments were used for the measurements presented in this work. The data shown in Figure 4.1a to c was obtained by means of ambient qPlus based atomically resolving AFM [189], namely with a quartz force sensor with resonance frequency $f_0 = 33\,\mathrm{kHz}$, stiffness $k = 1800\,\mathrm{N/m}$ and quality factor $Q = 3000$. Coarse topography images in Figure 4.1a and b were acquired in the frequency-modulated mode while Figure 4.1c shows an atomically resolved frequency shift image acquired in the constant height mode. The details of the setup are described elsewhere [200]. For all other AFM data a Bruker Dimension 3100 was used. All data measured with this instrument was acquired in intermittent contact mode (amplitude modulated).

H plasma parameters: The following parameters were used for the exposures of all samples presented in this work: $T = 400\,^{\circ}\mathrm{C}$, $p = 1.7\,\mathrm{mbar}$, H_2 gas flow of 20 SCCM. The details of the setup are described elsewhere [67].

Raman microscope: The Raman measurements were acquired with a WITEC alpha300 Raman system. The wavelength of the He-Ne laser was 633 nm and the used objective was 100x with $NA = 0.9$. The laser power was set to 1.5 mW or below for all measurements. This power is low enough to exclude any laser induced structural changes (see SOM S2). To extract the peak heights, we first subtract the background and fit single Lorentzains (for the G and 2D-peaks) and a double Lorentzian for the D and hBN peaks.

Sample fabrication: We used graphite flakes from NGS Naturgraphit GmbH. SL flakes were obtained by the scotch tape method [21] and transferred on top of hBN crystals by the wet transfer technique described in ref. [127]. High quality hBN crystals [174] were exfoliated on top of a p++ doped Si wafer covered by 300 nm SiO_2 following the same scotch tape method. For the sample in Figure 4.7, we used an hBN flake from HQ-Graphene. After H plasma etching, the electronic transport samples were in

addition encapsulated by a top hBN flake to ensure high cleanliness and stability of the devices. To cut the hBN/graphene/hBN stack in order to shape it or define control ribbons an $SF_6/Ar/O_2$ gas mixture was used in an RIE process. Cr/Au side-contacts were fabricated following ref. [129] with an additional RIE step with CHF_3/O_2 gas prior to metalization. The GNR presented in Figure 4.5 is 600 nm wide and measures 1.6 μm in length between the source and drain contacts. The bottom and top hBN layers have a thickness of 42 nm and approx. 35 nm, respectively.

Electronic transport measurements: Standard low frequency lock-in measurements were performed in a variable temperature insert at $T = 4\,\mathrm{K}$.

Quantum transport simulations: All quantum transport simulations are done with the following parameters. Magnetic field is fixed at $B = 16\,\mathrm{T}$, the distance between two *pn*-interfaces is set to 20 nm, the ribbon is about 40 nm wide, and the smoothness of the *pn* and *np* regions is approximately 5 nm. Device scaling is necessary due to computational capacity reasons and the strong magnetic field is required to ensure that the Landau levels are well developed in such a narrow ribbon. All calculations with disorder are averaged over 200 different configurations of Anderson-type disorder potential. All calculations are done at zero temperature.

4.6 Acknowledgments

We would like to thank J. Roche, C. Handschin and J. Overbeck for technical advice and helpful discussions. We acknowledge support from the Swiss Nanoscience Institute (SNI), NCCR QSIT, Swiss NSF, Taiwan Minister of Science and Technology (MOST), Grant No. 107-2112-M-006 -004 -MY3 and financial support from Innosuisse. We also thank Korbinian Pürckhauer, Anja Merkel, Florian Griesbeck and the machine shop of U Regensburg for building, assembling and testing the ambient qPlus based atomically resolving AFM and the Deutsche Forschungsgemeinschaft for funding under GRK 1570. Growth of hexagonal boron nitride crystals was supported by the Elemental Strategy Initiative conducted by the MEXT, Japan and the CREST (JPMJCR15F3), JST.

4.7 Supplementary Information

4.7.1 S1 High Quality Bulk Graphene after Hydrogen Plasma Exposure

In order to investigate the influence of remote hydrogen (H) plasma exposure on the graphene flake, we recorded Raman maps (see Figure 4.8). In panel a) and b) we show the integrated 2D- and D-peak intensities, respectively. It is nicely visible, that the D-peak intensity is only high at the edges of the flake and the hexagons and very low in the bulk, showing that exposure of graphene to remote H plasma only edges from defects and the edges and leaves the bulk intact. Furthermore, we can exclude hydrogenation of bulk graphene because this would lead to D-peak intensity [114]. Panel c) shows an AFM height image of the region where the Raman maps in a) and b) were recorded. The green, red and purple crosses are drawn at the same location on the flake through a) - c), namely the green cross lays inside the hexagon, the red cross at the edge and the purple cross on bulk graphene.

Raman spectra were recorded at the location of these crosses and are shown in panel d) with the corresponding color coding. We observe the graphene related D-, G-, and 2D-peaks, as well as the hBN-peak coming from the substrate. Looking at the G- and 2D-peaks, the intensity is highest for the measurement on bulk graphene, decreases to about half the intensity for the measurement at the hexagon edge and almost vanishes for the measurement taken inside the hexagon. Since the laser spot size is on the order of the hexagon size, the G- and 2D-peak intensities do not fully vanish because the tails of the Gaussian beam shape still excite a small fraction of graphene. Interestingly, the D-peak intensity is only high for the measurement taken at the edge and zero inside and outside the hexagon (see panel e) for the zoom-in). This shows, that the rim initially created when the starting defect was fabricated by reactive ion etching (RIE) in an Ar/O_2 plasma does not contribute to the graphene D-band in the Raman spectrum. In Figure 4.8 f) we show the intensity profile of the 2D-peak, recorded along the red solid line in panel a). From this profile we extract a laser spot diameter of $\sim 860\,\text{nm}$. This

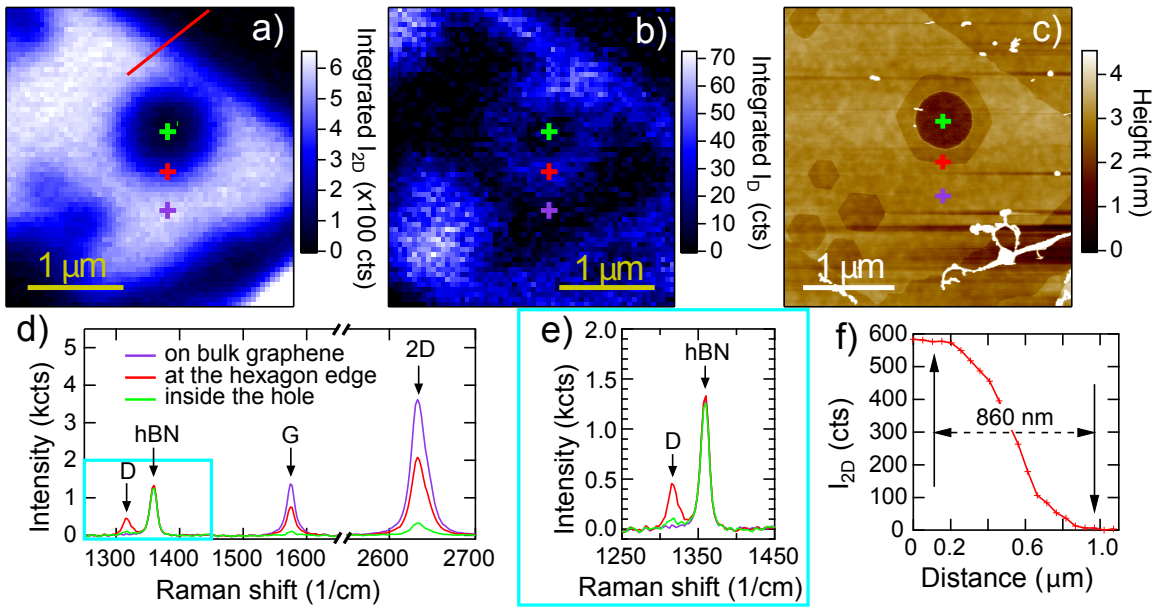

Figure 4.8: High quality bulk graphene after H plasma exposure Integrated 2D-intensity (a)) and integrated D-peak intensity (b)) of a section of a single layer (SL) graphene flake on a hexagonal boron nitride (hBN) substrate after 4 h of H plasma exposure. c) AFM height image of the region where the Raman maps in a) and b) were recorded. d) Raman spectra recorded at the locations indicated by the colored crosses in a) - c). e) Zoom-in on the region of the D-peak. f) 2D-peak intensity as a function of distance measured along the red solid line in panel a).

is well in agreement with the theoretically expected diffraction-limited spot diameter ($1.22{*}\lambda/NA = 858$ nm, with the numerical aperture $NA = 0.9$ and the laser wavelength $\lambda = 633$ nm).

4.7.2 S2 Laser Power Test

A crucial condition for the investigation of the edge constitution by means of Raman spectroscopy is that the edge is not changed upon laser irradiation. Indeed it has been observed experimentally [184] that edge reconstruction due to laser annealing can happen at graphene edges. To ensure, that our graphene edges are not altered upon laser irradiation we performed a laser power test. In Figure 4.9 a) we show an AFM height image of the sample on which we performed the laser power test. In panel b) we plot the normalized D-peak intensities measured at different stages of the laser power test (measurement # 1 to 5).

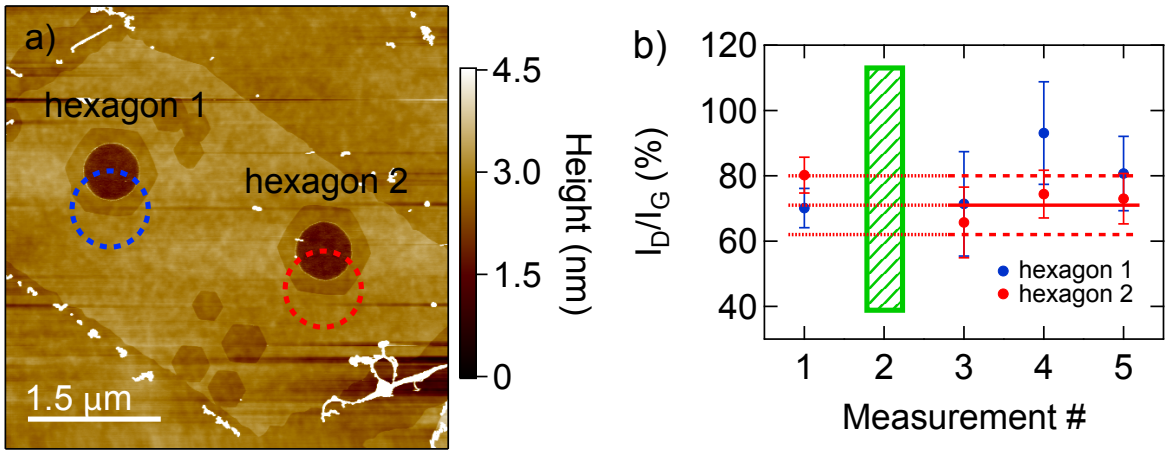

Figure 4.9: Laser power test a) AFM height image of a SL graphene flake on hBN after 4 h of remote H plasma exposure. The blue and red dashed circles indicate the laser spot where the Raman spectra shown in panel b) were recorded. b) Normalized D-peak intensity recorded at different stages of the laser power test. Measurement # 1, 3, 4 and 5 were acquired with a laser power of 0.5 mW. Only hexagon 2 was exposed to a laser power of 1.5 mW, see measurement # 2 (green dashed area indicates exposure to 1.5 mW). The red solid and dashed lines at measurement # 3 to 5 indicate the average and the standard deviations, respectively. They are prolonged to the left across measurement # 1 and 2 and show that the normalized D-peak intensities recorded before and after exposure to 1.5 mW are comparable. All data points are averages over five measurements and the error bars are the corresponding standard deviations.

First we measured at both hexagons with a laser power of 0.5 mW (measurement # 1). In a second step we expose hexagon 2 five times, each time for 1 min, to a laser power of 1.5 mW (measurement # 2). After this exposure to 1.5 mW we measure again at both hexagons with 0.5 mW (measurement # 3 to 5). Comparing the normalized D-peak intensities recorded before exposure to 1.5 mW (measurement # 1) with the intensities recorded afterwards (measurement # 3 to 5), it is indicated that measuring with a laser power of 1.5 mW does not change the recorded D-peak intensity significantly and hence the edge is not impaired. Hence we generally measured with a laser power of 1.5 mW to have a reasonable signal to noise ratio.

4.7.3 S3 Extraction of the Cavity Length

In order to characterize the electronic quality of our H plasma exposed graphene samples, we extract a lower bound for the mean free path l_{mfp} of the charge carriers from

the oscillation period of the Fabry-Pérot oscillations which are only visible if l_{mfp} exceeds the cavity length L. In particular, L can be calculated from the charge carrier density values n of two consecutive oscillations:

$$L = \frac{\sqrt{\pi}}{\sqrt{n_{j+1}} - \sqrt{n_j}} \tag{4.1}$$

In Figure 4.10 we present electronic transport data recorded on the sample presented in Figure 4.5 in the main manuscript. Panel a) shows the conductance as a function of the inner (n_{in}) and outer (n_{out}) densities, where n_{in} is the density in the top gated area and n_{out} is the density in the graphene which is only influenced by the global back gate.

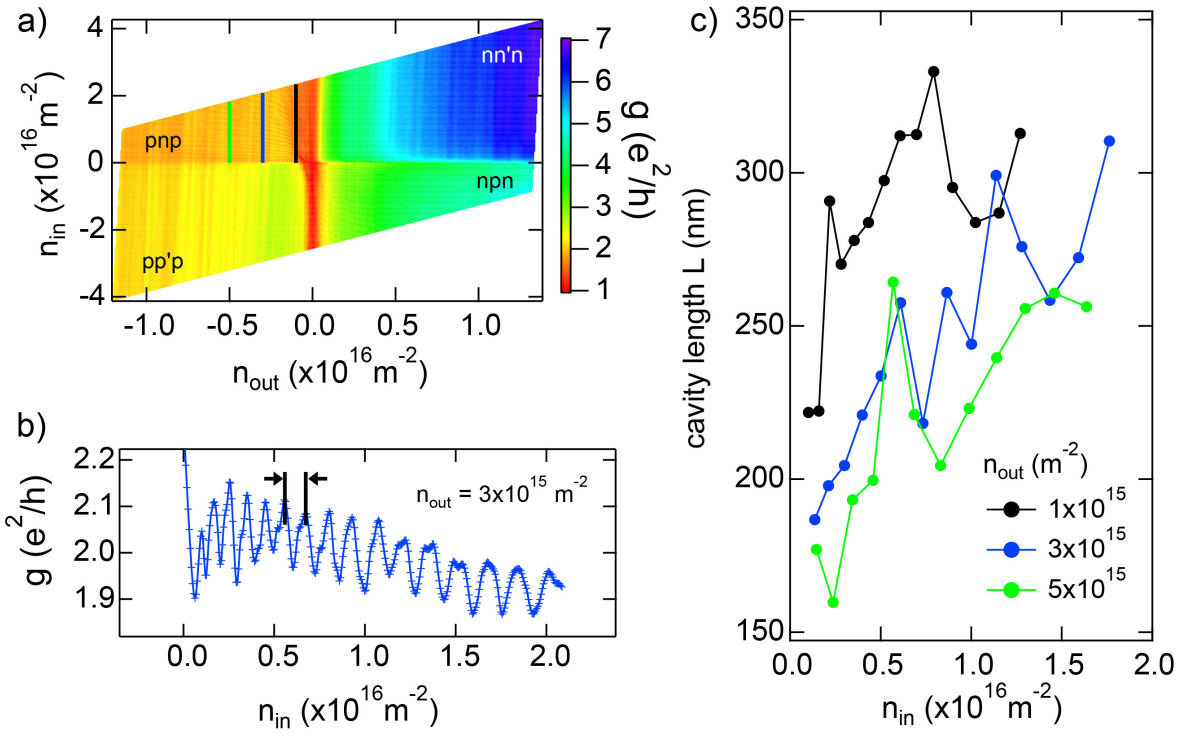

Figure 4.10: Extraction of the cavity length a) conductance as a function of n_{in} and n_{out}. b) cut along the blue solid line in a). Fabry-Pérot resonances are visible indicating ballistic transport between the pn-interfaces. c) Extracted cavity lengths L as a function of n_{in} for three different values of n_{out}.

The conductance map can be divided into four regimes: pnp, pp'p, npn and nn'n. In the two bipolar regimes (pnp and npn) pn-junctions are formed which build a cavity

for the charge carriers and lead to Fabry-Pérot resonances (see panel b) for a cut along the blue line in a)). Using Equation4.1 we extract values for L at different n_{out}, see panel c). The largest cavity sizes are reached for low values of n_{out} and large values of n_{in}. In particular, the values for L lay in the range of 160 nm to 330 nm.

4.7.4 S4 Edge Reconstruction

Reconstruction of zigzag (ZZ) edges has been observed experimentally [117, 201] and predicted theoretically [192]. Among them, Xu et al. [117] proposed a reconstruction mechanism which leads to four types of edge reconstructions and has the following form:

$$I_D \propto \frac{1}{4}f1 + f2 + \frac{1}{2}f1cos^2(\theta - \phi) \tag{4.2}$$

where f_1 describes the relative weight of armchair (AC)-30° segments, f_2 are the point defects, f_3 are the ZZ-0° segments and f_4 are the ZZ-60° weights. θ denotes the polarization angle with respect to the edge and ϕ is an offset which could stem from an alignment error. Since only AC-30° segments and point defects are D-peak active, it is possible to learn about their relative abundance (f_1/f_2) by performing polarized Raman experiments. In Figure 4.11 a) we plot the normalized D-peak intensity as a function of θ which was measured at the edge of the hexagon shown in Figure 4.4 a) in the main manuscript. The blue curve is a fit to Equation 4.2 from which we extract values for f_1 and f_2. The extracted values indicate that AC-30° segments are much more abundant than point defects and hence that the edge essentially consists only of AC-30° and ZZ segments.

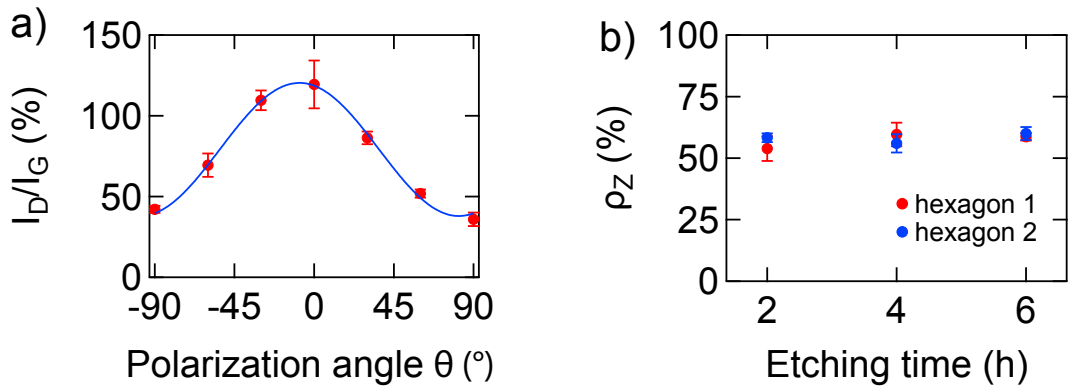

Figure 4.11: Edge reconstruction. a) Normalized D-peak intensity as a function of the polarization angle θ for the hexagon shown in Figure 4.4 a) of the main manuscript. The blue curve is a fit to Equation 4.2 yielding $f_1 = 165 \pm 6$, $f_2 = -3 \pm 3$ and $\phi = -8 \pm 1$. b) ρ_Z as a function of etching time for two different hexagon edges.

In Figure 4.11 b) we plot the ratio of ZZ to AC-30° segments ρ_Z extracted at different stages of the etching process for two different hexagon edges. The extraction of ρ_Z was done following the procedure presented in ref. [107] as also described in the main manuscript. Within the experimental error bars ρ_Z is similar for all investigated etching times.

4.7.5 S5 Effect of the Hole Shape on the D-peak Intensity

As complementary to the discussion of the etching series presented in Figure 4.3 of the main manuscript, the geometrical change from the circular hole to the hexagonal hole must be taken into account in order to interpret the increase of the D-peak intensity correctly. Typically, a change in edge length effects the D-peak intensity and a change in the graphene area enclosed in the laser spot effects the G-peak intensity. These shape changes must be normalized such that I_D/I_G only manifests the edge quality.

First, we look at the change of the shape from the RIE circular hole to the H plasma etched hexagonal hole. The total edge length enclosed in the laser spot for both shapes are almost equal to each other ($\sim$ 940 nm). But for the total D-peak intensity, it is crucial to consider the polarization direction of the light with respect to the orientation of the edge and the Gaussian intensity profile of the laser spot. We calculate an effective

D-peak intensity by assuming that every point at the edge allows the second order scattering process which is responsible for the D-peak signal. This assumption assures that the following calculation only represents the geometrical changes from a circular shape to a hexagonal shape. When the laser spot is positioned as seen in Figure 4.12,the D-peak intensity in a single spectrum measurement is given by:

$$I_D \approx \int\int d\beta dr P(\beta)\cos^2(\theta+\beta)I(\vec{r}). \tag{4.3}$$

The polarization function, $P(\beta)$, determines the laser power at an angle β with respect to the horizontal axis, shown in Figure 4.12. For linear polarization, this function is maximum at the polarization angle and zero at 90 degrees from the polarization angle. For general elliptical polarizations, the function is written explicitly in Equation 4.4, describing laser power for each angle in our single spectrum measurements:

$$|\vec{P}(\beta)| = P(\beta) = \sqrt{(2.5\cos\beta)^2 + \sin^2(\beta)}. \tag{4.4}$$

The coefficient (2.5) describes how much the polarization is deviated from a perfect circular polarization due to an asymmetry at the beam splitter. For the circular polarization, β is integrated from 0 to π. The second function $I(\vec{r})$ describes the Gaussian beam shape:

$$I(\vec{r}) = I_0 e^{-2\frac{r^2}{\omega_0^2}} \tag{4.5}$$

with $\vec{r}$ being the radial distance from the center of the laser spot to the respective point at the edge and ω_0 being the (Gaussian) beam waist, measured and calculated to be 430 nm. The third part is the cosine squared function which is a correction due to that the D-peak intensity is maximum (minimum) when the polarization direction is parallel (perpendicular) to the edge direction. The argument of this function is the sum of the polarization angle β and the angle θ of the tangent line with respect to the

horizontal axis, as shown in Figure 4.12.

In order to calculate the effective D-peak intensity at the RIE hole, we apply this integral onto the circumference of the circular hole that fits inside the laser spot, as drawn in Figure 4.12. For ease-of-calculation, the full circular shape is approximated as a 60-edge-polygon which has an imperceptible effect on the calculation. It should also be noted that for the calculation with the right integral limits, the integral in Equation 4.3 is converted into a line integral which runs along the circumference enclosed by the laser spot.

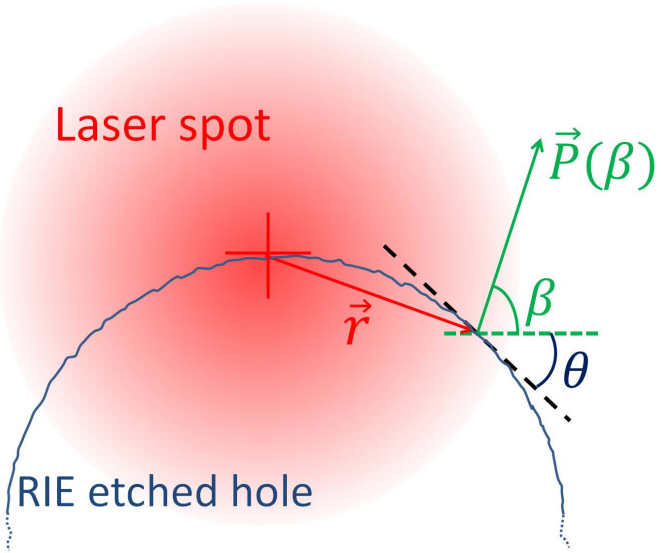

Figure 4.12: Schematic for the integral in Equation 4.3 In a single spectrum measurement, the center of the laser spot is located at the circumference. For any point along the edge, the distance from the center of the laser spot is defined as $\vec{r}$. The polarization vector $\vec{P}(\beta)$, is defined with angle β with respect to the horizontal axis (green dashed line). The orientation of the edge, which is the tangent line at that point, is also defined with respect to the horizontal axis with angle θ.

Secondly, we calculate the effective D-peak intensity for the hexagonal hole. This calculation is easier than the circular case since it includes only 3 edge segments with angles of 0 and ± 60 degrees. The lengths of the hexagonal hole edges are measured on AFM images and all the dimensions of the holes and the D-peak intensity calculations are given in Table 1.

Then we calculate the graphene area enclosed in the laser spot. Obviously, the graphene area enclosed in the laser spot changes from circular to hexagonal hole. Since we locate the center of the laser spot at the center of the top or bottom edge, half of the laser spot always covers the same graphene area but only the side pieces around the hole are different after each etching step. At this point, we calculate the area by using simple geometry and write the result again in Table 1. As you can see the change in area is at most 14 %. In this calculation, we assume that the G-peak intensity is only proportional to the area of graphene enclosed in the laser spot and we do not consider the Gaussian intensity profile. In fact, the effect of these side areas on the G-peak intensity is much less than the calculated values since they are further away from the center.

The resulting I_D/I_G ratios are given in Table 1. All the values in the table are normalized to the value for the RIE hole of the corresponding quantity. As a result, the top row (RIE hole values) is always equal to 1 and the values for 2h etching and 4h etching show the relative change from the RIE case. Apparently, the calculated I_D/I_G due to the geometrical change of the edge length and the area (rightmost column) does not correspond to the measured values of I_D/I_G in the main text. This means that the increase of the I_D/I_G values from the RIE hole to the H plasma etched hole is not due to that the edge is longer or the graphene area is less but it is due to a change in the atomic configuration at the edge. In other words, compared to an RIE etched edge of the same length, an H plasma etched edge has more AC edge segments contributing to the D-peak signal.

Etching (x)	Total edge length inside ω_0	Calculated I_D^x/I_D^{RIE}	Area inside ω_0 $\approx I_G^x/I_G^{RIE}$	Measured I_D^x/I_G^x (main text)	Calculated I_D^x/I_G^x (geometry)
RIE	$\sim 940nm$	1	1	1	1
2h H-plasma	$\sim 945nm$	1.03	0.89	2.4	1.16
4h H-plasma	$\sim 950nm$	1.04	0.86	2.4	1.21

Table 1: Calculations for the 600 nm hole with circularly polarized light

4.7.6 S6 Electronic Mobility of Encapsulated Hall Bar

In this section we present transport data recorded on a SL graphene Hall bar encapsulated between two hBN flakes. In particular we are interested in the cleanliness of the encapsulated graphene and extract the mean free path l_{mfp} of the charge carriers to compare it with relevant length scales of the investigated graphene nano ribbon (GNR) devices discussed in the main manuscript (Figure 4.7). In Figure 4.13 a) an optical microscopy image of the encapsulated Hall bar is shown with the electronic circuit drawn on top of it. In panel b) the conductivity σ as a function of the charge carrier density n is plotted. The blue and green curves are fits to the following equation:

$$\sigma(n) = \left(\frac{1}{\mu n e} + \rho_s \right)^{-1} \tag{4.6}$$

where μ is the mobility, e the electronic charge and ρ_s a series resistivity which is composed of the contact resistances and the cryostat lead resistances. The fit to the electron side (green curve) gives $\mu = 134'000\,\mathrm{cm}^2/\mathrm{Vs}$ and the fit to the hole side (blue curve) gives $\mu = 114'000\,\mathrm{cm}^2/\mathrm{Vs}$. In panel c) we plot σ as a function of n on a log-log scale. By looking at the position of the kink, indicated by the black solid and dashed lines, we extract an estimate of the residual disorder density which is $3 \cdot 10^{10}\,\mathrm{cm}^{-2}$. Further, we calculate l_{mfp} of the charge carriers for the electron side by using the following formula:

$$l_{mfp}(\mu, n) = \frac{\hbar}{e} \cdot \mu \cdot \sqrt{\pi n} \tag{4.7}$$

where $\hbar$ is the Planck constant.

The mean free path reaches $1\,\mu$m at $n = 4.1 \cdot 10^{11}\,\mathrm{cm}^{-2}$ which clearly exceeds all relevant length scales in the GNR devices discussed in the main manuscript (Figure 4.7).

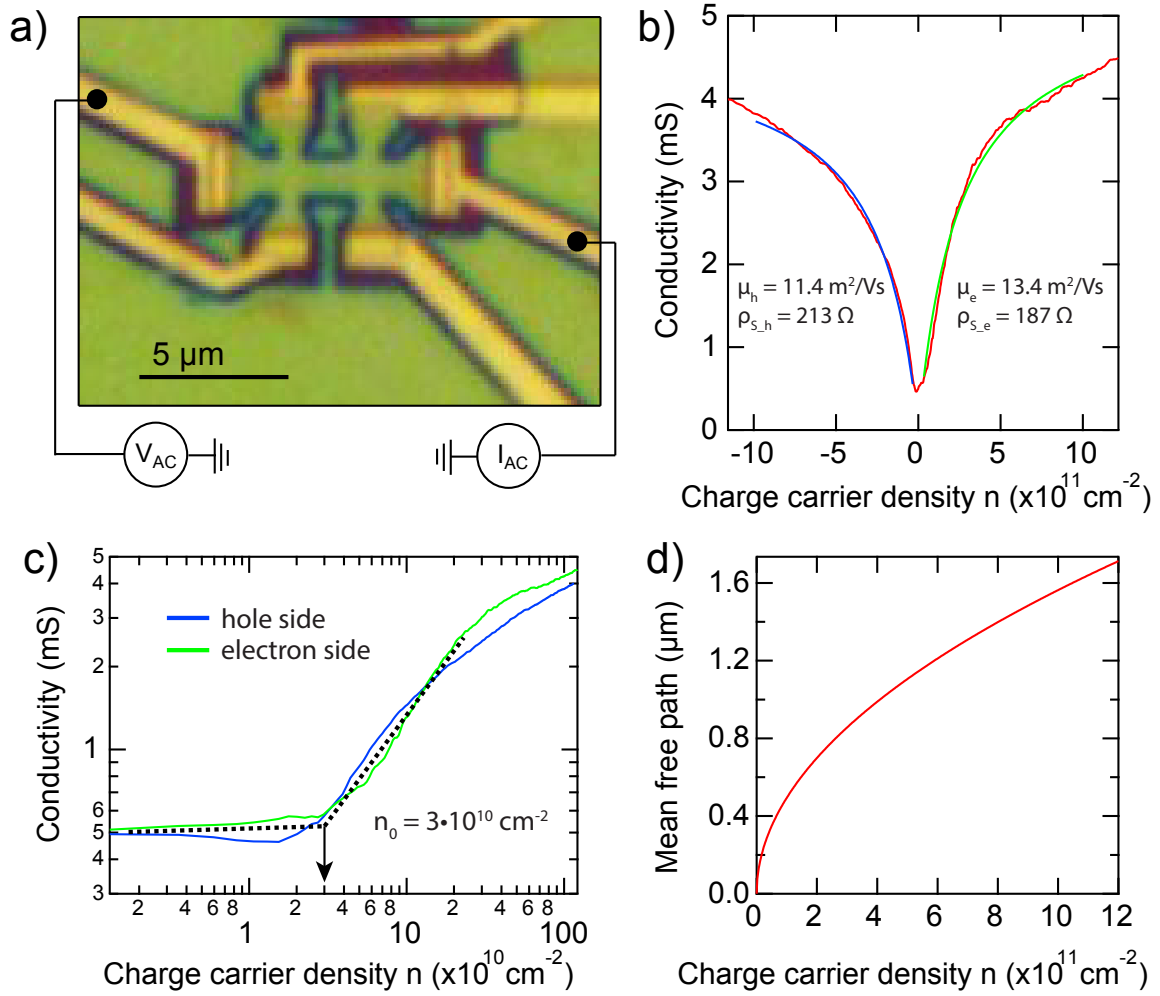

Figure 4.13: Mobility of an Encapsulated Hall Bar a) Optical microscopy image of the investigated SL graphene Hall bar encapsulated between two hBN flakes. The side contacts are yellow and the electronic circuit is indicated. b) Conductivity as a function of the charge carrier density. The green and blue curves are fits to Equation 4.6. The following fitting parameters were obtained: electron side, $\mu_e = 1.34 \cdot 10^5 \pm 1 \cdot 10^3\,\mathrm{cm}^2/\mathrm{Vs}$, $\rho_{S\_e} = 187 \pm 1\,\Omega$; hole side: $\mu_h = 1.14 \cdot 10^5 \pm 1 \cdot 10^3\,\mathrm{cm}^2/\mathrm{Vs}$, $\rho_{S\_h} = 213 \pm 1\,\Omega$. c) Conductivity as a function of the absolute value of the charge carrier density plotted in a log-log representation. The location of the kink gives the estimate of the residual disorder density n_0 which is $3 \cdot 10^{10}\,\mathrm{cm}^{-2}$. d) Mean free path as a function of the charge carrier density for the mobility value obtained for the electron side.

4.7.7 S7 Comparison of the Experiment with the Simulation

In this section, the differences between the experimentally measured conductance $g(\Delta x_{\text{np-exp}})$ and the simulated conductance $g(\Delta x_{\text{np-sim}})$ are discussed. In the experiment, the positions of the two pn-interfaces can be tuned with gate voltages applied

to the local top gate and the global back gate. Thereby, the pn-interfaces move always in opposite directions, i.e. either towards each other or apart from each other, see Figure 4.14 a). In the simulation, on the other hand, the two pn-interfaces move always in the same direction, see Figure 4.14 b).

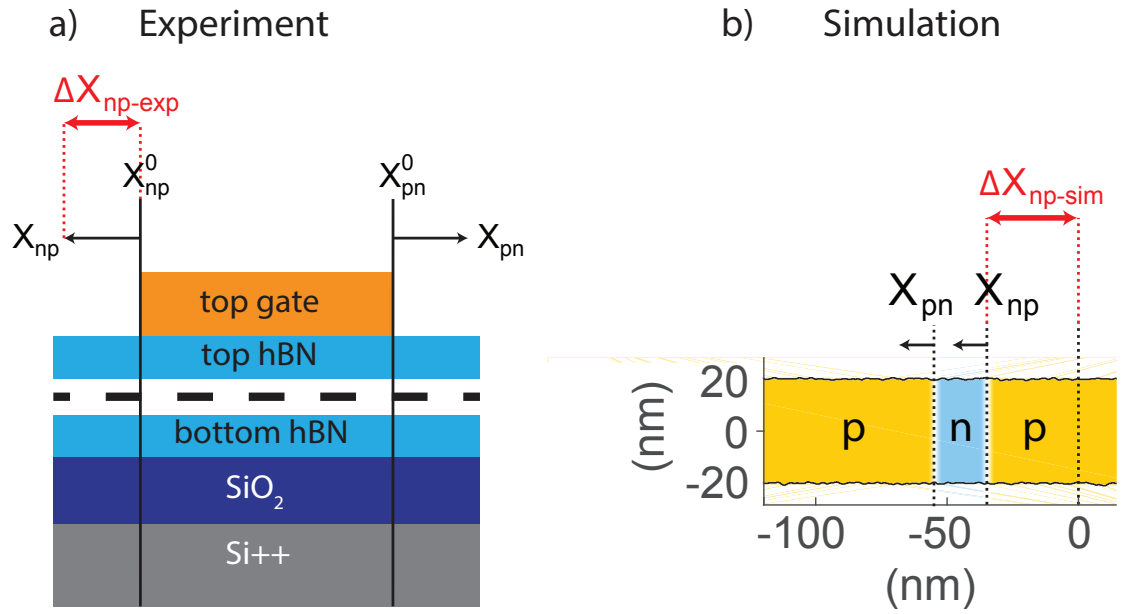

Figure 4.14: Experiment vs Simulation a) Schematic of the cross section of the device on which transport was measured. b) Model which was used for the simulations.

This is equivalent to connecting an *np* junction with conductance $G(x_{\mathrm{np}})$ and a *pn* junction with conductance $G(x_{\mathrm{pn}})$ in series, and then move the two junctions together in the same direction. Specifically, we are comparing our simulations for

$$g(\Delta x_{\text{np-sim}}) = g(x_{\mathrm{np}}) \propto G(x_{\mathrm{pn}})G(x_{\mathrm{np}})$$

with the experimentally measured

$$g(\Delta x_{\text{np-exp}}) = g(x_{\mathrm{np}} - x^0_{\mathrm{np}}) \propto G(x_{\mathrm{np}} - x^0_{\mathrm{np}})G(x_{\mathrm{pn}} - x^0_{\mathrm{pn}}) \ ,$$

where $x^0_{\mathrm{np}} = -100\,\mathrm{nm}$ and $x^0_{\mathrm{pn}} = 100\,\mathrm{nm}$ are the designed positions of the two edges of the top gate, and $x_{\mathrm{pn}} = -x_{\mathrm{np}}$ due to their opposite movement. Despite this subtle difference, the comparison makes reasonably good sense because the AC-30° segments

of the edge disorder are randomly located. That is, in the simulation, $G(x_{\mathrm{pn}})$ is expected to be uncorrelated with $G(x_{\mathrm{np}})$, just like in the experiment, $G(x_{\mathrm{np}} - x^0_{\mathrm{np}})$ is expected to be uncorrelated with $G(x_{\mathrm{pn}} - x^0_{\mathrm{pn}})$, either. Hence, $g(\Delta x_{\text{np-exp}}) \sim g(\Delta x_{\text{np-sim}})$ and therefore we introduce the parameter Δx_{np} for both, experiment and simulation, as used in the main paper in Figure 4.5 and Figure 4.6.

4.7.8 S8 Conversion of Backgate Voltage to the pn-interface Location

In order to interpret the valley-isospin oscillations in terms of the pn-interface locations it is necessary to convert gate voltages to the actual pn-interface locations. In Figure 4.15 a) a calculation of the electrostatics of the studied device is shown where the pn-interface position relative to the left edge of the top gate ΔX_{np} is plotted as a function of back gate and top gate voltages. In panel b) a cut along the red solid line in a) is shown. This curve was used to convert back gate voltage to ΔX_{np} for the curves presented in the main manuscript.

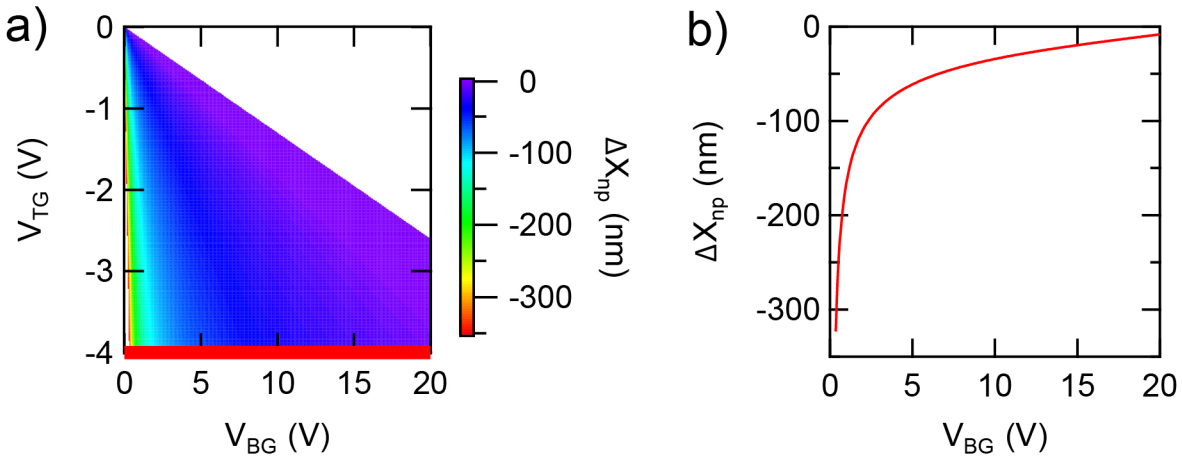

Figure 4.15: Conversion of Backgate Voltage to the pn-interface Location a) Electrostatic simulation of the device presented in Figure 4.5 in the main manuscript where the pn-interface location relative to the left edge of the top gate ΔX_{np} is plotted as function of top and back gate voltages. b) Cut along the red solid line in a).

5 Single, Double, and Triple Quantum Dots in Ge/Si Nanowires

F. N. M. Froning, M. K. Rehmann, D. M. Zumbühl and F. R. Braakman

Department of Physics, University of Basel, CH-4056 Basel, Switzerland

J. Ridderbos, M. Brauns, F. A. Zwanenburg

NanoElectronics Group, MESA+ Institute for Nanotechnology, University of Twente, P.O. Box 217,7500 AE Enschede, The Netherlands

A. Li, E. P. A. M. Bakkers

Department of Applied Physics, Eindhoven University of Technology, P.O. Box 513, 5600 MB Eindhoven, The Netherlands

Abstract

We report highly tunable control of holes in Ge/Si core/shell nanowires. We demonstrate the ability to create single quantum dots of various sizes, with low hole occupation numbers and clearly observable excited states. For the smallest dot size we observe indications of single-hole occupation. Moreover, we create double and triple tunnel-coupled quantum dot arrays. In the double quantum dot configuration we observe Pauli spin blockade (PSB). These results open the way to perform hole spin qubit experiments in these devices.

This chapter was published in *Applied Physics Letters* **113**, 073102 (2018).

5.1 Motivation

Single hole spins confined in quantum dots (QDs) in Ge/Si core/shell nanowires (NWs) combine several advantageous properties which makes them potentially very powerful quantum bits [6, 202]. The natural abundance of non-zero nuclear spins in both silicon and germanium is relatively small and can be further reduced to a negligible amount by isotopic purification. Furthermore, hole spins have no contact hyperfine interaction due to their p-type wavefunction. These properties make hole spin qubits in silicon and germanium resilient against dephasing via interaction with nuclear spins.

A particularly promising feature of hole spins in Ge/Si core/shell NWs is the nature of spin-orbit interaction (SOI) in this system. Confinement to one dimension gives rise to an effective SOI in the valence band, which is predicted to be both strong and tunable [13, 203], enabling fast all-electrical spin manipulation. An external electric field can be used to set the strength of this SOI. This promises the capability of electrical gating of the SOI, allowing to switch to a large SOI for high interaction strengths and fast quantum operations, or to turn off SOI for increased qubit coherence. Furthermore, this SOI results in a Landé g-factor that is locally tunable by external electric as well as magnetic fields [14, 15]. Local control over the g-factor makes it possible to selectively address individual spin qubits and allows for selective coupling to microwave cavities [132].

The confinement of single holes in QDs is an important step towards implementation of the basic ingredients of experimental quantum computation using hole spin qubits [6]. Single QDs form the fundamental building blocks, and it is therefore imperative to be able to reliably form and characterize them [141]. Moreover, a high level of control over the exact position and shape of individual QDs is required to accurately tune level splittings [13], spin relaxation times [147, 204], and tunnel coupling strengths.

In addition to single QDs, tunnel-coupled double QDs are of particular interest, since these are platforms for spin-to-charge conversion schemes facilitating spin read-out and coupling of spins to microwave cavities [205–207]. Spin states of double and triple QDs can be used as qubit encodings which are insensitive to fluctuations of a uniform magnetic field or of magnetic field gradients [208, 209]. Moreover, quantum operations on these qubits may be performed using different mechanisms than for single spin qubits, for instance only relying on the Heisenberg exchange interaction [210, 211]. Finally, double as well as triple QDs feature charge states with an increased dipole moment, potentially leading to enhanced coupling strengths of spin qubits to microwave cavities [207].

5.2 Main Experimental Findings

In this Letter, we demonstrate a large amount of control over the formation of single, double and triple QDs in Ge/Si NWs, all with a low hole occupation number. Using five bottom gate electrodes, we tune the size and position of single QDs defined in the NW. Furthermore, we form tunnel-coupled double and triple QDs. In the double QD configuration, we observe Pauli spin blockade [147, 151] (PSB).

5.3 Sample Design

We use a Ge/Si NW [130] with an estimated Ge core radius of 10 nm and Si shell thickness of 2.5 nm (see Fig. 5.1). Five Ti/Pd bottom gate electrodes are lithographically defined on a p++-doped Si substrate covered with 290 nm thermal oxide. The bottom gates have a thickness of ∼15 nm, a width of 20 nm, and are equally spaced with a pitch of 50 nm. On either side of these gates, a plateau gate (green in Fig. 5.1 b) is defined, which serves to prevent bending of the NW. The bottom gates are subsequently covered by a layer of Al_2O_3 of thickness 20 nm through atomic layer deposition at 225 °C. In a next step, the NW is placed deterministically on top of the bottom gates using

a micromanipulator setup. Electrical contact to the NW is made through two Ti/Pd (∼0.5/60 nm) contact pads, which are lithographically defined and metallized after a brief HF dip to strip the NWs native oxide.

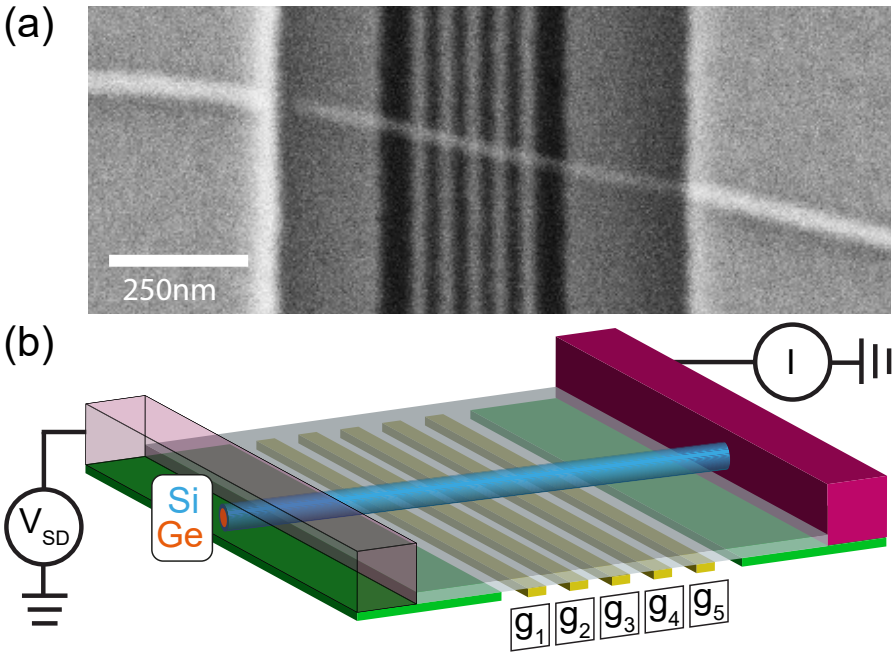

Figure 5.1: (a). Scanning electron micrograph of a device similar to the one used in this work. (b) Schematic overview of device and measurement setup. The NW is shown in blue, with the core in orange, bottom gates are in yellow and green, and contacts in purple.

Due to the type-II staggered band alignment of silicon and germanium, a hole gas accumulates in the core [131]. By applying positive voltages to the gate electrodes, the hole density can be depleted locally, resulting in the formation of QDs. We perform transport measurements by applying a dc source-drain bias V_{SD} over the NW and measuring the differential conductance using standard lock-in techniques with a small ac excitation in the range of 20-100 μV applied to the source contact. All measurements were performed at a temperature of 1.4 K, without application of an external magnetic field, and with the doped part of the substrate grounded.

5.4 Single QDs of Different Sizes

Figure 5.2 a gives an overview of the different configurations of biased gates and dot sizes that were studied. QDs can be formed using two, three, four or five neighboring gates. For each dot size, the outer two gates (red in Fig. 5.2 a) form tunnel barriers between the QD and the source and drain reservoirs. The voltage on individual or multiple middle gates (green in Fig. 5.2 a) are used to tune the electrochemical potential of the QD. Unused gates (white in Fig. 5.2 a) are grounded. In Figure 5.2 b and c, measured charge stability diagrams (Coulomb diamonds) are shown for the case of a single QD formed by two and three neighboring gates, respectively (see Fig. 5.2 a, top panels). Similar measurements were made for larger QDs formed by four and five gates. In case of the QD defined by two adjacent gates, we find that sweeping the voltage on these gates has a large effect on the tunnel barriers defining the dot. As a result, only a few charge transitions can be observed for this configuration. For the other dot sizes, the tunnel barriers are much less affected by the voltage on one of the middle gates, and we observe a large number of regular Coulomb diamonds.

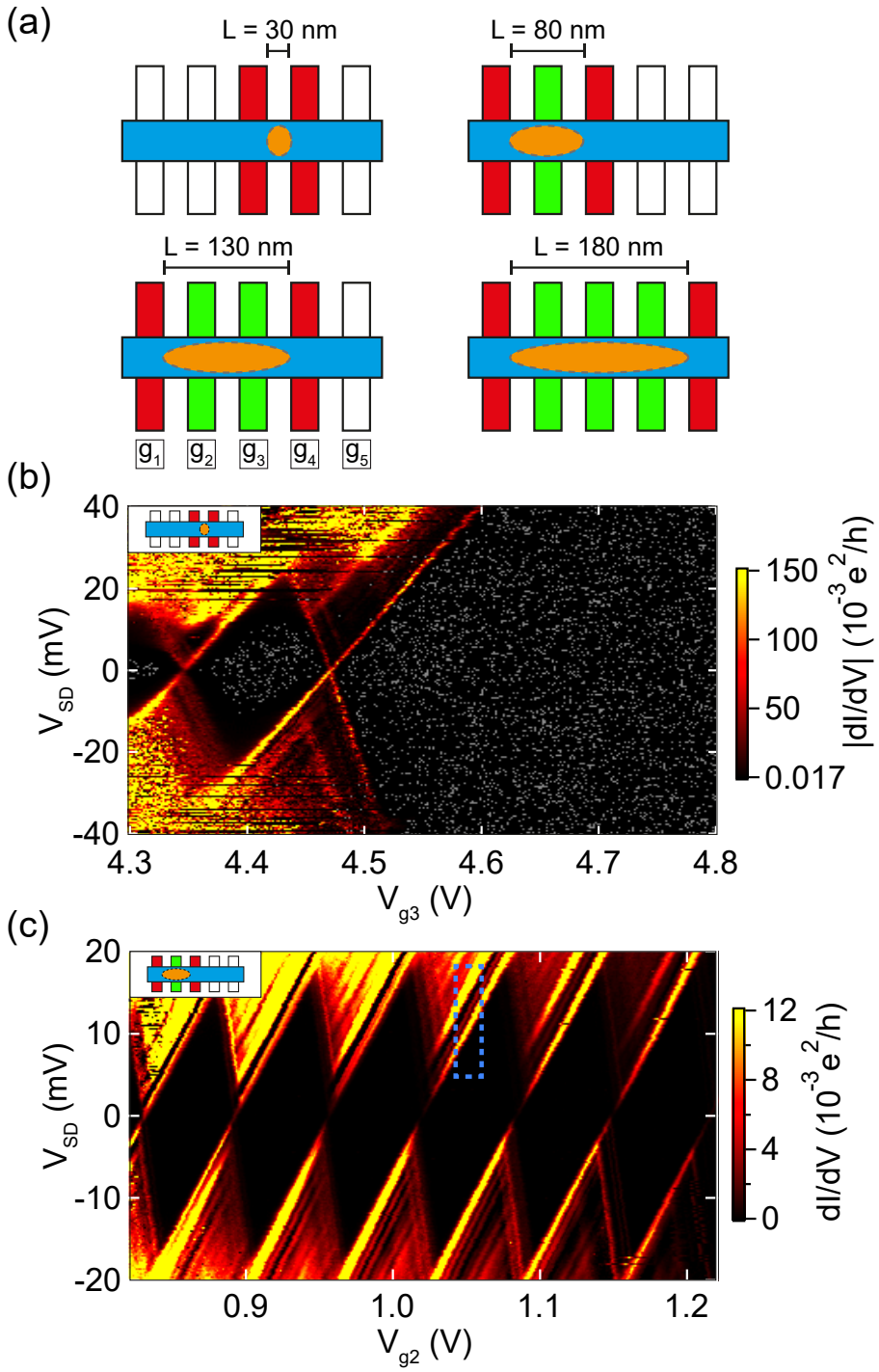

Figure 5.2: (a). Schematic picture of the gate configurations used to form QDs (orange) of different lengths using 2, 3, 4 and 5 gates, respectively. (b) Lock-in signal dI/dV versus V_{SD} and V_{g3} of QD formed by two gates. To enhance contrast, values below the colorscale were given a grey color. Here $V_{g4} = 1700\,\mathrm{mV}$. (c) Lock-in signal dI/dV versus V_{SD} and V_{g2} of QD formed by three gates. Here $V_{g1} = 2000\,\mathrm{mV}$ and $V_{g3} = 4000\,\mathrm{mV}$. Blue dashed rectangle shows an example of an averaging window used to extract excited state energies. Insets in (b) and (c) schematically show used gate configurations.

Table 2 summarizes parameters extracted from the Coulomb diamond measurements. In Figure 5.3 values of the hole addition energy E_{add} are plotted, which were extracted from the height of the Coulomb diamonds. We find that E_{add} is largest for the smallest dot and decreases for increasing dot size, in agreement with the expectation that both charging energy and orbital level splittings decrease with dot size.

# gates	E_{add} (meV)	E_{orb} (meV)	L (nm)	N_{est}
2	26	12.8	30	1, see main text
3	17	4.8	80	15
4	13	2.1	130	35
5	10	1.3	180	38

Table 2: Typical extracted single dot parameters: addition energies E_{add}, excited state energies E_{orb}, lithographically defined distances L between gates creating QD tunnel barriers, and estimated hole numbers N_{est}.

The conductance measurements feature additional resonances at higher values of V_{SD} [136]. We extract energies for these resonances by averaging the difference of the first resonance and the ground state transition, in windows similar to the one drawn in Figure 5.2 c. Here we convert the difference in V_{SD} to energy using lever arms determined from the slopes of each Coulomb diamond. The third column of Table 2 lists typical energies E_{orb} found in this way for the different dot sizes. Consistent with the level splitting of orbital hole states [212, 213], E_{orb} depends strongly on the longitudinal dot size, with smaller dots featuring higher values of E_{orb}. Note that incomplete knowledge of the exact confinement potential and the hole effective mass makes it difficult to compare our measurements to a theoretical model of orbital level splitting.

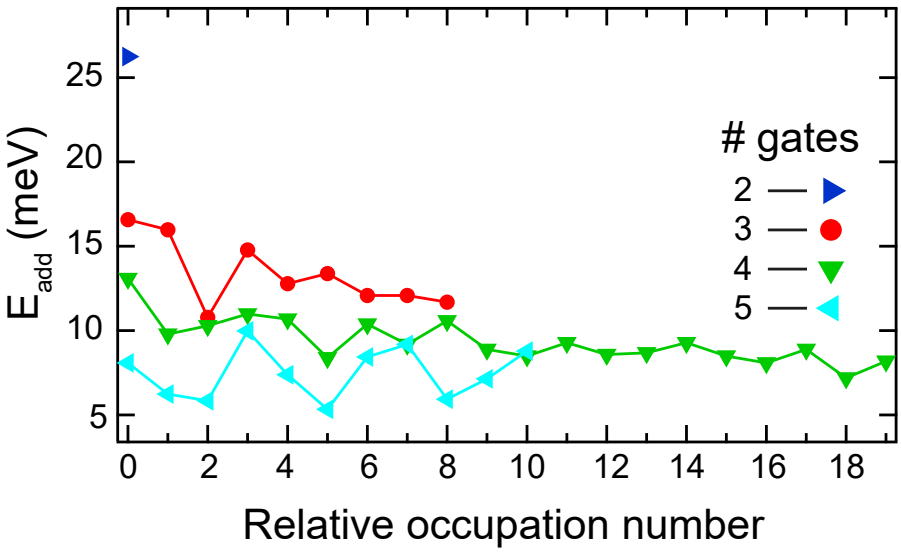

Figure 5.3: Extracted values of E_{add} for various QD lengths as a function of relative occupation number.

Furthermore, we estimate the lowest measurable hole occupation number N_{est} for the different dot sizes by comparing the used gate voltages with pinch-off voltages obtained at high V_{SD}. For dots formed by 3 to 5 neighboring gates, we find relatively low occupation numbers ranging from 15 to 38 (see Table 2). This method is not reliable for QDs defined by only two gates, since both gates directly define the tunnel barriers of the dot. However, several indications suggest that single-hole occupation is reached in this case. First of all, the last Coulomb diamond edge visible in Figure 5.2 b increases linearly up to at least $|V_{SD}| = 40\,\text{mV}$. Furthermore, even at high V_{SD}, no features involving tunneling of multiple holes are observed for the last visible Coulomb diamond (which would appear as lines intersecting the diamond edges on the high gate voltage side). We do find multiple resonances in the last diamond for low V_{SD}, which could arise from tunneling involving excited states. However, the splitting of these lines is lower than that found for the larger dots. Therefore, it is unlikely that these resonances correspond to excited orbital states in a small QD. Furthermore, we observe (not shown) that the splitting of the resonances strongly depends on gate voltages applied to g_2 and g_5 (flanking the barriers of the dot), again making it implausible that they correspond to excited orbital states [214]. A likely explanation is that these lines arise

from modulation of the reservoir density of states [213–215]. Finally, the energy of the first excited state in the second Coulomb diamond in Figure 5.2 b (around $V_{g3} = 4.35\,\mathrm{V}$) appears to be significantly reduced with respect to that found in the last diamond, consistent with an exchange energy appearing for two-hole states. More conclusive evidence of single hole occupation could be obtained by using a charge sensor [135].

Finally, we observed in multiple devices that QDs formed by three or more gates tend to split up when biasing the center gates too positively. This impedes reaching single-hole occupation for the larger dot sizes. Moreover, conductance becomes too low to measure when increasing the gate voltages, again potentially preventing the observation of single-hole occupation regimes. In the device studied here, this seems to be not the case for the dot made by two gates. The conductance exceeds $0.1\,e^2/h$ on the last diamond in Figure 5.2 b, thus adding more evidence for the single-hole regime.

5.5 Double QD Formation and Pauli Spin Blockade

Next, we demonstrate controllable formation of double QDs. As shown in the charge stability diagrams in Figure 5.4 a, a single QD formed by five gates can be continuously split up into a double tunnel-coupled QD, by increasing the voltage on gate g_3. Here, the voltage on gates g_2 and g_4 are swept and the current through the NW is measured for each point. The leftmost charge stability diagram shows single-dot behavior, in which diagonal lines are Coulomb peaks corresponding to sequential addition of single holes to the dot. The middle panel shows a charge stability diagram of a double QD featuring high coupling between the dots, as evidenced by the bending of the charging lines. The right panel shows conductance only when the electrochemical potentials of the two dots are aligned, in the form of bias triangles [148]. The absence of conductance along the charging lines indicates that significant cotunneling with the lead reservoirs can be avoided. These measurements indicate that we have a large amount of control over the capacitive coupling and tunnel-coupling between the two QDs.

Pauli spin blockade is a basic ingredient of many spin qubit experiments, in which

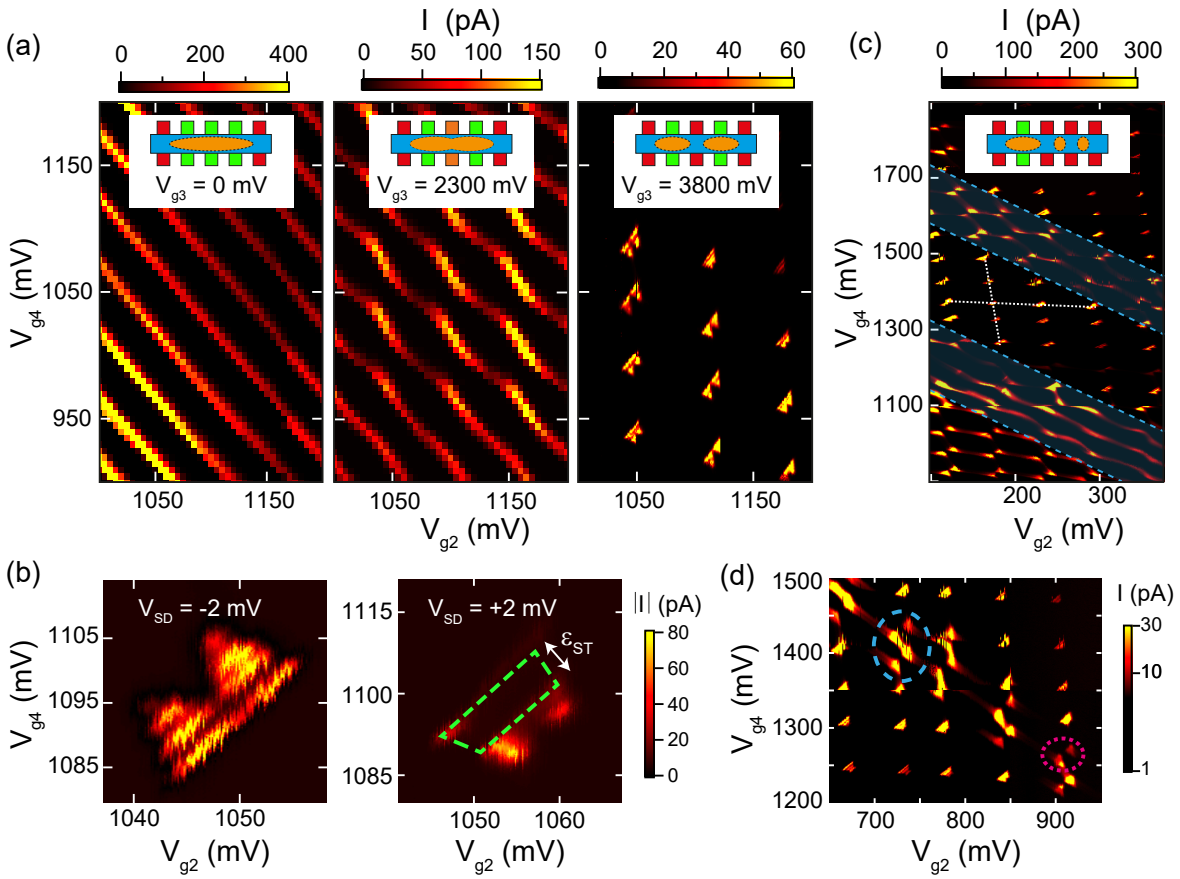

Figure 5.4: (a) Charge stability diagrams for different values of the voltage on g_3, showing a transition from a single QD to a double QD, at $V_{SD} = 2$ mV. Insets schematically show QD configurations. (b) Zoom-in of a pair of bias triangles, at $V_{g3} = 3800$ mV. Plotted is the dc current for positive and negative V_{SD}. The strong reduction in the area enclosed by the dashed green line indicates the presence of Pauli spin blockade. (c) Charge stability diagram with highlighted (shaded blue regions) triple QD features. White dotted lines indicate the slope of charge transitions of the outer two dots. (d) Charge stability diagram of triple QD. Dashed blue and dotted pink circles highlight triple dot resonances. In (c) and (d), $V_{g1} = 2000$ mV, $V_{g3} = 3800$ mV, and $V_{g5} = 2800$ mV.

interdot transitions are blocked for spin triplet but not for singlet states [147, 151]. As such, it forms a means of reading out spin qubit states. When measuring the conductance through a double QD, the blockade may be observed for one sign of V_{SD}, but not for the other. In this work, the relevant spin states are those of Kramers doublets formed by mixed heavy hole and light hole states [13].

We observe signatures of PSB at several interdot transitions when measuring bias triangles for positive and negative V_{SD}, in the form of a region of reduced conductance inside the bias triangles for one sign of V_{SD}. Figure 5.4 (b) focuses on one such an

interdot transition where the current inside the region indicated by the dashed green line is suppressed by roughly a factor 10 for positive V_{SD}. The size of the blockaded region is determined by the singlet-triplet splitting ϵ_{ST} in the single dots (see white arrow in Fig. 5.4 b, right panel). We find ε_{ST} to be 1 meV, which compares well with other measurements [142, 144]. Moreover, we observe a leakage current that depends on the detuning of the electrochemical potentials in the two dots and on the magnitude of an applied magnetic field. In particular, we find a small leakage current at low detuning that is consistent with an effective T(1,1) to S(0,2) transition, and a larger current at higher detuning consistent with a T(1,1) to T(0,2) transition. Various processes may lift PSB, including spin-flip cotunneling, spin-flip reservoir exchange [216], hyperfine interaction, and SOI [142, 144, 217]. The resulting leakage current thus forms a probe to detect the strength of these processes, but a detailed study of this goes beyond the scope of the present work.

5.6 Triple QD

We find that the double QD can be further subdivided into a triple QD, by increasing the voltage on g_4. In this case, the triple dot is likely composed of two small QDs between gate pairs g_3-g_4 and g_4-g_5, as well as a larger QD between g_1-g_3. In the charge stability diagram shown in Figure 5.4 c, triple dot features appear as lines with enhanced conductance with an intermediate slope (see dashed blue lines). Figure 5.4 d shows a zoomed-in region of the triple QD charge stability diagram. Similar to bias triangles in a double QD, conductance is enhanced when the electrochemical potential of the center dot is aligned with that of one of the outer dots (dotted pink circle in Fig. 5.4 d), or when the electrochemical potentials of all three dots are aligned (dashed blue circle in Fig. 5.4 d) [218, 219]. The fact that we also observe conductance at points corresponding to double QD bias triangles suggests that there is cotunneling involving the center dot present in the measurements, resulting in conductance even when only the electrochemical potentials of two out of three dots are aligned.

5.7 Conclusion

The demonstration of tunable single, double, and triple QDs opens the way to perform spin qubit experiments with few holes in these devices. Reaching the single-hole regime is particularly important, as it makes single and two-qubit operations much more straightforward. Overall, we observe very good repeatability of the measurements, with gate voltage changes of 1 V leading to no observable shifts in charge stability diagrams. These results enable several follow-up experiments. In particular, the strength and electric field dependence of the SOI could be determined from magnetic field dependence of leakage current in a double QD in the PSB regime [142, 144, 217]. Moreover, we expect that a slightly different gate design than used here will enable reaching single-hole occupation in a controllable way.

5.8 Acknowledgements

We thank C. Kloeffel, D. Loss, and M. Rancic for helpful discussions. We acknowledge the support of the Swiss National Science Foundation (Ambizione Grant No. PZOOP2161284/1, Project Grant No. 157213, and Project Grant No. 179024), the Swiss Nanoscience Institute, the European Microkelvin Platform EMP, the NCCR Quantum Science and Technology (QSIT), and the Netherlands Organization for Scientific Research (NWO).

6 Summary and Outlook

In **chapter 3** the investigation of a H plasma etching technique, to anisotropically etch graphite and graphene, was presented. First, graphite samples were used to examine the influence of important plasma parameters (gas pressure and sample-plasma distance) on the etching characteristics. Two distinct plasma regimes could be identified: the *remote* and the *direct* regime. In the direct plasma regime, the samples were lying inside the glowing part of the plasma, where highly energetic ions are present, which continuously induce new defects during the exposure and lead to perforated sample surfaces. In contrast, samples placed outside the glowing part of the plasma, i.e. in the remote regime, showed regular hexagonal etch pits. These etch pits were seen to grow in size but no new, additional etch pits were created, which indicates that etching proceeds only from pre-existing defects and leaves the basal plane pristine. Hence, the remote regime is particularly useful because artificial defects can be used to fabricate custom-made nano structures with, presumably, well-defined ZZ edges. In a further step of the experiment, the substrate influence on the etching of SL graphene was investigated. It was found that graphene on a SiO_2 substrate is etched isotropically, whereas graphene on hBN exhibits anisotropic etching, featuring regular hexagonal etch pits.

With this anisotropic etching technique at hand, diverse graphene nano structures such as, e.g. GNRs can be fabricated. In earlier work [62, 63], it was found that H plasma etched hexagon edges follow the ZZ direction of the graphene lattice. However, it was not clear how high the edge quality really is on a microscopic level. This open question is addressed in **chapter 4**, where H plasma defined graphene edges were characterized by means of atomic resolution AFM, Raman spectroscopy, and low-temperature electronic transport measurements. It was found that hexagon edges on graphite follow the ZZ direction of the crystal lattice, and the absence of the Raman D-peak indicated a high quality of these edges. Hexagon edges created in SL graphene on

hBN, on the other hand, exhibited a quite considerable D-peak intensity in the Raman spectrum. Polarization angle dependent measurements revealed an edge configuration consisting of approximately 60 % ZZ and 40 % AC-30° segments. Furthermore, valley-isospin conductance oscillations were analyzed and compared to quantum transport calculations to get insight into the nature of the edges. The calculations for edges with AC-30° segments fit the experimental data best, and, hence, supported the findings from the Raman measurements. Moreover, transport through H plasma defined and RIE defined constrictions was found to have similar mobilities, also indicating the presence of edge disorder at H plasma defined edges.

The above-mentioned findings indicate that the H plasma etching technique of SL graphene on hBN needs to be further optimized in order to obtain pure crystalline graphene edges. Temperature induced reconstruction of ZZ edges could play a role in the H plasma etching process [117]. Hence, future experiments might focus on the investigation of the edge quality as a function of etching temperature and, possibly, yield a temperature range, which allows for the etching of higher quality graphene edges. However, the etching is only working in a quite narrow temperature range and special care needs to be taken when approaching lower temperatures because graphane could be formed. A second possible cause for the observed edge disorder could be hBN-graphene interactions, which negatively influence the quality of the etch. It was shown that the small lattice offsets of graphene and hBN lead to Moiré super-lattice effects [172, 199], which, depending on the relative rotation angle of the two material layers, result in different influences on the electronic structure of graphene. It is plausible that a change of the electronic structure of graphene has an influence on the quality of the etch. Hence, future experiments could focus on the enhancement of the edge quality by optimizing the relative rotation angle between graphene and the hBN substrate.

Once the H plasma etching technique is optimized and enabled to create high quality ZZ edges, a range of possible experiments comes within reach such as, e.g. the realization of edge-magnetism and spin-filtering experiments [30].

In **chapter 5** the formation of single QDs of various sizes with low occupation numbers in Ge/Si core/shell NWs was presented. In the smallest QD, indications for the single-hole regime were found. Furthermore, important QD parameters, such as addition energies and orbital energies were extracted. In the same device, double QDs and triple QDs were formed and PSB was observed in a double QD.

Future experiments could focus on the investigation of the leakage current in the PSB regime. The dependence of the leakage current on the detuning of the two QDs and on the externally applied magnetic field can give insight into mechanisms, which lift the blockade such as, e.g. hyperfine interaction, SOI, and spin-flip co-tunneling.

Next-generation devices are planned to be equipped with side-gates, which allow application of electric fields across the NW and, therefore, tuning the strength of the SOI and the g-factor. Electric-dipole-induced spin resonance (EDSR) experiments could be performed to investigate the functionality of the electric tuneability of the SOI and the g-factor.

In a wider context, circuit quantum electrodynamics experiments might be envisaged, where several spin-qubits are coupled through a transmission line [132]. The tuneability of the SOI and the g-factor would enable the operation of single and two-qubit gates.

References

[1] R. P. Feynman. *Simulating physics with computers.* International Journal of Theoretical Physics **21**, 467 (1982).

[2] R. P. Feynman. *Quantum mechanical computers.* Foundations of Physics **16**, 507 (1986).

[3] J. I. Cirac and P. Zoller. *Quantum computations with cold trapped ions.* Physical Review Letters **74**, 4091 (1995).

[4] I. L. Chuang, N. Gershenfeld, and M. Kubinec. *Experimental implementation of fast quantum searching.* Physical Review Letters **80**, 3408 (1998).

[5] G. K. Brennen, C. M. Caves, P. S. Jessen, and I. H. Deutsch. *Quantum logic gates in optical lattices.* Physical Review Letters **82**, 1060 (1999).

[6] D. Loss and D. P. DiVincenzo. *Quantum computation with quantum dots.* Physical Review A **57**, 120 (1998).

[7] S. Tarucha, D. Austing, T. Honda, R. Van der Hage, and L. P. Kouwenhoven. *Shell filling and spin effects in a few electron quantum dot.* Physical Review Letters **77**, 3613 (1996).

[8] J. Elzerman, R. Hanson, L. W. Van Beveren, B. Witkamp, L. Vandersypen, and L. P. Kouwenhoven. *Single-shot read-out of an individual electron spin in a quantum dot.* Nature **430**, 431 (2004).

[9] J. R. Petta, A. C. Johnson, J. M. Taylor, E. A. Laird, A. Yacoby, M. D. Lukin, C. M. Marcus, M. P. Hanson, and A. C. Gossard. *Coherent manipulation of coupled electron spins in semiconductor quantum dots.* Science **309**, 2180 (2005).

[10] M. Fujita, K. Wakabayashi, K. Nakada, and K. Kusakabe. *Peculiar Localized States at Zigzag Graphite Edge.* Journal of the Physical Society of Japan **65**, 1920 (1996).

[11] J. Klinovaja and D. Loss. *Giant Spin-Orbit Interaction Due to Rotating Magnetic Fields in Graphene Nanoribbons.* Physical Review X **3**, 011008 (2013).

[12] B. Trauzettel, D. V. Bulaev, D. Loss, and G. Burkard. *Spin qubits in graphene quantum dots.* Nature Physics **3**, 192 (2007).

[13] C. Kloeffel, M. Trif, and D. Loss. *Strong spin-orbit interaction and helical hole states in Ge/Si nanowires.* Physical Review B **84**, 195314 (2011).

[14] F. Maier, C. Kloeffel, and D. Loss. *Tunable g factor and phonon-mediated hole spin relaxation in Ge/Si nanowire quantum dots.* Physical Review B **87**, 161305 (2013).

[15] M. Brauns, J. Ridderbos, A. Li, E. P. Bakkers, and F. A. Zwanenburg. *Electric-field dependent g-factor anisotropy in Ge-Si core-shell nanowire quantum dots.* Physical Review B **93**, 121408 (2016).

[16] R. Peierls. *Quelques proprietes typiques des corpses solides.* Annales de le Institut Poincare **5**, 177 (1935).

[17] L. Landau. *Zur Theorie der phasenumwandlungen II.* Physikalische Zeitschrift der Sowjetunion **11**, 26 (1937).

[18] P. R. Wallace. *The band theory of graphite.* Physical Review **71**, 622 (1947).

[19] J. McClure. *Diamagnetism of graphite.* Physical Review **104**, 666 (1956).

[20] J. Slonczewski and P. Weiss. *Band structure of graphite.* Physical Review **109**, 272 (1958).

[21] K. S. Novoselov, A. K. Geim, S. V. Morozov, D. Jiang, Y. Zhang, S. V. Dubonos, I. V. Grigorieva, and A. A. Firsov. *Electric field effect in atomically thin carbon films.* Science **306**, 666 (2004).

[22] C. Lee, X. Wei, J. W. Kysar, and J. Hone. *Measurement of the elastic properties and intrinsic strength of monolayer graphene.* Science **321**, 385 (2008).

[23] A. A. Balandin, S. Ghosh, W. Bao, I. Calizo, D. Teweldebrhan, F. Miao, and C. N. Lau. *Superior thermal conductivity of single-layer graphene.* Nano Letters **8**, 902 (2008).

[24] K. I. Bolotin, K. Sikes, Z. Jiang, M. Klima, G. Fudenberg, J. Hone, P. Kim, and H. Stormer. *Ultrahigh electron mobility in suspended graphene.* Solid State Communications **146**, 351 (2008).

[25] Y. Zhang, Y.-W. Tan, H. L. Stormer, and P. Kim. *Experimental observation of the quantum Hall effect and Berry's phase in graphene.* Nature **438**, 201 (2005).

[26] M. Katsnelson, K. Novoselov, and A. Geim. *Chiral tunnelling and the Klein paradox in graphene.* Nature Physics **2**, 620 (2006).

[27] A. C. Neto, F. Guinea, N. M. Peres, K. S. Novoselov, and A. K. Geim. *The electronic properties of graphene.* Reviews of Modern Physics **81**, 109 (2009).

[28] Https://atomselectrons.com/2012/03/26/alkenes/.

[29] O. V. Yazyev. *Emergence of magnetism in graphene materials and nanostructures.* Reports on Progress in Physics **73**, 056501 (2010).

[30] Y.-W. Son, M. L. Cohen, and S. G. Louie. *Half-metallic graphene nanoribbons.* Nature **444**, 347 (2006).

[31] F. Muñoz-Rojas, J. Fernández-Rossier, and J. Palacios. *Giant magnetoresistance in ultrasmall graphene based devices.* Physical Review Letters **102**, 136810 (2009).

[32] N. Tombros, A. Veligura, J. Junesch, M. H. Guimarães, I. J. Vera-Marun, H. T. Jonkman, and B. J. Van Wees. *Quantized conductance of a suspended graphene nanoconstriction.* Nature Physics **7**, 697 (2011).

[33] T. Li and S.-P. Lu. *Quantum conductance of graphene nanoribbons with edge defects.* Physical Review B **77**, 085408 (2008).

[34] D. Gunlycke, D. Areshkin, and C. White. *Semiconducting graphene nanostrips with edge disorder.* Applied Physics Letters **90**, 142104 (2007).

[35] D. A. Areshkin, D. Gunlycke, and C. T. White. *Ballistic transport in graphene nanostrips in the presence of disorder: Importance of edge effects.* Nano Letters **7**, 204 (2007).

[36] L. Jiao, X. Wang, G. Diankov, H. Wang, and H. Dai. *Facile synthesis of high-quality graphene nanoribbons.* Nature Nanotechnology **5**, 321 (2010).

[37] D. V. Kosynkin, A. L. Higginbotham, A. Sinitskii, J. R. Lomeda, A. Dimiev, B. K. Price, and J. M. Tour. *Longitudinal unzipping of carbon nanotubes to form graphene nanoribbons.* Nature **458**, 872 (2009).

[38] X. Li, X. Wang, L. Zhang, S. Lee, and H. Dai. *Chemically derived, ultrasmooth graphene nanoribbon semiconductors.* Science **319**, 1229 (2008).

[39] P. Ruffieux, S. Wang, B. Yang, C. Sánchez-Sánchez, J. Liu, T. Dienel, L. Talirz, P. Shinde, C. A. Pignedoli, D. Passerone, et al. *On-surface synthesis of graphene nanoribbons with zigzag edge topology.* Nature **531**, 489 (2016).

[40] J. Cai, P. Ruffieux, R. Jaafar, M. Bieri, T. Braun, S. Blankenburg, M. Muoth, A. P. Seitsonen, M. Saleh, X. Feng, et al. *Atomically precise bottom-up fabrication of graphene nanoribbons.* Nature **466**, 470 (2010).

[41] L. Talirz, H. SoÌˆde, T. Dumslaff, S. Wang, J. R. Sanchez-Valencia, J. Liu, P. Shinde, C. A. Pignedoli, L. Liang, V. Meunier, et al. *On-surface synthesis and characterization of 9-atom wide armchair graphene nanoribbons.* ACS Nano **11**, 1380 (2017).

[42] P. Ruffieux, J. Cai, N. C. Plumb, L. Patthey, D. Prezzi, A. Ferretti, E. Molinari, X. Feng, K. Müllen, C. A. Pignedoli, et al. *Electronic structure of atomically precise graphene nanoribbons.* ACS Nano **6**, 6930 (2012).

[43] M. Koch, F. Ample, C. Joachim, and L. Grill. *Voltage-dependent conductance of a single graphene nanoribbon.* Nature Nanotechnology **7**, 713 (2012).

[44] H. Huang, D. Wei, J. Sun, S. L. Wong, Y. P. Feng, A. C. Neto, and A. T. S. Wee. *Spatially resolved electronic structures of atomically precise armchair graphene nanoribbons.* Scientific Reports **2**, 983 (2012).

[45] J. Van Der Lit, M. P. Boneschanscher, D. Vanmaekelbergh, M. Ijäs, A. Uppstu, M. Ervasti, A. Harju, P. Liljeroth, and I. Swart. *Suppression of electron–vibron coupling in graphene nanoribbons contacted via a single atom.* Nature Communications **4**, 2023 (2013).

[46] L. C. Campos, V. R. Manfrinato, J. D. Sanchez-Yamagishi, J. Kong, and P. Jarillo-Herrero. *Anisotropic etching and nanoribbon formation in single-layer graphene.* Nano Letters **9**, 2600 (2009).

[47] D. Geng, B. Wu, Y. Guo, B. Luo, Y. Xue, J. Chen, G. Yu, and Y. Liu. *Fractal etching of graphene.* Journal of the American Chemical Society **135**, 6431 (2013).

[48] W. Guo, B. Wu, Y. Li, L. Wang, J. Chen, B. Chen, Z. Zhang, L. Peng, S. Wang, and Y. Liu. *Governing rule for dynamic formation of grain boundaries in grown graphene.* ACS Nano **9**, 5792 (2015).

[49] Y. Zhang, Z. Li, P. Kim, L. Zhang, and C. Zhou. *Anisotropic hydrogen etching of chemical vapor deposited graphene.* ACS Nano **6**, 126 (2011).

[50] Y. Y. Stehle, X. Sang, R. R. Unocic, D. Voylov, R. K. Jackson, S. Smirnov, and I. Vlassiouk. *Anisotropic Etching of Hexagonal Boron Nitride and Graphene: Question of Edge Terminations.* Nano Letters **17**, 7306 (2017).

[51] P. Nemes-Incze, G. Magda, K. Kamarás, and L. P. Biró. *Crystallographically selective nanopatterning of graphene on SiO2.* Nano Research **3**, 110 (2010).

[52] B. Krauss, P. Nemes-Incze, V. Skakalova, L. P. Biro, K. v. Klitzing, and J. H. Smet. *Raman scattering at pure graphene zigzag edges.* Nano Letters **10**, 4544 (2010).

[53] F. Oberhuber, S. Blien, S. Heydrich, F. Yaghobian, T. Korn, C. Schüller, C. Strunk, D. Weiss, and J. Eroms. *Weak localization and Raman study of anisotropically etched graphene antidots.* Applied Physics Letters **103**, 143111 (2013).

[54] F. Oberhuber, S. Blien, F. Schupp, D. Weiss, and J. Eroms. *Anisotropic etching of graphene in inert and oxygen atmospheres.* Physica Status Solidi (a) **214** (2017).

[55] M. C. Lemme, D. C. Bell, J. R. Williams, L. A. Stern, B. W. Baugher, P. Jarillo-Herrero, and C. M. Marcus. *Etching of graphene devices with a helium ion beam.* ACS Nano **3**, 2674 (2009).

[56] A. N. Abbas, G. Liu, B. Liu, L. Zhang, H. Liu, D. Ohlberg, W. Wu, and C. Zhou. *Patterning, characterization, and chemical sensing applications of graphene nanoribbon arrays down to 5 nm using helium ion beam lithography.* ACS Nano **8**, 1538 (2014).

[57] Z. J. Qi, J. A. Rodriguez-Manzo, A. R. Botello-Mendez, S. J. Hong, E. A. Stach, Y. W. Park, J.-C. Charlier, M. Drndic, and A. C. Johnson. *Correlating atomic structure and transport in suspended graphene nanoribbons.* Nano Letters **14**, 4238 (2014).

[58] J. Baringhaus, M. Ruan, F. Edler, A. Tejeda, M. Sicot, A. Taleb-Ibrahimi, A.-P. Li, Z. Jiang, E. H. Conrad, C. Berger, et al. *Exceptional ballistic transport in epitaxial graphene nanoribbons.* Nature **506**, 349 (2014).

[59] G. Z. Magda, X. Jin, I. Hagymási, P. Vancsó, Z. Osvath, P. Nemes-Incze, C. Hwang, L. P. Biró, and L. Tapaszto. *Room-temperature magnetic order on zigzag edges of narrow graphene nanoribbons.* Nature **514**, 608 (2014).

[60] B. McCarroll and D. McKee. *The reactivity of graphite surfaces with atoms and molecules of hydrogen, oxygen and nitrogen.* Carbon **9**, 301 (1971).

[61] B. McCarroll and D. McKee. *Interaction of atomic hydrogen and nitrogen with graphite surfaces.* Nature **225**, 722 (1970).

[62] R. Yang, L. Zhang, Y. Wang, Z. Shi, D. Shi, H. Gao, E. Wang, and G. Zhang. *An anisotropic etching effect in the graphene basal plane.* Advanced Materials **22**, 4014 (2010).

[63] Z. Shi, R. Yang, L. Zhang, Y. Wang, D. Liu, D. Shi, E. Wang, and G. Zhang. *Patterning graphene with zigzag edges by self-aligned anisotropic etching.* Advanced Materials **23**, 3061 (2011).

[64] L. Xie, L. Jiao, and H. Dai. *Selective etching of graphene edges by hydrogen plasma.* Journal of the American Chemical Society **132**, 14751 (2010).

[65] G. Wang, S. Wu, T. Zhang, P. Chen, X. Lu, S. Wang, D. Wang, K. Watanabe, T. Taniguchi, D. Shi, et al. *Patterning monolayer graphene with zigzag edges on hexagonal boron nitride by anisotropic etching.* Applied Physics Letters **109**, 053101 (2016).

[66] G. Diankov, M. Neumann, and D. Goldhaber-Gordon. *Extreme monolayer-selectivity of hydrogen-plasma reactions with graphene.* ACS Nano **7**, 1324 (2013).

[67] D. Hug, S. Zihlmann, M. K. Rehmann, Y. B. Kalyoncu, T. N. Camenzind, L. Marot, K. Watanabe, T. Taniguchi, and D. M. Zumbühl. *Anisotropic etching of graphite and graphene in a remote hydrogen plasma.* Npj 2D Materials and Applications **1**, 21 (2017).

[68] X. Wang, Y. Ouyang, L. Jiao, H. Wang, L. Xie, J. Wu, J. Guo, and H. Dai. *Graphene nanoribbons with smooth edges behave as quantum wires.* Nature Nanotechnology **6**, 563 (2011).

[69] L. Xie, H. Wang, C. Jin, X. Wang, L. Jiao, K. Suenaga, and H. Dai. *Graphene nanoribbons from unzipped carbon nanotubes: atomic structures, Raman spectroscopy, and electrical properties.* Journal of the American Chemical Society **133**, 10394 (2011).

[70] A. Chuvilin, J. C. Meyer, G. Algara-Siller, and U. Kaiser. *From graphene constrictions to single carbon chains.* New Journal of Physics **11**, 083019 (2009).

[71] Ç. Ö. Girit, J. C. Meyer, R. Erni, M. D. Rossell, C. Kisielowski, L. Yang, C.-H. Park, M. Crommie, M. L. Cohen, S. G. Louie, et al. *Graphene at the edge: stability and dynamics.* Science **323**, 1705 (2009).

[72] X. Jia, M. Hofmann, V. Meunier, B. G. Sumpter, J. Campos-Delgado, J. M. Romo-Herrera, H. Son, Y.-P. Hsieh, A. Reina, J. Kong, et al. *Controlled formation of sharp zigzag and armchair edges in graphitic nanoribbons.* Science **323**, 1701 (2009).

[73] P. Koskinen, S. Malola, and H. Häkkinen. *Evidence for graphene edges beyond zigzag and armchair.* Physical Review B **80**, 073401 (2009).

[74] Z. Liu, K. Suenaga, P. J. Harris, and S. Iijima. *Open and closed edges of graphene layers.* Physical Review Letters **102**, 015501 (2009).

[75] K. Suenaga and M. Koshino. *Atom-by-atom spectroscopy at graphene edge.* Nature **468**, 1088 (2010).

[76] R. Zan, Q. M. Ramasse, U. Bangert, and K. S. Novoselov. *Graphene reknits its holes.* Nano Letters **12**, 3936 (2012).

[77] Y. Niimi, T. Matsui, H. Kambara, K. Tagami, M. Tsukada, and H. Fukuyama. *Scanning tunneling microscopy and spectroscopy of the electronic local density of states of graphite surfaces near monoatomic step edges.* Physical Review B **73**, 085421 (2006).

[78] K. A. Ritter and J. W. Lyding. *The influence of edge structure on the electronic properties of graphene quantum dots and nanoribbons.* Nature Materials **8**, 235 (2009).

[79] X. Zhang, O. V. Yazyev, J. Feng, L. Xie, C. Tao, Y.-C. Chen, L. Jiao, Z. Pedramrazi, A. Zettl, S. G. Louie, et al. *Experimentally engineering the edge termination of graphene nanoribbons.* ACS Nano **7**, 198 (2012).

[80] Y. Kobayashi, K.-i. Fukui, T. Enoki, and K. Kusakabe. *Edge state on hydrogen-terminated graphite edges investigated by scanning tunneling microscopy.* Physical Review B **73**, 125415 (2006).

[81] C. Tao, L. Jiao, O. V. Yazyev, Y.-C. Chen, J. Feng, X. Zhang, R. B. Capaz, J. M. Tour, A. Zettl, S. G. Louie, H. Dai, and M. F. Crommie. *Spatially resolving edge states of chiral graphene nanoribbons.* Nature Physics **7**, 616 (2011).

[82] M. Pan, E. C. Girão, X. Jia, S. Bhaviripudi, Q. Li, J. Kong, V. Meunier, and M. S. Dresselhaus. *Topographic and Spectroscopic Characterization of Electronic Edge States in CVD Grown Graphene Nanoribbons.* Nano Letters **12**, 1928 (2012).

[83] M. Ijäs, M. Ervasti, A. Uppstu, P. Liljeroth, J. van der Lit, I. Swart, and A. Harju. *Electronic states in finite graphene nanoribbons: Effect of charging and defects.* Physical Review B **88**, 075429 (2013).

[84] S. Kawai, S. Saito, S. Osumi, S. Yamaguchi, A. S. Foster, P. Spijker, and E. Meyer. *Atomically controlled substitutional boron-doping of graphene nanoribbons.* Nature Communications **6**, 8098 (2015).

[85] S. Kawai, S. Nakatsuka, T. Hatakeyama, R. Pawlak, T. Meier, J. Tracey, E. Meyer, and A. S. Foster. *Multiple heteroatom substitution to graphene nanoribbon.* Science Advances **4**, eaar7181 (2018).

[86] C. Stampfer, J. Güttinger, S. Hellmüller, F. Molitor, K. Ensslin, and T. Ihn. *Energy gaps in etched graphene nanoribbons.* Physical Review Letters **102**, 056403 (2009).

[87] M. Han, B. Özyilmaz, Y. Zhang, and P. Kim. *Energy Band-Gap Engineering of Graphene Nanoribbons.* Physical Review Letters **98**, 206805 (2007).

[88] J. Bai, R. Cheng, F. Xiu, L. Liao, M. Wang, A. Shailos, K. L. Wang, Y. Huang, and X. Duan. *Very large magnetoresistance in graphene nanoribbons.* Nature Nanotechnology **5**, 655 (2010).

[89] P. Gallagher, K. Todd, and D. Goldhaber-Gordon. *Disorder-induced gap behavior in graphene nanoribbons.* Physical Review B **81**, 115409 (2010).

[90] B. Özyilmaz, P. Jarillo-Herrero, D. Efetov, and P. Kim. *Electronic transport in locally gated graphene nanoconstrictions.* Applied Physics Letters **91**, 192107 (2007).

[91] D. Bischoff, T. Krähenmann, S. Dröscher, M. A. Gruner, C. Barraud, T. Ihn, and K. Ensslin. *Reactive-ion-etched graphene nanoribbons on a hexagonal boron nitride substrate.* Applied Physics Letters **101**, 203103 (2012).

[92] M. Nevius, F. Wang, C. Mathieu, N. Barrett, A. Sala, T. Mentes, A. Locatelli, and E. Conrad. *The bottom-up growth of edge specific graphene nanoribbons.* Nano Letters **14**, 6080 (2014).

[93] J. Aprojanz, S. R. Power, P. Bampoulis, S. Roche, A.-P. Jauho, H. J. Zandvliet, A. A. Zakharov, and C. Tegenkamp. *Ballistic tracks in graphene nanoribbons.* Nature Communications **9**, 4426 (2018).

[94] B. Terrés, L. Chizhova, F. Libisch, J. Peiro, D. Jörger, S. Engels, A. Girschik, K. Watanabe, T. Taniguchi, S. Rotkin, et al. *Size quantization of Dirac fermions in graphene constrictions.* Nature Communications **7**, 11528 (2016).

[95] K. Nakada, M. Fujita, G. Dresselhaus, and M. S. Dresselhaus. *Edge state in graphene ribbons: Nanometer size effect and edge shape dependence.* Physical Review B **54**, 17954 (1996).

[96] R. Grubbs and S. George. *Attenuation of hydrogen radicals traveling under flowing gas conditions through tubes of different materials.* Journal of Vacuum Science & Technology A: Vacuum, Surfaces, and Films **24**, 486 (2006).

[97] K. E. Shuler and K. J. Laidler. *The Kinetics of Heterogeneous Atom and Radical Reactions. I. The Recombination of Hydrogen Atoms on Surfaces.* Journal of Chemical Physics **17**, 1212 (1949).

[98] A. Horn, A. Schenk, J. Biener, B. Winter, C. Lutterloh, M. Wittmann, and J. Kueppers. *H atom impact induced chemical erosion reaction at CH film surfaces.* Chemical Physics Letters **231**, 193 (1994).

[99] A. Davydova, E. Despiau-Pujo, G. Cunge, and D. B. Graves. *Etching mechanisms of graphene nanoribbons in downstream H2 plasmas: insights from molecular dynamics simulations.* Journal of Physics D: Applied Physics **48**, 195202 (2015).

[100] F. Tuinstra and J. L. Koenig. *Raman spectrum of graphite.* The Journal of Chemical Physics **53**, 1126 (1970).

[101] M. S. Dresselhaus, G. Dresselhaus, R. Saito, and A. Jorio. *Raman spectroscopy of carbon nanotubes.* Physics Reports **409**, 47 (2005).

[102] H. Kuzmany, R. Pfeiffer, M. Hulman, and C. Kramberger. *Raman spectroscopy of fullerenes and fullerene–nanotube composites.* Philosophical Transactions of the Royal Society of London A: Mathematical, Physical and Engineering Sciences **362**, 2375 (2004).

[103] L. Malard, M. Pimenta, G. Dresselhaus, and M. Dresselhaus. *Raman spectroscopy in graphene.* Physics Reports **473**, 51 (2009).

[104] A. C. Ferrari, J. C. Meyer, V. Scardaci, C. Casiraghi, M. Lazzeri, F. Mauri, S. Piscanec, D. Jiang, K. S. Novoselov, S. Roth, and A. K. Geim. *Raman Spectrum of Graphene and Graphene Layers.* Physical Review Letters **97**, 187401 (2006).

[105] M. M. Lucchese, F. Stavale, E. M. Ferreira, C. Vilani, M. Moutinho, R. B. Capaz, C. Achete, and A. Jorio. *Quantifying ion-induced defects and Raman relaxation length in graphene.* Carbon **48**, 1592 (2010).

[106] J.-Y. Hwang, C.-C. Kuo, L.-C. Chen, and K.-H. Chen. *Correlating defect density with carrier mobility in large-scaled graphene films: Raman spectral signatures for the estimation of defect density.* Nanotechnology **21**, 465705 (2010).

[107] C. Casiraghi, A. Hartschuh, H. Qian, S. Piscanec, C. Georgi, A. Fasoli, K. Novoselov, D. Basko, and A. Ferrari. *Raman spectroscopy of graphene edges.* Nano Letters **9**, 1433 (2009).

[108] Y. You, Z. Ni, T. Yu, and Z. Shen. *Edge chirality determination of graphene by Raman spectroscopy.* Applied Physics Letters **93**, 163112 (2008).

[109] A. K. Gupta, T. J. Russin, H. R. Gutiérrez, and P. C. Eklund. *Probing graphene edges via Raman scattering.* ACS Nano **3**, 45 (2008).

[110] Z. H. Ni, T. Yu, Y. H. Lu, Y. Y. Wang, Y. P. Feng, and Z. X. Shen. *Uniaxial strain on graphene: Raman spectroscopy study and band-gap opening.* ACS Nano **2**, 2301 (2008).

[111] T. Mohiuddin, A. Lombardo, R. Nair, A. Bonetti, G. Savini, R. Jalil, N. Bonini, D. Basko, C. Galiotis, N. Marzari, et al. *Uniaxial strain in graphene by Raman spectroscopy: G peak splitting, Grüneisen parameters, and sample orientation.* Physical Review B **79**, 205433 (2009).

[112] M. Kalbac, A. Reina-Cecco, H. Farhat, J. Kong, L. Kavan, and M. S. Dresselhaus. *The influence of strong electron and hole doping on the Raman intensity of chemical vapor-deposition graphene.* ACS Nano **4**, 6055 (2010).

[113] A. Das, S. Pisana, B. Chakraborty, S. Piscanec, S. Saha, U. Waghmare, K. Novoselov, H. Krishnamurthy, A. Geim, A. Ferrari, et al. *Monitoring dopants by Raman scattering in an electrochemically top-gated graphene transistor.* Nature Nanotechnology **3**, 210 (2008).

[114] D. C. Elias, R. R. Nair, T. Mohiuddin, S. Morozov, P. Blake, M. Halsall, A. Ferrari, D. Boukhvalov, M. Katsnelson, A. Geim, et al. *Control of graphene's properties by reversible hydrogenation: evidence for graphane.* Science **323**, 610 (2009).

[115] R. Beams, L. G. Cançado, and L. Novotny. *Raman characterization of defects and dopants in graphene.* Journal of Physics: Condensed Matter **27**, 083002 (2015).

[116] M. Bayle, N. Reckinger, A. Felten, P. Landois, O. Lancry, B. Dutertre, J.-F. Colomer, A.-A. Zahab, L. Henrard, J.-L. Sauvajol, et al. *Determining the number of layers in few-layer graphene by combining Raman spectroscopy and optical contrast.* Journal of Raman Spectroscopy **49**, 36 (2018).

[117] Y. N. Xu, D. Zhan, L. Liu, H. Suo, Z. H. Ni, T. T. Nguyen, C. Zhao, and Z. X. Shen. *Thermal Dynamics of Graphene Edges Investigated by Polarized Raman Spectroscopy.* ACS Nano **5**, 147 (2011).

[118] E. Pallecchi, A. Betz, J. Chaste, G. Fève, B. Huard, T. Kontos, J.-M. Berroir, and B. Plaçais. *Transport scattering time probed through rf admittance of a graphene capacitor.* Physical Review B **83**, 125408 (2011).

[119] V. V. Cheianov, V. Fal'ko, and B. Altshuler. *The focusing of electron flow and a Veselago lens in graphene pn junctions.* Science **315**, 1252 (2007).

[120] A. Rycerz, J. Tworzydło, and C. Beenakker. *Valley filter and valley valve in graphene.* Nature Physics **3**, 172 (2007).

[121] Https://www.researchgate.net/figure/Bloch-sphere-representation-of-a-qubit_fig1_317573486.

[122] C. Handschin, P. Makk, P. Rickhaus, R. Maurand, K. Watanabe, T. Taniguchi, K. Richter, M.-H. Liu, and C. Schönenberger. *Giant valley-isospin conductance oscillations in ballistic graphene.* Nano Letters **17**, 5389 (2017).

[123] Y. Zheng and T. Ando. *Hall conductivity of a two-dimensional graphite system.* Physical Review B **65**, 245420 (2002).

[124] J. Tworzydło, I. Snyman, A. Akhmerov, and C. Beenakker. *Valley-isospin dependence of the quantum Hall effect in a graphene p- n junction.* Physical Review B **76**, 035411 (2007).

[125] D. Abanin and L. Levitov. *Quantized transport in graphene pn junctions in a magnetic field.* Science **317**, 641 (2007).

[126] J. Williams, L. DiCarlo, and C. Marcus. *Quantum Hall effect in a gate-controlled pn junction of graphene.* Science **317**, 638 (2007).

[127] C. R. Dean, A. F. Young, I. Meric, C. Lee, L. Wang, S. Sorgenfrei, K. Watanabe, T. Taniguchi, P. Kim, K. L. Shepard, et al. *Boron nitride substrates for high-quality graphene electronics.* Nature Nanotechnology **5**, 722 (2010).

[128] C. Handschin. *Quantum Transport in Encapsulated Graphene P-N Junctions*. Ph.D. thesis, University of Basel (2017).

[129] L. Wang, I. Meric, P. Huang, Q. Gao, Y. Gao, H. Tran, T. Taniguchi, K. Watanabe, L. Campos, D. Muller, et al. *One-dimensional electrical contact to a two-dimensional material*. Science **342**, 614 (2013).

[130] S. Conesa-Boj, A. Li, S. Koelling, M. Brauns, J. Ridderbos, T. Nguyen, M. Verheijen, P. Koenraad, F. Zwanenburg, and E. P. Bakkers. *Boosting Hole Mobility in Coherently Strained [110]-Oriented Ge–Si Core–Shell Nanowires*. Nano Letters **17**, 2259 (2017).

[131] W. Lu, J. Xiang, B. P. Timko, Y. Wu, and C. M. Lieber. *One-dimensional hole gas in germanium/silicon nanowire heterostructures*. Proceedings of the National Academy of Sciences **102**, 10046 (2005).

[132] C. Kloeffel, M. Trif, P. Stano, and D. Loss. *Circuit QED with hole-spin qubits in Ge/Si nanowire quantum dots*. Physical Review B **88**, 241405 (2013).

[133] L. J. Lauhon, M. S. Gudiksen, D. Wang, and C. M. Lieber. *Epitaxial core–shell and core–multishell nanowire heterostructures*. Nature **420**, 57 (2002).

[134] J. Xiang, W. Lu, Y. Hu, Y. Wu, H. Yan, and C. M. Lieber. *Ge/Si nanowire heterostructures as high-performance field-effect transistors*. Nature **441**, 489 (2006).

[135] Y. Hu, H. O. Churchill, D. J. Reilly, J. Xiang, C. M. Lieber, and C. M. Marcus. *A Ge/Si heterostructure nanowire-based double quantum dot with integrated charge sensor*. Nature Nanotechnology **2**, 622 (2007).

[136] S. Roddaro, A. Fuhrer, P. Brusheim, C. Fasth, H. Xu, L. Samuelson, J. Xiang, and C. Lieber. *Spin states of holes in Ge/Si nanowire quantum dots*. Physical Review Letters **101**, 186802 (2008).

[137] X.-J. Hao, T. Tu, G. Cao, C. Zhou, H.-O. Li, G.-C. Guo, W. Y. Fung, Z. Ji, G.-P. Guo, and W. Lu. *Strong and Tunable Spin- Orbit Coupling of One-Dimensional Holes in Ge/Si Core/Shell Nanowires.* Nano Letters **10**, 2956 (2010).

[138] Y. Hu, F. Kuemmeth, C. M. Lieber, and C. M. Marcus. *Hole spin relaxation in Ge–Si core–shell nanowire qubits.* Nature nanotechnology **7**, 47 (2012).

[139] A. P. Higginbotham, T. W. Larsen, J. Yao, H. Yan, C. M. Lieber, C. M. Marcus, and F. Kuemmeth. *Hole spin coherence in a Ge/Si heterostructure nanowire.* Nano Letters **14**, 3582 (2014).

[140] A. P. Higginbotham, F. Kuemmeth, T. W. Larsen, M. Fitzpatrick, J. Yao, H. Yan, C. M. Lieber, and C. M. Marcus. *Antilocalization of coulomb blockade in a Ge/Si nanowire.* Physical Review Letters **112**, 216806 (2014).

[141] M. Brauns, J. Ridderbos, A. Li, W. G. van der Wiel, E. P. Bakkers, and F. A. Zwanenburg. *Highly tuneable hole quantum dots in Ge-Si core-shell nanowires.* Applied Physics Letters **109**, 143113 (2016).

[142] M. Brauns, J. Ridderbos, A. Li, E. P. Bakkers, W. G. Van Der Wiel, and F. A. Zwanenburg. *Anisotropic Pauli spin blockade in hole quantum dots.* Physical Review B **94**, 041411 (2016).

[143] R. Wang, R. Deacon, J. Yao, C. Lieber, and K. Ishibashi. *Electrical modulation of weak-antilocalization and spin–orbit interaction in dual gated Ge/Si core/shell nanowires.* Semiconductor Science and Technology **32**, 094002 (2017).

[144] A. Zarassi, Z. Su, J. Danon, J. Schwenderling, M. Hocevar, B.-M. Nguyen, J. Yoo, S. A. Dayeh, and S. M. Frolov. *Magnetic field evolution of spin blockade in Ge/Si nanowire double quantum dots.* Physical Review B **95**, 155416 (2017).

[145] H. Watzinger, C. Kloeffel, L. Vukusic, M. D. Rossell, V. Sessi, J. Kukucka, R. Kirchschlager, E. Lausecker, A. Truhlar, M. Glaser, et al. *Heavy-hole states in germanium hut wires.* Nano Letters **16**, 6879 (2016).

[146] W. Pauli. *Über den Zusammenhang des Abschlusses der Elektronengruppen im Atom mit der Komplexstruktur der Spektren.* Zeitschrift für Physik **31**, 765 (1925).

[147] R. Hanson, L. P. Kouwenhoven, J. R. Petta, S. Tarucha, and L. M. Vandersypen. *Spins in few-electron quantum dots.* Reviews of Modern Physics **79**, 1217 (2007).

[148] W. G. Van der Wiel, S. De Franceschi, J. M. Elzerman, T. Fujisawa, S. Tarucha, and L. P. Kouwenhoven. *Electron transport through double quantum dots.* Reviews of Modern Physics **75**, 1 (2002).

[149] N. Van der Vaart, S. Godijn, Y. V. Nazarov, C. Harmans, J. Mooij, L. Molenkamp, and C. Foxon. *Resonant tunneling through two discrete energy states.* Physical Review Letters **74**, 4702 (1995).

[150] D. Averin and Y. V. Nazarov. *Macroscopic quantum tunneling of charge and co-tunneling.* In *Single Charge Tunneling*, 217–247 (Springer, 1992).

[151] K. Ono, D. Austing, Y. Tokura, and S. Tarucha. *Current rectification by Pauli exclusion in a weakly coupled double quantum dot system.* Science **297**, 1313 (2002).

[152] F. Rossella, A. Bertoni, D. Ercolani, M. Rontani, L. Sorba, F. Beltram, and S. Roddaro. *Nanoscale spin rectifiers controlled by the Stark effect.* Nature Nanotechnology **9**, 997 (2014).

[153] O. N. Jouravlev and Y. V. Nazarov. *Electron transport in a double quantum dot governed by a nuclear magnetic field.* Physical Review Letters **96**, 176804 (2006).

[154] K. M. Itoh, J. Kato, M. Uemura, A. K. Kaliteevskii, O. N. Godisov, G. G. Devyatych, A. D. Bulanov, A. V. Gusev, I. D. Kovalev, P. G. Sennikov, et al. *High purity isotopically enriched 29Si and 30Si single crystals: Isotope separation, purification, and growth.* Japanese Journal of Applied Physics **42**, 6248 (2003).

[155] K. Itoh, W. Hansen, E. Haller, J. Farmer, V. Ozhogin, A. Rudnev, and A. Tikhomirov. *High purity isotopically enriched 70 Ge and 74 Ge single crystals: Isotope separation, growth, and properties.* Journal of Materials Research **8**, 1341 (1993).

[156] E. Fermi. *Über die magnetischen Momente der Atomkerne.* Zeitschrift für Physik A Hadrons and Nuclei **60**, 320 (1930).

[157] F. Qassemi, W. Coish, and F. Wilhelm. *Stationary and transient leakage current in the Pauli spin blockade.* Physical Review Letters **102**, 176806 (2009).

[158] W. Coish and F. Qassemi. *Leakage-current line shapes from inelastic cotunneling in the Pauli spin blockade regime.* Physical Review B **84**, 245407 (2011).

[159] J. Danon and Y. V. Nazarov. *Pauli spin blockade in the presence of strong spin-orbit coupling.* Physical Review B **80**, 041301 (2009).

[160] Y.-W. Son, M. L. Cohen, and S. G. Louie. *Energy Gaps in Graphene Nanoribbons.* Physical Review Letters **97**, 216803 (2006).

[161] S. Wang, L. Talirz, C. A. Pignedoli, X. Feng, K. Müllen, R. Fasel, and P. Ruffieux. *Giant edge state splitting at atomically precise graphene zigzag edges.* Nature Communications **7**, 11507 (2016).

[162] E. R. Mucciolo, A. C. Neto, and C. H. Lewenkopf. *Conductance quantization and transport gaps in disordered graphene nanoribbons.* Physical Review B **79**, 075407 (2009).

[163] J. B. Oostinga, B. Sacépé, M. F. Craciun, and A. F. Morpurgo. *Magnetotransport through graphene nanoribbons.* Physical Review B **81**, 193408 (2010).

[164] X. Liu, J. B. Oostinga, A. F. Morpurgo, and L. M. Vandersypen. *Electrostatic confinement of electrons in graphene nanoribbons.* Physical Review B **80**, 121407 (2009).

[165] F. Molitor, C. Stampfer, J. Güttinger, A. Jacobsen, T. Ihn, and K. Ensslin. *Energy and transport gaps in etched graphene nanoribbons.* Semiconductor Science and Technology **25**, 034002 (2010).

[166] NGS Naturgraphit GmbH.

[167] R. K. Janev, D. Reiter, and U. Samm. *Collision Processes in Low-Temperature Hydrogen Plasmas* (Forschungszentrum Juelich GmbH, 2003).

[168] G. Dixon-Lewis, M. M. Sutton, and A. Williams. *The kinetics of hydrogen atom recombination.* Discussions of the Faraday Society **33**, 205 (1962).

[169] Suprasil 310, Heraeus Quarzglas GmbH.

[170] Y. Zhang, V. W. Brar, C. Girit, A. Zettl, and M. F. Crommie. *Origin of spatial charge inhomogeneity in graphene.* Nature Physics **5**, 722 (2009).

[171] R. Decker, Y. Wang, V. W. Brar, W. Regan, H.-Z. Tsai, Q. Wu, W. Gannett, A. Zettl, and M. F. Crommie. *Local Electronic Properties of Graphene on a BN Substrate via Scanning Tunneling Microscopy.* Nano Letters **11**, 2291 (2011).

[172] J. Xue, J. Sanchez-Yamagishi, D. Bulmash, P. Jacquod, A. Deshpande, K. Watanabe, T. Taniguchi, P. Jarillo-Herrero, and B. J. LeRoy. *Scanning tunnelling microscopy and spectroscopy of ultra-flat graphene on hexagonal boron nitride.* Nature Materials **10**, 282 (2011).

[173] Y. C. Kim and M. Boudart. *Recombination of O, N and H atoms on Silica: Kinetics and Mechanism.* ACS Langmuir **7**, 2999 (1991).

[174] T. Taniguchi and K. Watanabe. *Synthesis of high-purity boron nitride single crystals under high pressure by using Ba–BN solvent.* Journal of Crystal Growth **303**, 525 (2007).

[175] J. Sofo, A. Chaudhari, and G. Barber. *Graphane: A two-dimensional hydrocarbon.* Physical Review B **75**, 153401 (2007).

[176] B. Eren, D. Hug, L. Marot, R. Pawlak, M. Kisiel, R. Steiner, D. M. Zumbühl, and E. Meyer. *Pure hydrogen low-temperature plasma exposure of HOPG and graphene: Graphane formation?* Beilstein Journal of Nanotechnology **3**, 852 (2012).

[177] C. Woods, F. Withers, M. Zhu, Y. Cao, G. Yu, A. Kozikov, M. B. Shalom, S. Morozov, M. van Wijk, and A. Fasolino. *Macroscopic self-reorientation of interacting two-dimensional crystals.* Nature Communications **7**, 10800 (2016).

[178] D. Wang, G. Chen, C. Li, M. Cheng, W. Yang, S. Wu, G. Xie, J. Zhang, J. Zhao, and X. Lu. *Thermally Induced Graphene Rotation on Hexagonal Boron Nitride.* Physical Review Letters **116**, 126101 (2016).

[179] L. Zhang, D. A. Pejaković, B. Geng, and J. Marschall. *Surface modification of highly oriented pyrolytic graphite by reaction with atomic nitrogen at high temperatures.* Applied Surface Science **257**, 5647 (2011).

[180] M. Moisan, Z. Zakrzewski, M. Moisan, and Z. Zakrzewski. *Plasma sources based on the propagation of electromagnetic surface waves.* Journal of Physics D: Applied Physics **24**, 1025 (1991).

[181] K. Sancier and H. Wise. *Diffusion and Heterogeneous Reaction. XI. Diffusion Coefficient Measurements for Gas Mixture of Atomic and Molecular Hydrogen.* Journal of Chemical Physics **51**, 1434 (1969).

[182] S. Weissman and E. Mason. *Estimation of the mutual diffusion coefficient of hydrogen atoms and molecules.* The Journal of Chemical Physics **36**, 794 (1962).

[183] R. Geick, C. H. Perry, and G. Rupprecht. *Normal modes in hexagonal boron nitride.* Physical Review Letters **146**, 543 (1966).

[184] M. Begliarbekov, K.-I. Sasaki, O. Sul, E.-H. Yang, and S. Strauf. *Optical control of edge chirality in graphene.* Nano Letters **11**, 4874 (2011).

[185] L. Jiao, L. Zhang, X. Wang, G. Diankov, and H. Dai. *Narrow graphene nanoribbons from carbon nanotubes.* Nature **458**, 877 (2009).

[186] S. Wu, B. Liu, C. Shen, S. Li, X. Huang, X. Lu, P. Chen, G. Wang, D. Wang, M. Liao, et al. *Magnetotransport Properties of Graphene Nanoribbons with Zigzag Edges.* Physical Review Letters **120**, 216601 (2018).

[187] L. Cancado, M. Pimenta, B. Neves, M. Dantas, and A. Jorio. *Influence of the atomic structure on the Raman spectra of graphite edges.* Physical Review Letters **93**, 247401 (2004).

[188] D. Basko. *Boundary problems for Dirac electrons and edge-assisted Raman scattering in graphene.* Physical Review B **79**, 205428 (2009).

[189] D. S. Wastl, A. J. Weymouth, and F. J. Giessibl. *Optimizing atomic resolution of force microscopy in ambient conditions.* Physical Review B **87**, 245415 (2013).

[190] N. J. Couto, D. Costanzo, S. Engels, D.-K. Ki, K. Watanabe, T. Taniguchi, C. Stampfer, F. Guinea, and A. F. Morpurgo. *Random strain fluctuations as dominant disorder source for high-quality on-substrate graphene devices.* Physical Review X **4**, 041019 (2014).

[191] D. Bischoff, J. Güttinger, S. Dröscher, T. Ihn, K. Ensslin, and C. Stampfer. *Raman spectroscopy on etched graphene nanoribbons.* Journal of Applied Physics **109**, 073710 (2011).

[192] P. Koskinen, S. Malola, and H. Häkkinen. *Self-Passivating Edge Reconstructions of Graphene.* Physical Review Letters **101**, 115502 (2008).

[193] K.-i. Sasaki, R. Saito, K. Wakabayashi, and T. Enoki. *Identifying the orientation of edge of graphene using G band Raman spectra.* Journal of the Physical Society of Japan **79**, 044603 (2010).

[194] C. Cong, T. Yu, and H. Wang. *Raman study on the G mode of graphene for determination of edge orientation.* ACS Nano **4**, 3175 (2010).

[195] L. Campos, A. Young, K. Surakitbovorn, K. Watanabe, T. Taniguchi, and P. Jarillo-Herrero. *Quantum and classical confinement of resonant states in a trilayer graphene Fabry-Pérot interferometer.* Nature Communications **3**, 1239 (2012).

[196] A. F. Young and P. Kim. *Quantum interference and Klein tunnelling in graphene heterojunctions.* Nature Physics **5**, 222 (2009).

[197] P. Rickhaus, R. Maurand, M.-H. Liu, M. Weiss, K. Richter, and C. Schönenberger. *Ballistic interferences in suspended graphene.* Nature communications **4**, 2342 (2013).

[198] M.-H. Liu, K. Richter, et al. *Efficient quantum transport simulation for bulk graphene heterojunctions.* Physical Review B **86**, 115455 (2012).

[199] J. R. Wallbank, M. Mucha-Kruczyński, X. Chen, and V. I. Fal'ko. *Moiré superlattice effects in graphene/boron-nitride van der Waals heterostructures.* Annalen der Physik **527**, 359 (2015).

[200] S. Morita, F. J. Giessibl, E. Meyer, and R. Wiesendanger. *Noncontact atomic force microscopy*, volume 3 (Springer, 2015).

[201] K. He, A. W. Robertson, Y. Fan, C. S. Allen, Y.-C. Lin, K. Suenaga, A. I. Kirkland, and J. H. Warner. *Temperature Dependence of the Reconstruction of Zigzag Edges in Graphene.* ACS Nano **9**, 4786 (2015).

[202] C. Kloeffel and D. Loss. *Prospects for spin-based quantum computing in quantum dots.* Annual Review of Condensed Matter Physics **4**, 51 (2013).

[203] C. Kloeffel, M. J. Rančić, and D. Loss. *Direct Rashba spin-orbit interaction in Si and Ge nanowires with different growth directions.* Physical Review B **97**, 235422 (2018).

[204] L. C. Camenzind, L. Yu, P. Stano, J. Zimmerman, A. C. Gossard, D. Loss, and D. M. Zumbühl. *Hyperfine-phonon spin relaxation in a single-electron GaAs quantum dot.* arXiv:1711.01474 (2017).

[205] N. Samkharadze, G. Zheng, N. Kalhor, D. Brousse, A. Sammak, U. Mendes, A. Blais, G. Scappucci, and L. Vandersypen. *Strong spin-photon coupling in silicon.* Science **359**, 1123 (2018).

[206] X. Mi, M. Benito, S. Putz, D. M. Zajac, J. M. Taylor, G. Burkard, and J. R. Petta. *A coherent spin–photon interface in silicon.* Nature **555**, 599 (2018).

[207] A. Landig, J. Koski, P. Scarlino, U. Mendes, A. Blais, C. Reichl, W. Wegscheider, A. Wallraff, K. Ensslin, and T. Ihn. *Coherent spin-qubit photon coupling.* arXiv:1711.01932 (2017).

[208] J. Taylor, H.-A. Engel, W. Dür, A. Yacoby, C. Marcus, P. Zoller, and M. Lukin. *Fault-tolerant architecture for quantum computation using electrically controlled semiconductor spins.* Nature Physics **1**, 177 (2005).

[209] J. M. Taylor, V. Srinivasa, and J. Medford. *Electrically protected resonant exchange qubits in triple quantum dots.* Physical Review Letters **111**, 050502 (2013).

[210] D. P. DiVincenzo, D. Bacon, J. Kempe, G. Burkard, and K. B. Whaley. *Universal quantum computation with the exchange interaction.* Nature **408**, 339 (2000).

[211] J. Medford, J. Beil, J. Taylor, S. Bartlett, A. Doherty, E. Rashba, D. DiVincenzo, H. Lu, A. Gossard, and C. M. Marcus. *Self-consistent measurement and state tomography of an exchange-only spin qubit.* Nature Nanotechnology **8**, 654 (2013).

[212] L. P. Kouwenhoven, D. Austing, and S. Tarucha. *Few-electron quantum dots.* Reports on Progress in Physics **64**, 701 (2001).

[213] C. Escott, F. Zwanenburg, and A. Morello. *Resonant tunnelling features in quantum dots.* Nanotechnology **21**, 274018 (2010).

[214] M. Möttönen, K. Tan, K. Chan, F. Zwanenburg, W. Lim, C. Escott, J.-M. Pirkkalainen, A. Morello, C. Yang, J. Van Donkelaar, et al. *Probe and control of the reservoir density of states in single-electron devices.* Physical Review B **81**, 161304 (2010).

[215] M. T. Björk, C. Thelander, A. E. Hansen, L. E. Jensen, M. W. Larsson, L. R. Wallenberg, and L. Samuelson. *Few-electron quantum dots in nanowires.* Nano Letters **4**, 1621 (2004).

[216] D. Biesinger, C. Scheller, B. Braunecker, J. Zimmerman, A. Gossard, and D. Zumbühl. *Intrinsic metastabilities in the charge configuration of a double quantum dot.* Physical Review Letters **115**, 106804 (2015).

[217] R. Li, F. E. Hudson, A. S. Dzurak, and A. R. Hamilton. *Pauli spin blockade of heavy holes in a silicon double quantum dot.* Nano Letters **15**, 7314 (2015).

[218] D. Schröer, A. Greentree, L. Gaudreau, K. Eberl, L. Hollenberg, J. Kotthaus, and S. Ludwig. *Electrostatically defined serial triple quantum dot charged with few electrons.* Physical Review B **76**, 075306 (2007).

[219] G. Granger, L. Gaudreau, A. Kam, M. Pioro-Ladrière, S. Studenikin, Z. Wasilewski, P. Zawadzki, and A. Sachrajda. *Three-dimensional transport diagram of a triple quantum dot.* Physical Review B **82**, 075304 (2010).

A Fabrication Recipes

In this section detailed fabrication recipes used to produce the samples investigated in this thesis are listed.

A.1 hBN/graphene and hBN/graphene/hBN stacks

A.1.1 hBN/graphene assembly

Cleave two Si^{++}/SiO_2 wafer pieces: chip 1 for the exfoliation of hBN and chip 2 for a graphene-transfer wafer, both wafers with ~ 1 cm side length

- **chip 1:** hBN substrate wafer
  - **Cleaning:** 3 min in acetone and 3 min in IPA at 100 % ultrasonication power; 3 min UVO; 3 min on hotplate at 120 °C
  - **Exfoliation of hBN:** Use Nitto tape to cleave hBN crystals about ~ 10 times, press on wafer and peel-off slowly
  - **Choose suitable hBN flake:** OM to find suitable hBN flakes regarding their size, thickness and location on the wafer
  - **Annealing:** Annealing in quartz tube oven for cleaning the hBN surfaces (see section A.2 for the annealing recipe)
  - **AFM:** Check cleanliness of hBN flake with AFM, surface roughness should be below 0.1 nm
- **chip 2:** graphene transfer wafer
  - **Cleaning:** 3 min in acetone and 3 min in IPA at 100 % ultrasonication power; 10 min UVO; 3 min on hotplate at 250 °C
  - **Spin coat dextrane:** 5000 rpm, 4 s ramp time, 40 s, bake 1 min at 150 °C

  - **Spin coat PMMA:** 4000 rpm, 4 s ramp time, 40 s, $\sim$ 500 nm thick, bake 2 min at 180 °C
  - **Exfoliate graphene on polymer stack:** Use Nitto tape to cleave graphite crystals about $\sim$ 10 times, press on wafer and peel-off slowly
  - **Find suitable graphene flake:** OM to find suitable graphene flakes regarding their size and location on the wafer
  - **Raman spectroscopy:** Use Raman spectroscopy to verify SL character of flake
  - **Fish on glass plate:** Put chip in petri dish filled with DI water and let the dextrane layer dissolve. Fish PMMA layer with graphene flake on top with the glass slide which has a hole in the middle. Let it dry overnight.

- **Transfer graphene onto hBN flake:**
  - **Transfer with mask aligner:** Mount chip 1 and the glass slide with the graphene/PMMA layer into a mask aligner setup. Heat chip 1 to 120 °C and bring graphene flake slowly in contact. After contact heat to 180 °C and wait for $\sim$ 5 min, then retract the glass plate and remove the chip
  - **Lift-off:** Remove PMMA layer by lift-off in warm acetone at 50 °C for $\sim$ 1h, put in room-T IPA and blow dry with N_2-gun

A.1.2 hBN/graphene/hBN stacks

In order to encapsulate a graphene on hBN flake, a top hBN flake can be transferred on top, done as follows.

- **chip 1:** graphene/hBN sample prepared as described in section A.1.1
- **chip 2:** hBN transfer wafer
  - **Cleaning:** 5 min in acetone and 5 min in IPA at 100 % ultrasonication power; 5 min UVO

  - **Spin coat Poly-propylene carbonate (PPC):** 2500 rpm, 4 s ramp time, 60 s, $\sim 1\,\mu$m thick, bake 5 min at 80 °C
  - **Prepare stamp:** Cut-out window in double-layered scotch tape and press on Si/SiO_2/PPC chip
  - **Exfoliation of hBN:** Use Nitto tape to cleave hBN crystals about ~ 10 times, press on wafer and peel-off slowly
  - **Choose suitable hBN flake:** OM to find suitable hBN flakes regarding their size, thickness and location on the wafer
  - **Finish stamp:** Peel-off PPC and place on a PDMS cube which lies on a glass slide

- **Transfer hBN onto graphene/hBN sample**
  - **Transfer with mask aligner:** Mount chip 1 and the PPC/PDMS stamp into a mask aligner setup. Align top hBN flake to graphene/hBN sample and bring them slowly into contact. After contact heat to 80 °C to release PPC from PDMS, then retract the glass plate and remove the chip
  - **Bake:** Put on hotplate for ~ 5 min at 150 °C
  - **Lift-off:** Remove PPC layer by lift-off in warm chloroform at 50 °C for $\sim$ 1h, put in room-T IPA and blow dry with N_2-gun
  - **Annealing:** Thermally anneal the whole stack in a rapid-thermal annealer in an Ar/H_2 atmosphere at 300 °C for 3 h

A.2 Hydrogen Plasma Etching and Annealing

In the following, a detailed description of the H plasma etching process is given. If samples should be annealed, the procedure was the same except that no plasma was ignited.

- Sample is put on a quartz boat, which is placed at the desired distance from the surfatron, inside the plasma tube
- Place glass plates which hinder the plasma to interact with the metallic closures of the quartz tube plasma chamber and close the chamber
- Install the Faraday cage and connect the RF power source to the surfatron. Ground the surfatron, the Faraday cage and the oven housing.
- Pumping with a scroll pump in combination with a turbo pump to reach a base pressure $< 5{\cdot}10^{-3}$ mbar.
- Slowly turn on the hydrogen flux and fix it at 20 SCCM with a mass flow controller.
- Tune the gas pressure inside the tube to the desired working pressure value. Then start heating towards the desired operation temperature
- When the operation temperature is reached, ignite the plasma and make sure that the reflected power is zero.
- After the desired exposure time has passed, the plasma and the oven are switched off.
- When T $< 100\,^{\circ}$C the H flow is stopped and the pumps are switched off. Then the plasma tube is slowly vented and the samples are removed.

A.3 Electron Beam Lithography

A.3.1 Used PMMA

Generally 950k PMMA from *Allresist* was used. Depending on the process which followed (e.g. metal evaporation for contacts, RIE etching) different thicknesses were desirable and adjusted by the level of dilution of PMMA in its solvent Chlorobenzene.

In this work, mostly 5 % and 2 % PMMA was used, which was spin-coated onto the samples with the following parameters:

- **Rotation speed:** 4000 rpm
- **Ramp time:** 4 s
- **Duration:** 40 s
- **Baking:** 5 min at 180 °C

A.3.2 Large Contact Structures

- **Acceleration voltage EHT:** 20 kV
- **Aperture:** 120 μm
- **Working distance:** 17.7 mm
- **Write field:** 2000 μm
- **Area step size:** 31.1 nm or 62 nm
- **Area dose:** 500 μC/cm^2

A.3.3 Small Contact Structures and Artificial Defects

- **Acceleration voltage EHT:** 30 kV
- **Aperture:** 10 μm
- **Working distance:** 9.1 mm
- **Write field:** 250 μm
- **Area step size:** 3.9 nm
- **Area dose:** 500 μC/cm^2

A.3.4 Development

Cold development was performed in order to avoid cracking on top of hBN substrates. Therefore, the chip is immersed in a mixture of IPA:H_2O (ratio 7:3) at $\sim$5 °C for 60 s and then blown dry.

A.4 Reactive Ion Etching Recipes

For the processes described in the following, an RIE system from Oxford (Plasma 80 Plus) is used.

A.4.1 Cut Graphene

- **Base pressure:** $5{\cdot}10^{-5}$ mbar
- **Ar/O_2 contents:** 16 %/8 %
- **Power:** 30 W
- **Process pressure:** 25 mTorr
- **Time:** 30 s

A.4.2 Cut hBN/graphene/hBN Stack

- **Base pressure:** $5{\cdot}10^{-5}$ mbar
- **SF_6/Ar/O_2 contents:** 76 %/3.6 %/5 %
- **Power:** 50 W
- **Process pressure:** 25 mTorr
- **Time:** Depending on the thickness of the stack. Etch rate $\sim$ 600 nm/min.

A.4.3 Etching Before Side-contact Evaporation

- **Base pressure:** $5{\cdot}10^{-5}$ mbar
- **CHF_3/O_2 contents:** 80 %/4 %
- **Power:** 60 W
- **Process pressure:** 60 mTorr
- **Time:** Depending on the thickness of the stack. Etch rate $\sim$ 20 nm/min.

Acknowledgments

Special thanks goes to Prof. Dominik Zumbühl who guided me through my PhD time and to whom I am proud of to be able to call my *Doktorvater*. His passion for physics and his scientific intuition were truly inspiring. He always had time for discussions and was open for new ideas. His ability to explain complicated processes with easy words saved me lots of time and his enthusiasm, paired with his profound knowledge, made him certainly a great teacher. Also, besides work, it was very enjoyable to spend time with Dominik. For example, at the numerous BBQs we had on the roof-top of the physics building. There he demonstrated that he is not only a great physicist but also an exceptionally gifted grill master.

I would like to thank Prof. Andras Kis for his interest in my work and for being part of my PhD committee.

Great thanks go to all the group members of the Quantum Coherence Lab. In particular, I would like to thank Florian Froning, who gave me a warm welcome into the Ge/Si nano wire project. His astute and, at the same time, inspiring work attitude made the collaboration with him very pleasant. Our post-doc Floris Braakman was always there for discussions and his seminal ideas for the experiments were very valuable. Further, I would like to thank Y. Bilal Kalyoncu for his collaboration during the work on the graphene project. He always remained calm, even when things didn't work out as we wished. A big thank-you goes to Leon Camenzind for the enlightening afternoon-walks, where we discussed physics as well as other mysteries of life. Our post-doc Christian Scheller was always very helpful when Igor questions came up and the whole group benefits from his rich experience in the lab. I also want to thank Taras Patlatiuk for his help in the lab when noise-hunting was a topic. Moreover, my thanks goes to Timothy Camenzind for being a good and motivated project and master student, who afterwards joined our group as a PhD student. I thank Kris Cerveny for his help on grammar issues. Especially during writing my thesis he helped me a lot. Mario Palma

and Pirmin Weigele always added an exciting atmosphere to the group-life and we had many amusing conversations.

Last but not least, I want to thank my wife Patricia who was very supportive throughout my PhD time. Her life-affirming and cheerful being is a source of motivation and essential for me in many different aspects.